3.2 SOMBRERO CHAMBER DESIGN AND ANALYSIS

3.2.1 Laser Propagation in Cavity Gas

Primary to the SOMBRERO design is the choice of xenon gas density that fills the target chamber. Our approach in the target chamber design is to choose a target chamber fill gas that absorbs the target generated x rays and ions and re-radiates the energy to the target chamber first wall over the longest possible time while simultaneously allowing the propagation of the laser beams to the target. We have chosen xenon as a target chamber fill gas, because it has a high cross-section for stopping x rays and energetic ions and because it is chemically inert in its neutral state. Also, xenon is one of the few high atomic number elemental gases. We believe that breakdown of the gas by the laser places an upper limit on the density of the gas. In this section, we discuss laser-induced breakdown in the xenon chamber fill gas of SOMBRERO. We begin by discussing breakdown issues in laser fusion reactors. Here we also define the SOMBRERO target illumination conditions. We then review what laser-induced breakdown experimental results that we know to exist. Finally, we use these experimental results to extrapolate to the SOMBRERO conditions and choose a xenon density.

3.2.1.1 Laser-Induced Breakdown Issues

There is concern that laser-induced breakdown will affect the laser beams before they are absorbed in the target and will, therefore, reduce the target performance. If the uniformity of the laser illumination on the target is reduced, the implosion of the target will be less symmetric, and the thermonuclear burn of the DT fuel will be degraded. It is not clear to us how much breakdown is acceptable or where along the beam breakdown is allowed.

Breakdown very near to the surface of the target may not be detrimental to target performance. Even if there were no fill gas, the region near the target would be quickly filled with plasma because of blowoff from the target. So if the presence of ionized gas in the region near the target prevents proper implosion symmetry, then direct-drive laser fusion would not be possible under even vacuum conditions.

The laser intensity is much higher very close to the target than throughout most of the transport length. The illumination geometry for SOMBRERO is shown schematically in Fig. 3.2. Here, one sees the laser beams overlapping on the target. It is clear from this picture that it is only near the target that the beams overlap. The illumination parameters are given in Table 3.2. The peak intensity that the laser beams must jointly apply to the target is about 500 TW/cm^2. This is achieved with 60 beams with a peak intensity (over the beam cross-section) of 33 TW/cm^2. The radius at which the beams begin to overlap is ~1.2 cm. The average intensity rises quadratically from 33 TW/cm^2 at the overlap point to 500 TW/cm^2 at the target

surface. If breakdown within 1.2 cm of the target is acceptable, then laser-induced breakdown need only be considered at the lower intensity.

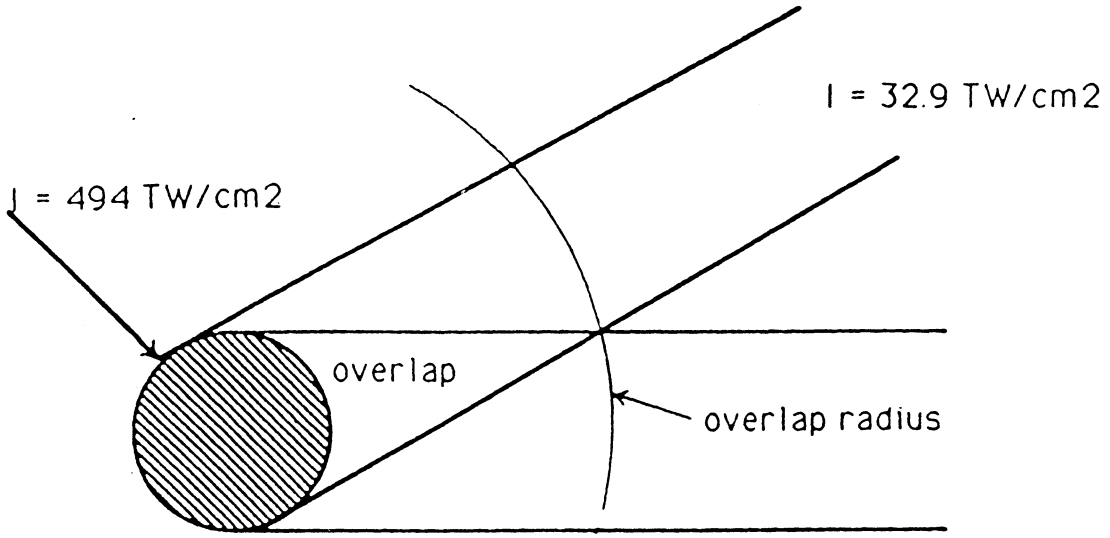

Fig. 3.2. Schematic picture of SOMBRERO target illumination geometry.

Table 3.2. SOMBRERO Target Illumination Parameters

Laser Pulse Width (ns)	6
Peak Total Intensity on Target ($TW/cm^{2)}$	500
Peak Beam Intensity ($TW/cm^{2)}$	33
Target Radius (cm)	0.3
Number of Beams	60
f # for Final Laser Optics	50
Overlap Radius (cm)	1.20
Fill Gas Species	Xenon
Fill Gas Density (cm^{-3})	1.8×10^{16} (0.5 Torr)

We are also curious as to the effects of incoherence on laser-induced breakdown. In the overlap region, the photons from separate laser beams are not coherent with each other. Their electric vectors are no longer in phase with each other so electron avalanche breakdown would be reduced compared to coherent light at the same intensity. However, KrF lasers produce light with photon energies of about 5 eV, so only three photons are needed to ionize a xenon atom, since xenon's ionization energy of 12.1 eV. Therefore, 3-photon absorption may be an important breakdown mechanism. There may be coherence effects with multi-photon absorption as well. If there are such effects, we may by able to use the single beam intensity even in the overlap region.

Breakdown is a process involving many effects and is not a simple threshold phenomenon. We choose to define breakdown in terms of free electron density, where the electron density is high enough to alter the passage laser light. We wish to know the xenon density allowed at SOMBRERO laser intensity, while not generating laser degrading electron density. This xenon density is a function of the laser intensity, the wavelength, the laser bandwidth, the laser coherence, the laser focal length, the spot size, the pulse width, and gas properties such as temperature and impurities. We have tried to rely on experimental results, but there are no experiments that meet all of the SOMBRERO conditions.

3.2.1.2 Breakdown Experimental Data

We have examined past experimental studies into laser induced breakdown and have found that the wavelength and density dependence is well documented.[3.5] Thresholds for four laser wavelengths were measured using ruby and neodymium lasers and their second harmonics, so the lowest wavelength used is 0.35 μm. This is still quite different from the KrF wavelength of 0.25 μm, so we have extrapolated. The spot radii varied and was 13 μm for the small wavelength, much smaller than the SOMBRERO value of 0.3 cm. The pulse width was 20 ns compared to 6 ns. The focal length was 18.4 mm compared with 30 m for SOMBRERO. Nothing is known about the smoothness of the laser profile. We can probably assume small bandwidths and high coherence. Breakdown was measured by observing visible emission at the focal spot. The threshold intensity as a function of gas pressure (or density) is shown in Fig. 3.3 for several wavelengths and for argon and xenon. The threshold intensity is seen to be a strong function of wavelength. One can also see that the threshold intensity for xenon is roughly the same at 1.06 μm as it would be at 0.25 μm . The measured breakdown threshold is plotted against wavelength for a number of densities for argon and xenon in Fig. 3.4. In these experiments, the breakdown threshold of xenon was measured above 1000 torr of gas pressure, three orders of magnitude higher than in SOMBRERO. Other experiments have measured the breakdown threshold near the SOMBRERO density for 1 μm laser light.[3.6, 3.7] The results of all

these experiments are shown in Fig. 3.5, where the quoted laser intensity thresholds for breakdown are plotted against gas density. One aspect of breakdown for which we have found no experimental studies is the effect of laser coherence.

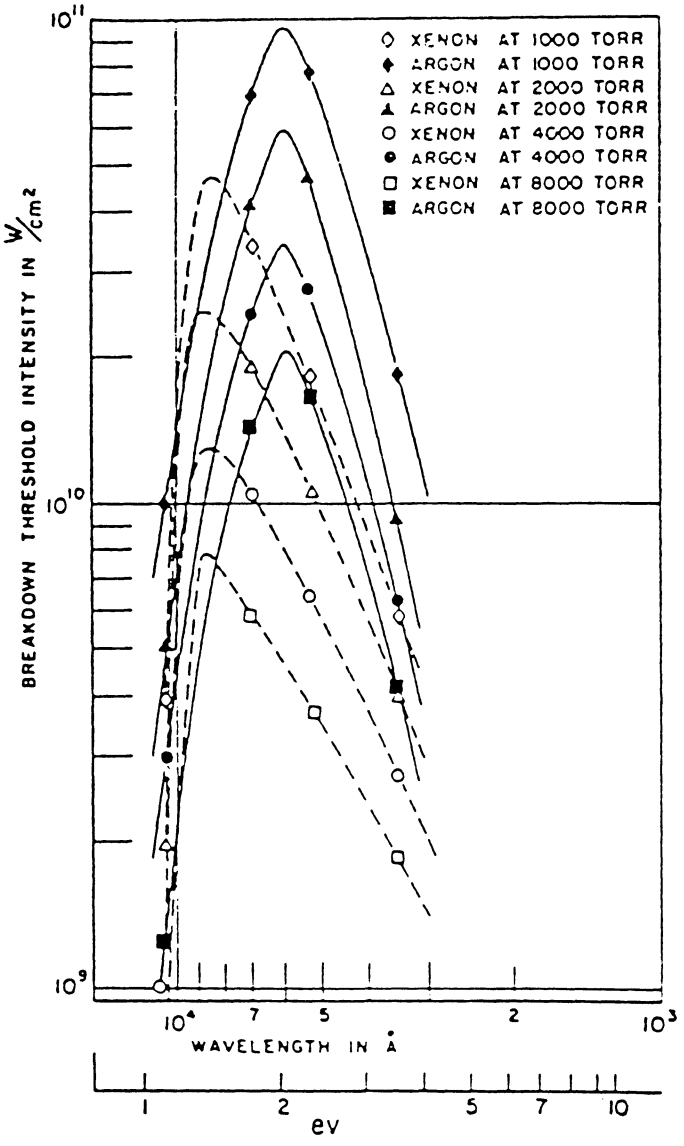

Fig. 3.3. Experimentally measured breakdown threshold intensities in xenon and argon versus wavelength for a number of densities. (Ref. 3.5)

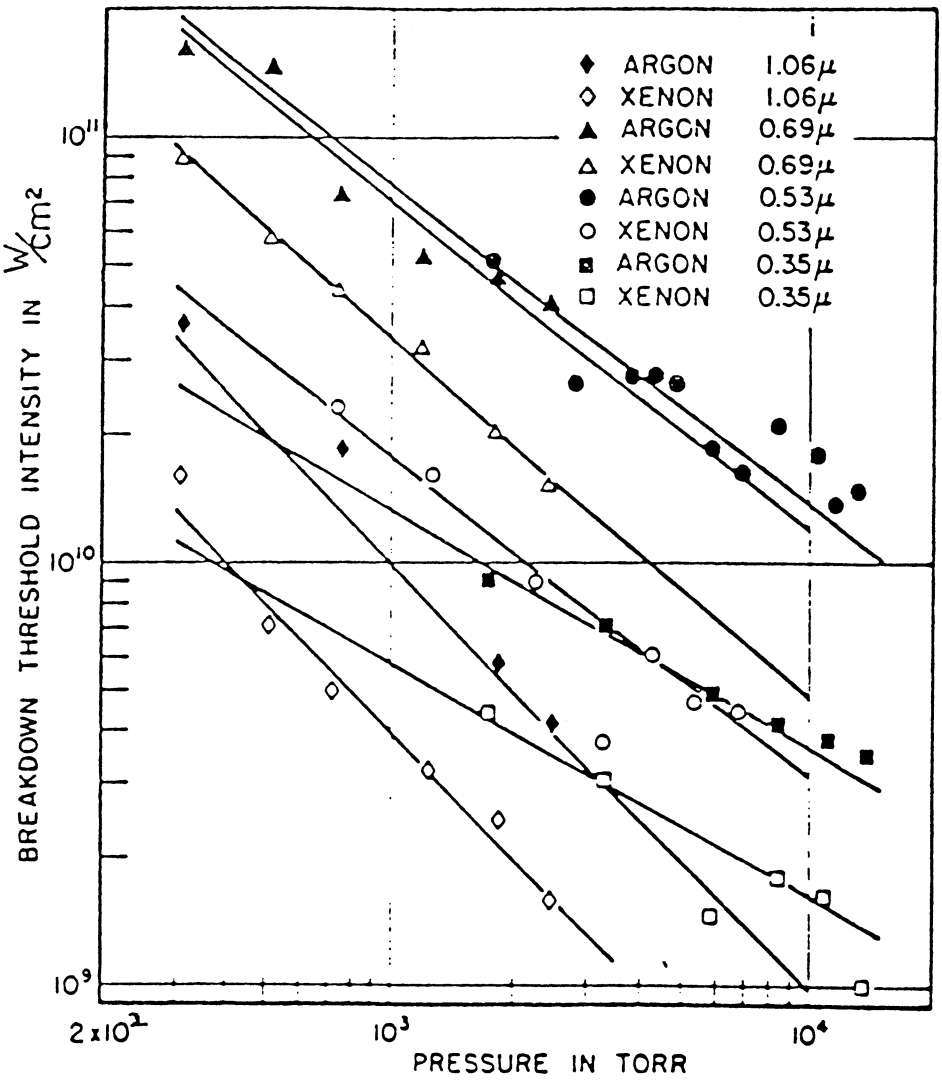

Fig. 3.4. Experimentally measured breakdown threshold intensities in xenon and argon versus density for a number of wavelengths. (Ref. 3.5)

3.2.1.3 Cavity Gas Density Limits

From Table 3.2 and Fig. 3.5, one sees that breakdown can be avoided with SOMBRERO parameters if we assume that the laser light must be coherent to breakdown and the density is 1.8×10^{16} cm^{-3} (0.5 Torr). The extrapolated line in Fig. 3.5 passes through 0.5 torr and 33 TW/cm^2. The experimental data at 1 μm wavelength is uncertain and could allow a higher gas pressure at 33 TW/cm^2. The Sandia National Laboratories results were that no breakdown was observed at this intensity in the gas density range of 0.1 to 0.5 torr. Therefore, we feel that 0.5 torr is a safe xenon gas density to avoid laser-induced breakdown at 33 TW/cm^2. Additionally, if breakdown within 1.2 cm of the target surface is acceptable, then we do not need to rely on increased breakdown threshold intensities due to the incoherence at adjacent beams or the incoherence induced in the beams to reduce parametric instabilities.

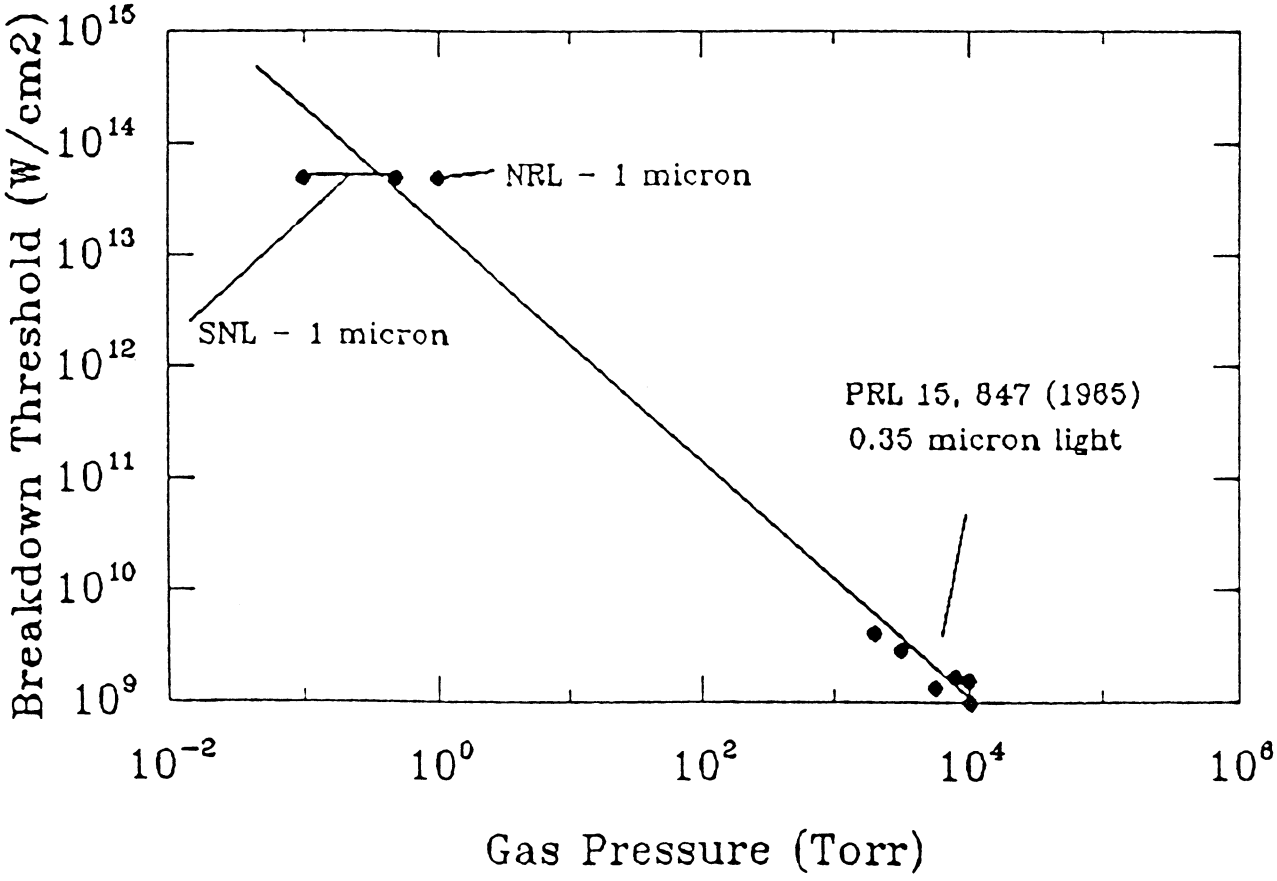

Fig. 3.5. Breakdown threshold intensities in xenon. Experimental values are shown as well as an extrapolated curve. (Refs. 3.5 - 3.7)

3.2.2 First Wall Protection

We propose to protect the graphite first wall of the SOMBRERO target chamber with 0.5 torr of xenon gas. The gas absorbs the target x rays and debris ions and re-radiates the energy to the wall over a long enough time that thermal conduction in the wall can keep the surface temperature low enough to avoid damage to the graphite. We will begin by describing the x rays and ions emitted from the target. We will then discuss the CONRAD computer code and how it calculates the re-radiation to the wall. We will also discuss the calculation of the wall surface temperatures. Finally, we will present the wall thermal and mechanical response.

3.2.2.1 Target Emanations

The SOMBRERO targets emit x rays, neutrons, and ions. The assumed target parameters are given in Table 3.3. The "Assumed" values were used in the calculations presented in this section. After these calculations were completed, the reference design point was changed to a slightly lower yield as shown under the "Base Case" column. Results will be scaled proportional to yield to generate "Base Case" results. The time-integrated x-ray spectrum is shown in Fig. 3.6. The intensity is shown in arbitrary units. The spectral shape is assumed to be independent of target yield, so the intensity is scaled uniformly in x-ray photon energy to reach the proper x-ray yield in Table 3.3. The debris ion energies are shown in Table 3.4. It is interesting to note the presence of very high energy carbon ions that are generated when the outer plastic shell is accelerated to a high velocity by the target micro-explosion. These carbon ions will have the longest range in the xenon gas of any of the target emanations except neutrons. The xenon gas must be thick enough to attenuate the carbon ions.

Table 3.3. Target Parameters for SOMBRERO

	Assumed	Base Case
Energy on Target (MJ)	3.6	3.4
Target Gain	118	118
Target Yield (MJ)	425	400
Neutron Yield (MJ)	317	298
X-ray Yield (MJ)	24	23
X-ray Pulse Width (ns)	0.1	0.1
Debris Yield (MJ)	84	79

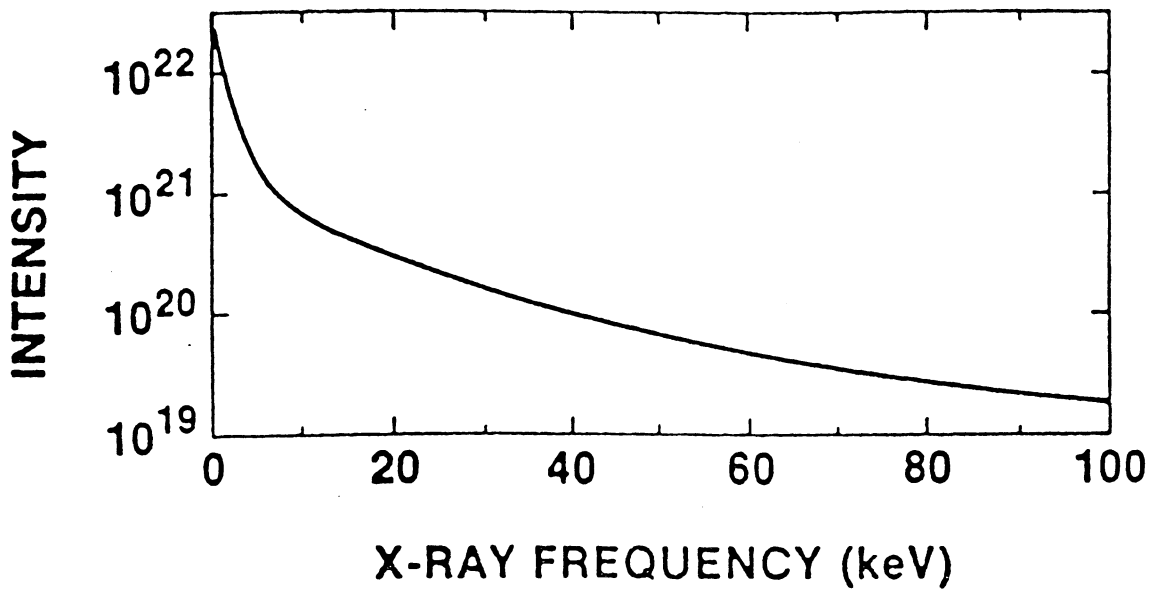

Fig. 3.6. Time-Integrated X-Ray Spectrum from SOMBRERO Target.

Table 3.4. Target Debris Spectra for SOMBRERO

Deuterium Energy (keV)	94
Protium Energy (keV)	138
Tritium Energy (keV)	141
Helium-4 Energy (keV)	188
Carbon-12 Energy (keV)	1650

3.2.2.2 CONRAD Computer Code

We have used the CONRAD computer code[3.8] to analyze the target chamber designs for SOMBRERO. CONRAD is a one-dimensional Lagrangian finite difference computer code that calculates hydrodynamic motion, radiation transport, and vaporization and condensation in slab, cylindrical, or spherical geometry. Radiation transport is calculated with flux limited multi-group diffusion. 180 group opacities are used in SOMBRERO calculations. Time-dependent target x-ray and ion deposition are calculated in the fill gas and walls. Heat transfer calculations are performed by CONRAD to get wall surface temperatures and temperature profiles in the wall at all times. Vaporization calculations can then be done.

Equation-of-state and opacity data is read by CONRAD from data tables. The properties of the materials are, therefore, assumed to be quasi-static. The data tables are created with equation-of-state results from the IONMIX[3.9] computer code or from the SESAME[3.10] library. IONMIX is better suited to materials much less dense than solids or liquids, while SESAME is preferred at higher density. Opacity tables are constructed with results from IONMIX.

3.2.2.3 First Wall Thermal Loading

The essential parameters for the SOMBRERO simulations are shown in Table 3.5. Parameters are shown for both assumed and "Base Case" conditions. The wall is taken to be 6.5 m in the simulation as this is the closest point in a non-spherical chamber. A steady state heat transfer calculation of the surface heat through the graphite leads to a steady state surface temperature of 1485°C. The results of the CONRAD simulation for the assumed conditions are plotted in Figs. 3.7 - 3.14. The radiation temperature is plotted over a radius versus time mesh in Fig. 3.7, where different shades of grade represent ranges of radiation temperature. The radiation temperature is that blackbody temperature that would provide the calculated radiation energy density. One can see the radiation burning through the xenon gas, finally reaching the wall some time near 0.1 ms. The radiation temperature is plotted against position for various times in Fig. 3.8. The surface heat flux on the wall of the SOMBRERO target chamber is shown in Fig. 3.9. The peak heat flux occurs at 86.8 μs. The CONRAD simulation predicts a peak surface temperature at the closest point on the wall of 2155°C, well below the sublimation temperature for graphite of 4100°C. Scaling this peak temperature to the "Base Case" conditions, the peak temperature would be 2116°C. CONRAD predicts that no graphite is vaporized. The xenon gas is very effective in slowing the transfer of energy from the target to the wall, which is why there is no vaporization. The surface temperature of the graphite is shown as a function of time in Fig. 3.10. The broad temperature pulse, which reaches a maximum at 0.134 ms, should be compared to the almost instantaneous target x-ray pulse and the target ion pulse width of a few ns. Based on this simulation, we believe that a 6.5 m radius graphite lined chamber filled with 0.5 torr of xenon will survive a 425 MJ target explosion. This situation for the "Base Case" is somewhat better because of the lower target yield.

3.2.2.4 First Wall Mechanical Loading

CONRAD calculations also predict the mechanical loading on the SOMBRERO target chamber first wall. The results of a CONRAD simulation for the assumed conditions is given in Table 3.5. The "Base Case" parameters are also shown in Table 3.5. The pressure profiles at various times are shown in Fig. 3.12. The gas density profiles are shown in Fig. 3.13. Comparing these with the radiation temperature profiles in Fig. 3.8, one may note that the gas

pressure moves with the radiation. This is also shown by comparing the gas pressure plotted over the time-position mesh of Fig. 3.12 with Fig. 3.7. There is very little hydrodynamic motion except near the target, which is shown in Fig. 3.13 and Fig. 3.14. The radiation diffuses through the gas, heating the gas as it goes. This is why the time of peak pressure and heat flux on the wall are the same. The peak pressure on the wall is very low, 0.0127 MPa. The impulse is also low. Neither should cause any major mechanical response in the first wall.

Table 3.5. SOMBRERO Gas and First Wall Parameters

	Assumed	**Base Case**
Gas Species	Xenon	
Gas Density (cm^{-3})	1.8×10^{16} (0.5 Torr)	
Distance to Wall (m)	6.5	
Wall Material	Woven Rigidized Graphite	
Steady State Wall Temperature (°C)	1485	
Peak Heat Flux on Wall (MW/cm^2)	0.138	0.130
Time of Peak Heat Flux (μs)	86.8	86.8
Peak Wall Temperature (°C)	2155	2116
Time of Peak Wall Temperature (ms)	0.134	0.134
Impulse on Wall (Pa-s)	2.21	2.08
Peak Pressure on Wall (MPa)	0.0127	0.0120
Time of Peak Pressure on Wall (μs)	88.7	88.7

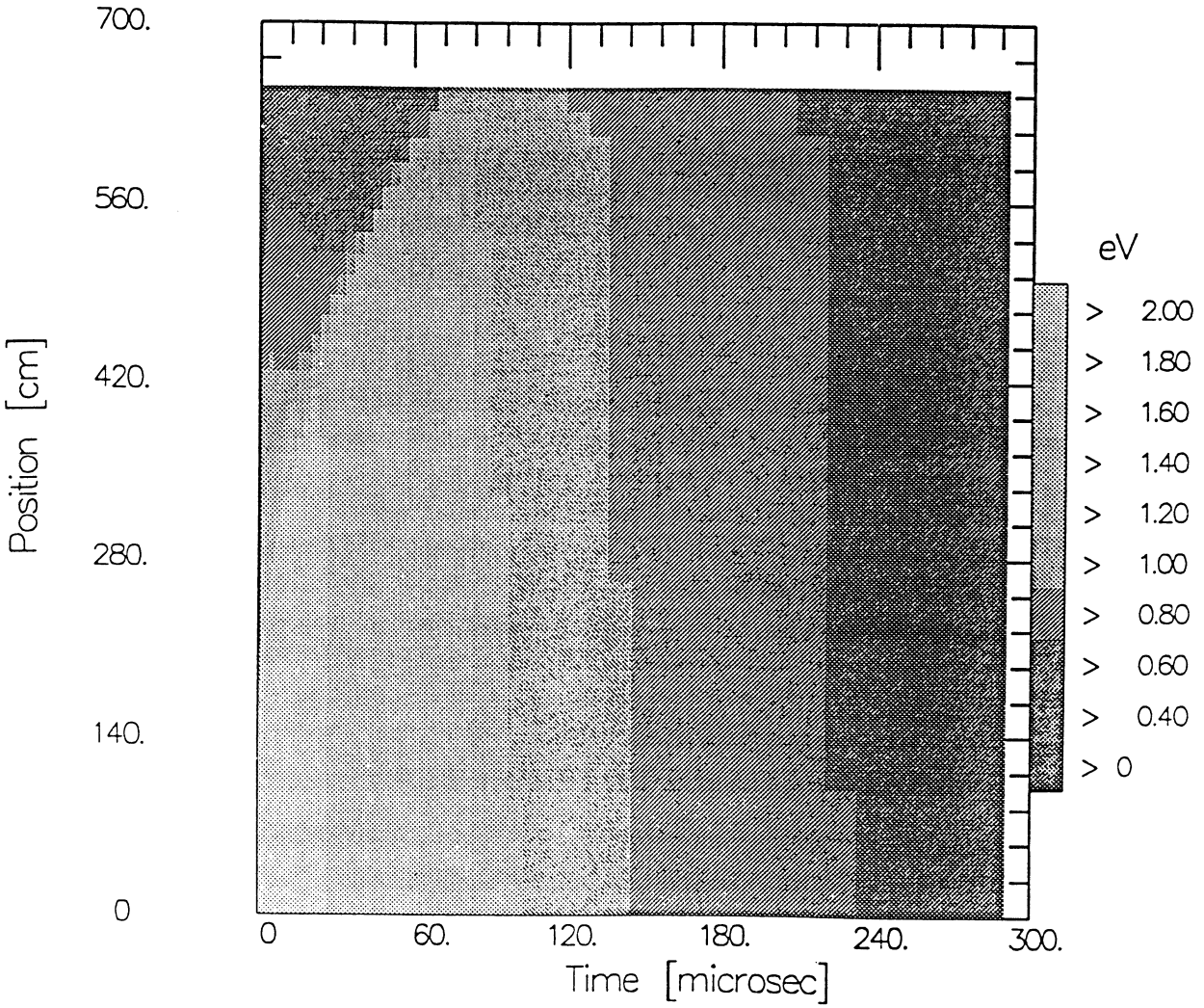

Fig. 3.7. Radiation temperatures in the SOMBRERO target chamber plotted over a time-position mesh. A 425 MJ yield, 0.5 torr Xenon fill gas, and a 650 cm radius chamber have been assumed. The target is positioned at the origin, the wall is at 650 cm.

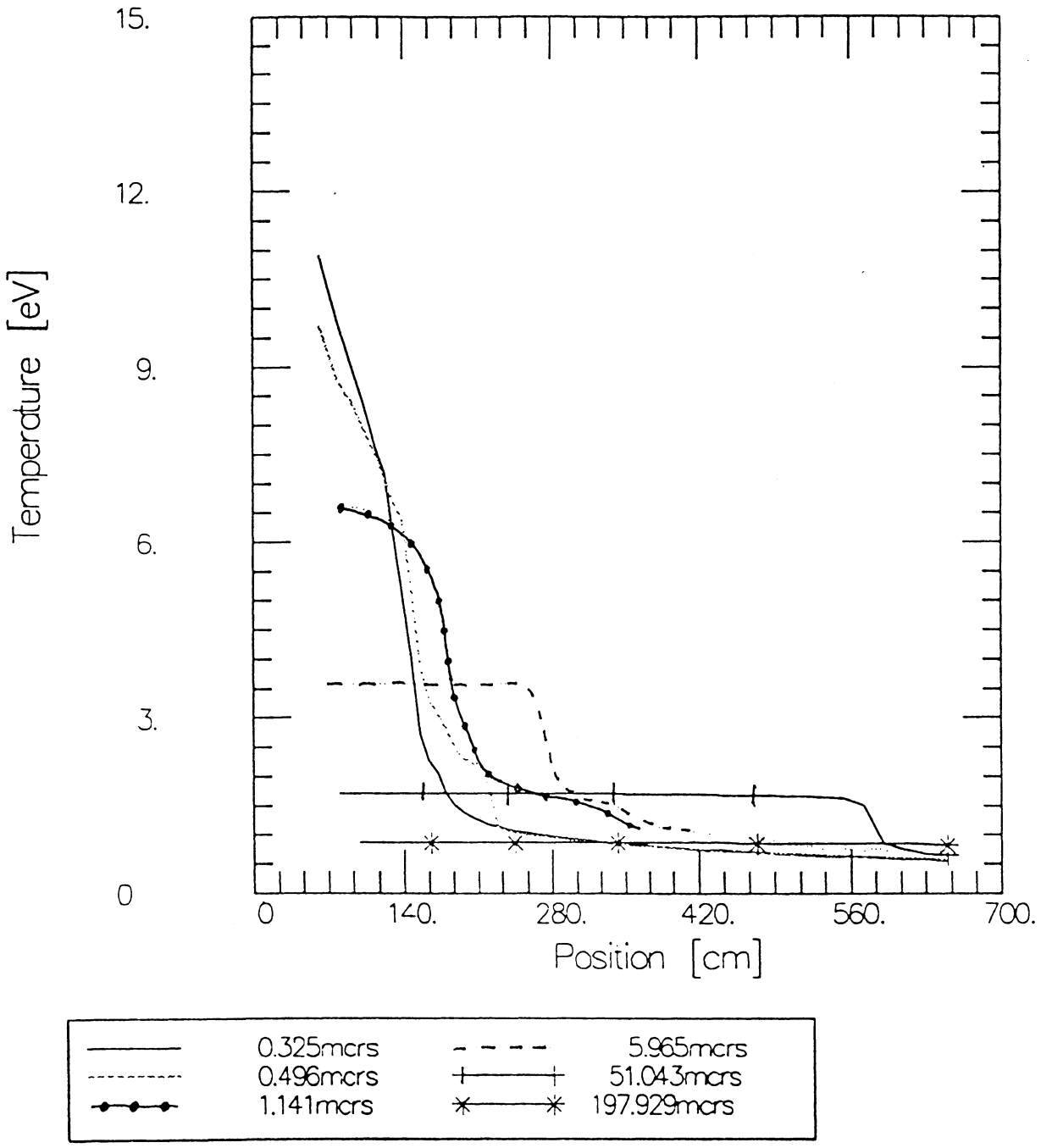

Fig. 3.8. Radiation temperature versus position for various times. A 425 MJ yield, 0.5 torr Xenon fill gas, and a 650 cm radius chamber have been assumed. The target is positioned at the origin, the wall is at 650 cm.

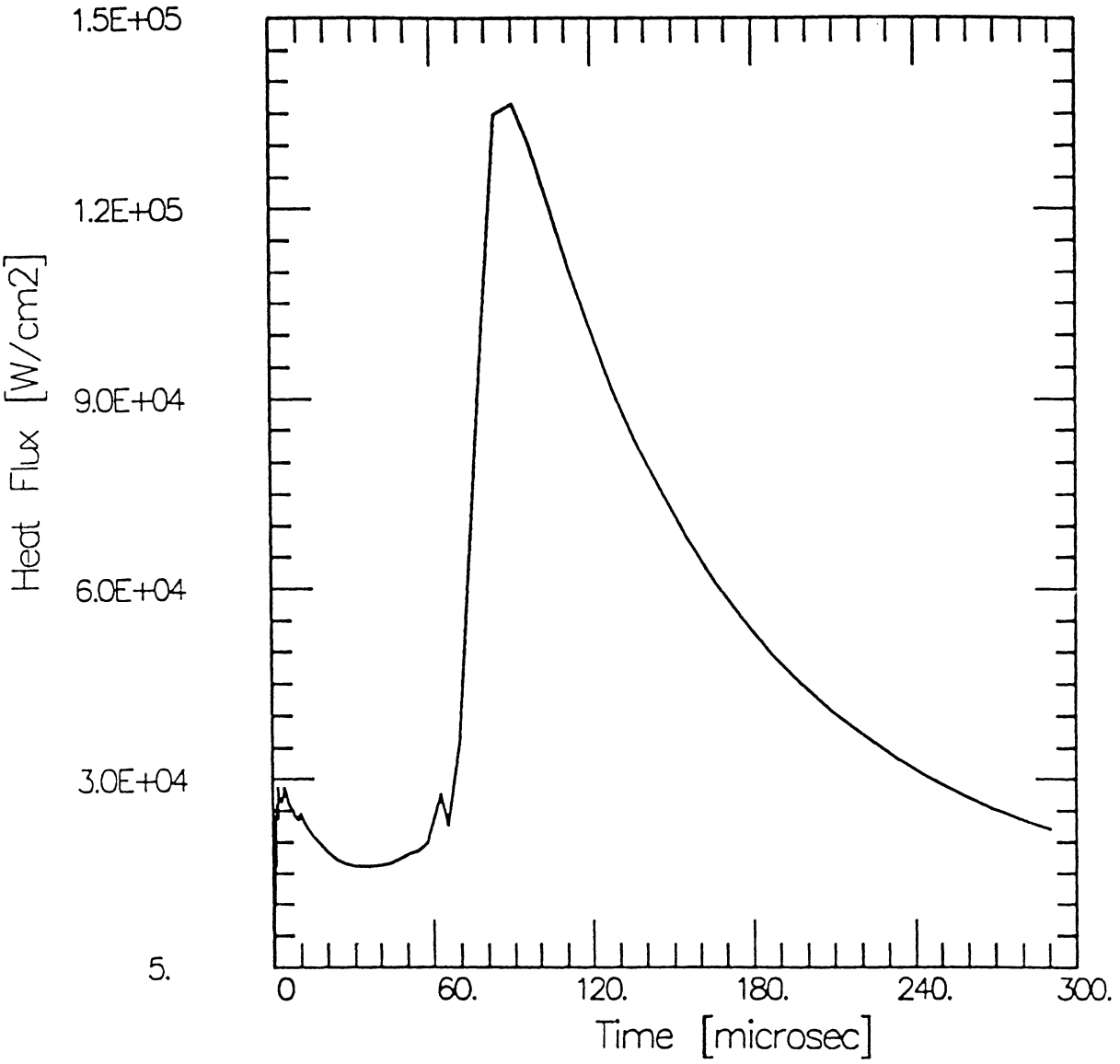

Fig. 3.9. Radiant heat flux on the surface of the SOMBRERO target chamber wall. A 425 MJ yield, 0.5 torr Xenon fill gas, and a 650 cm radius chamber have been assumed.

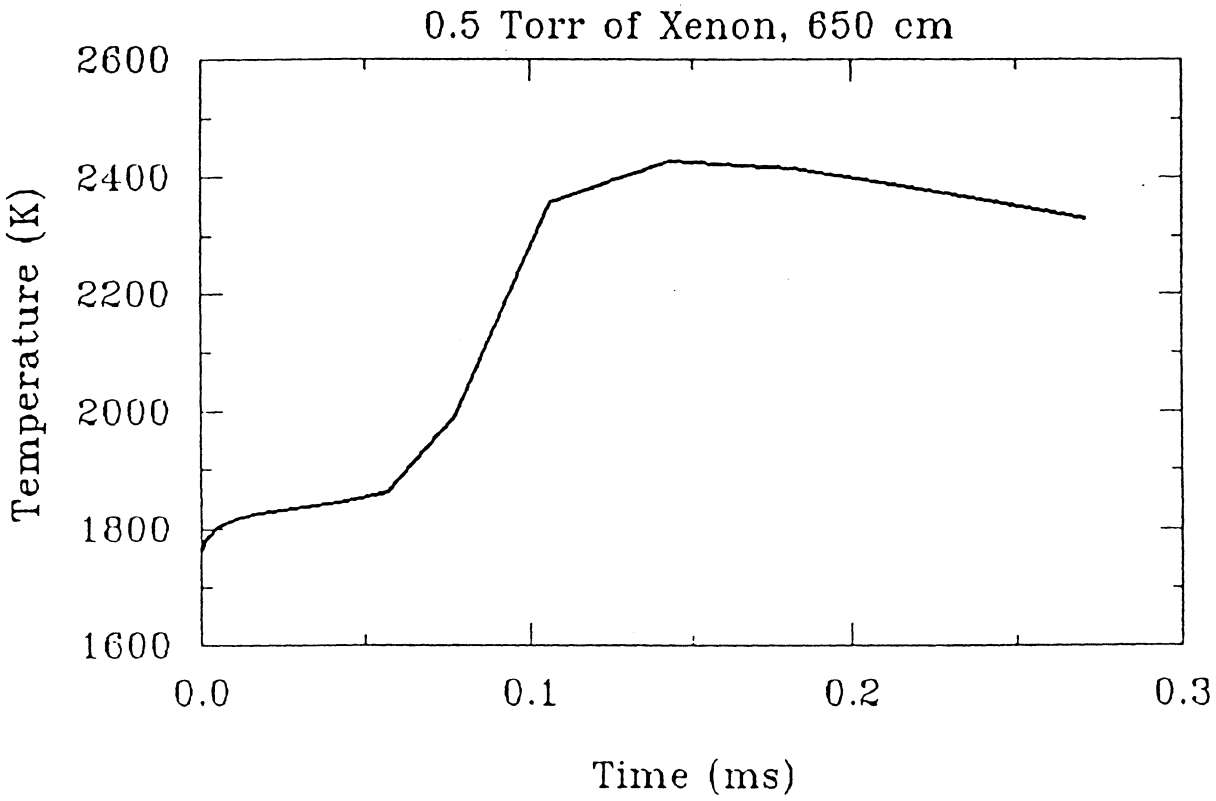

Fig. 3.10. Surface temperature on the graphite first wall of the SOMBRERO target chamber. A 425 MJ yield, 0.5 torr Xenon fill gas, and a 650 cm radius chamber have been assumed.

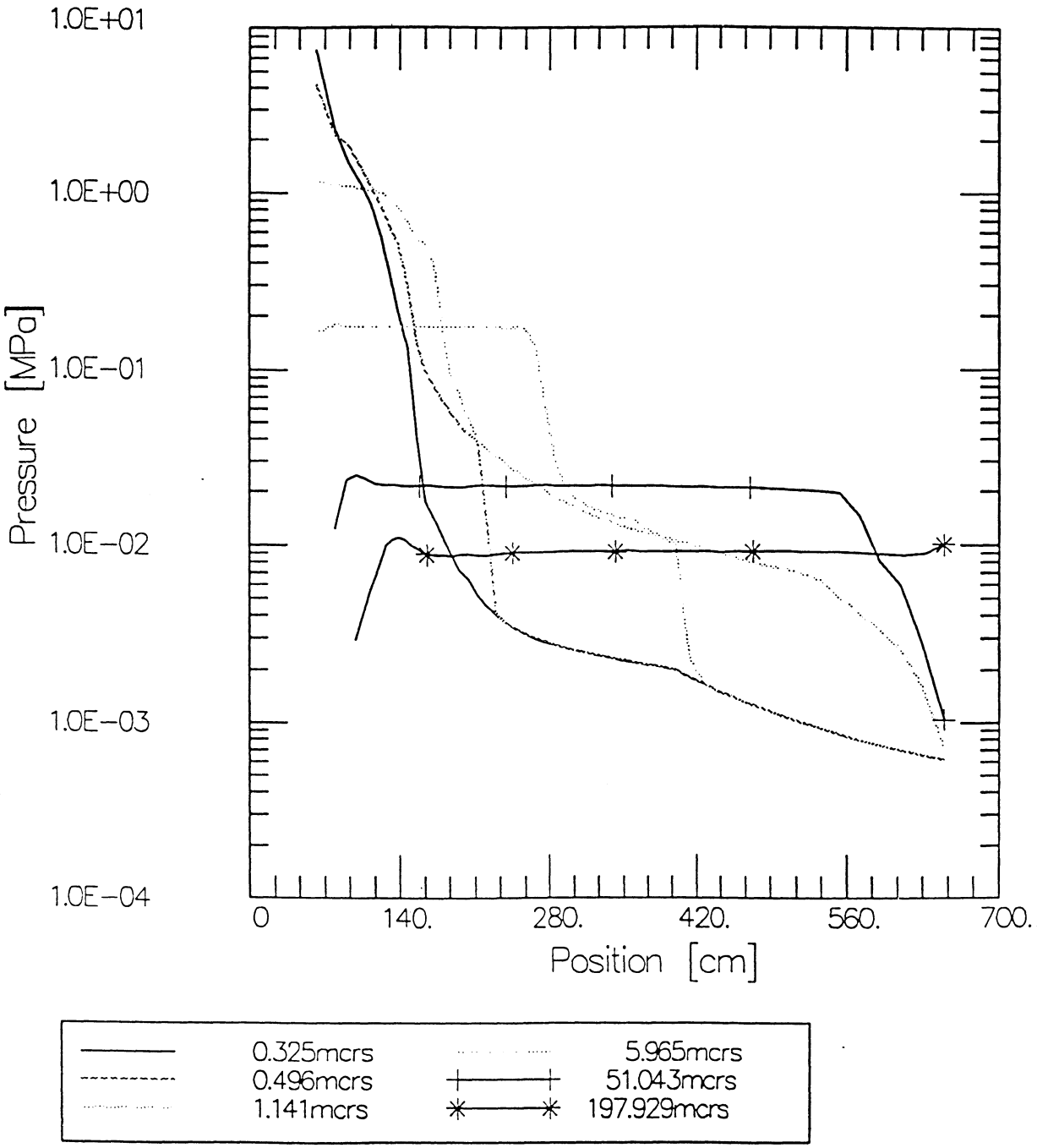

Fig. 3.11. **Gas pressure versus position for various times. A 425 MJ yield, 0.5 torr Xenon fill gas, and a 650 cm radius chamber have been assumed. The target is positioned at the origin, the wall is at 650 cm.**

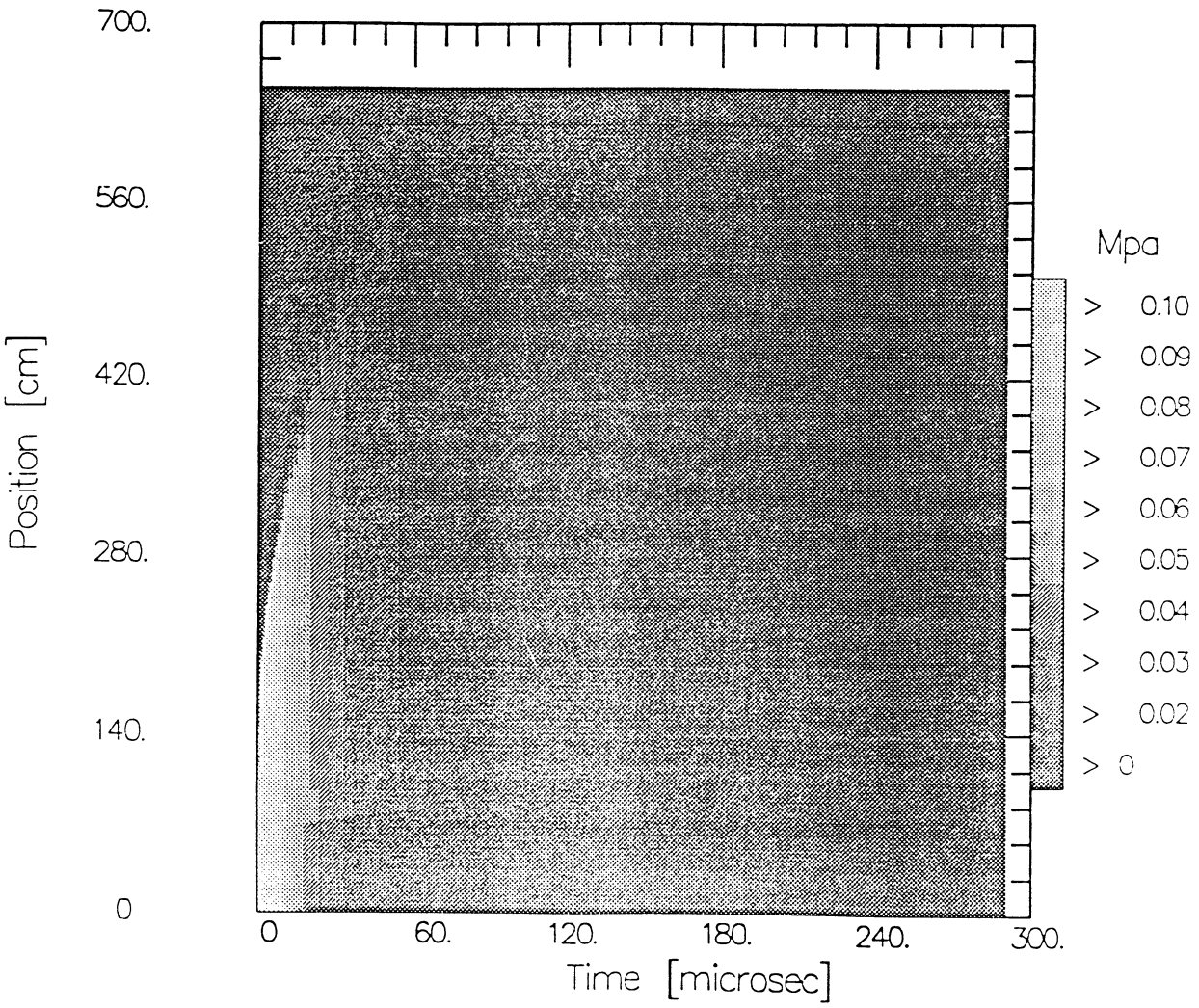

Fig. 3.12. **Gas pressure in the SOMBRERO target chamber plotted over a time-position mesh. A 425 MJ yield, 0.5 torr Xenon fill gas, and a 650 cm radius chamber have been assumed. The target is positioned at the origin, the wall is at 650 cm.**

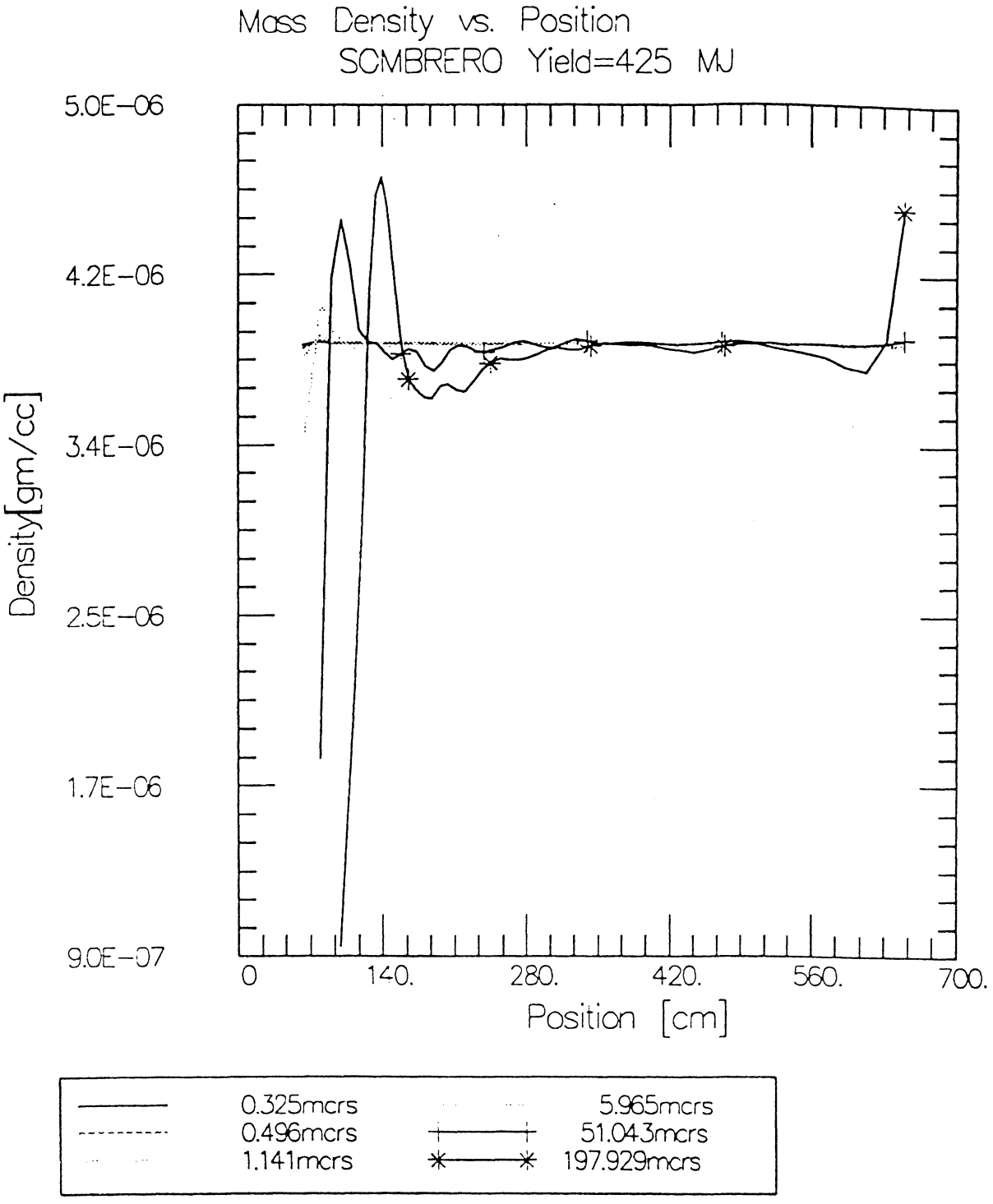

Fig. 3.13. **Gas density versus position for various times. A 425 MJ yield, 0.5 torr Xenon fill gas, and a 650 cm radius chamber have been assumed. The target is positioned at the origin, the wall is at 650 cm.**

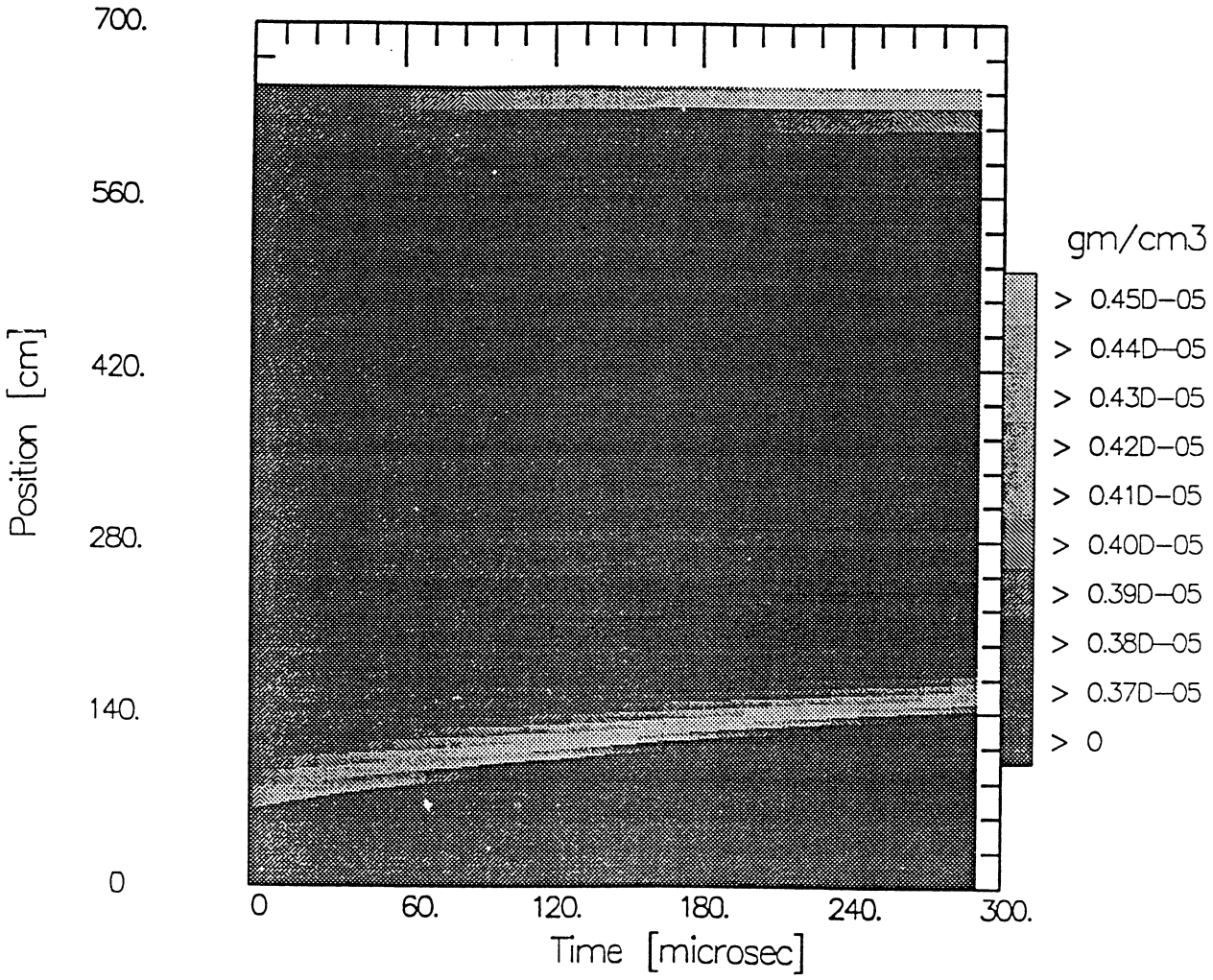

Fig. 3.14. **Gas density in the SOMBRERO target chamber plotted over a time-position mesh. A 425 MJ yield, 0.5 torr Xenon fill gas, and a 650 cm radius chamber have been assumed. The target is positioned at the origin, the wall is at 650 cm.**

3.2.3 First Wall and Blanket Design

3.2.3.1 Overall Chamber Description

The SOMBRERO chamber as shown in Fig. 3.15 is an upright cylinder with conical ends. In cross section on the inside of the chamber, the angle between the side of the cone and the side of the cylinder is 135°, which means the angle at the upper and lower vertices is 90°. Except for the location of the beam ports, the chamber is symmetric about the midplane. The cylindrical portion extends ±2.6 m, and each conical portion is 6.4 m high, making the overall internal vertical height of the chamber 18 m. At midplane the chamber radius is 6.5 m. In fact, if a 6.5 m radius sphere were to be placed at the center of the chamber, it would touch the first wall (FW) at midplane and at the conical surfaces located at a vertical height of ±4.6 m and a horizontal distance of 4.6 m from the chamber axis. These are the points on the FW at which the surface heat load will be the highest. Everywhere else, the surface heat load falls off by the ratio of $(6.5)^2/R^2$, where R is always >6.5 m.

The chamber is constructed from a 4D weave of a carbon/carbon composite. It is divided into 12 modules (i.e. every 30° on the horizontal plane). Each module extends vertically, the full height of the chamber. The modules are entirely independent of each other, having individual supply and return tubes connected to common supply and return manifolds. The target is imploded with 60 beams in a near symmetric configuration. All the beam ports lie along vertical planes at the interfaces between the modules. They also lie along ten horizontal planes with six beam ports in each plane forming a cone with the vertex at the chamber center. Five of the cones lie above midplane and have polar angles of 25.8°, 45.6°, 60°, 72.5°, and 84.3°, and there are five cones below the midplane with complimentary polar angles. Figures 3.16a and 3.16b give the horizontal distribution of the vertical planes and the five polar angles above midplane, respectively. Figure 3.17 shows the beam distribution in one octant. Note from Fig. 3.15 is that the beam ports do not face each other across from the target. Therefore, if a beam does not hit a target, it will not propagate through another beam port, but rather will hit the FW. The consequences of the beam impacting the FW are not serious, as will be shown in Section 3.2.3.3.

As mentioned earlier, the chamber is divided into 12 modules by vertical planes going through the chamber axis, rotated every 30°. The beam ports are built into the sides of the modules, half a beam port into each side. Mating the two sides of adjacent modules thus forms a single beam tube. This is done to minimize the beam obstruction on the particle flow side of the blanket. By streamlining the internal profile of the half beam port, the moving particles can flow past the beam port unobstructed. This is shown in Fig. 3.18. The twelve modules are identical in all respects except for the location of the beam ports. However, there are only two variations of beam port locations, meaning that there are two sets of six modules which are indentical in all

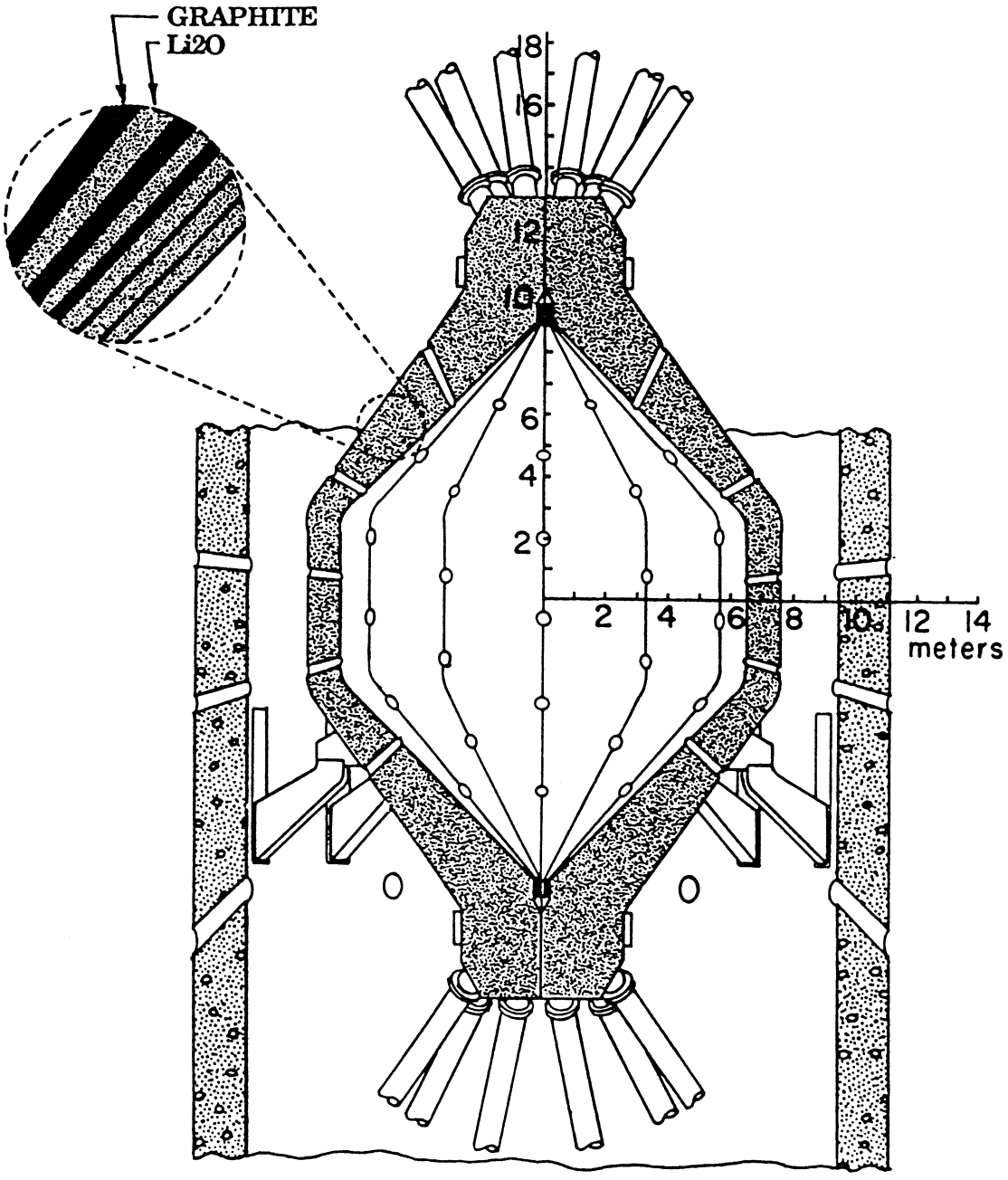

Fig. 3.15. Cross section of SOMBRERO chamber.

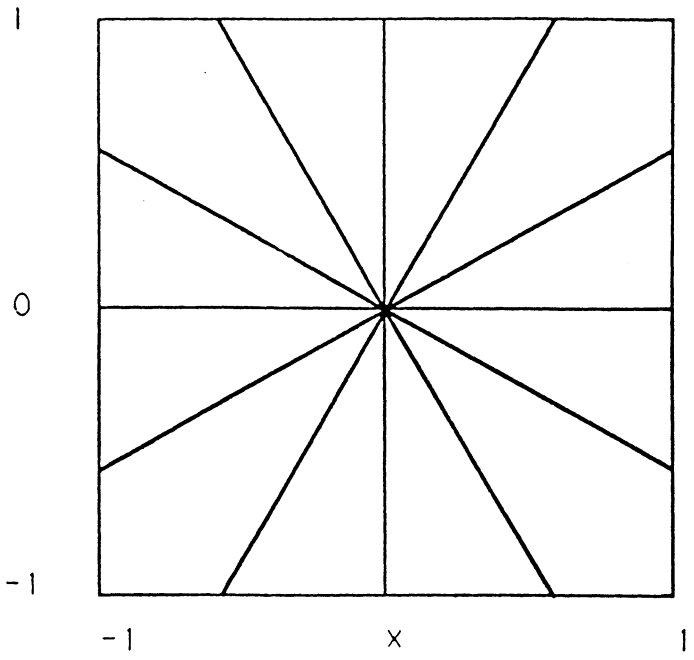

Fig. 3.16a. Azimuthal distribution of vertical planes separating modules.

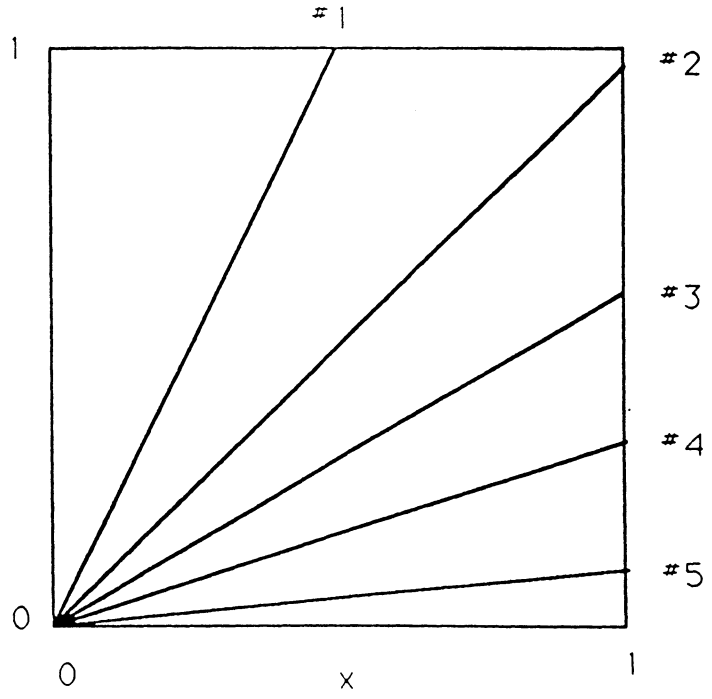

Fig. 3.16b. Five polar angles above midplane.

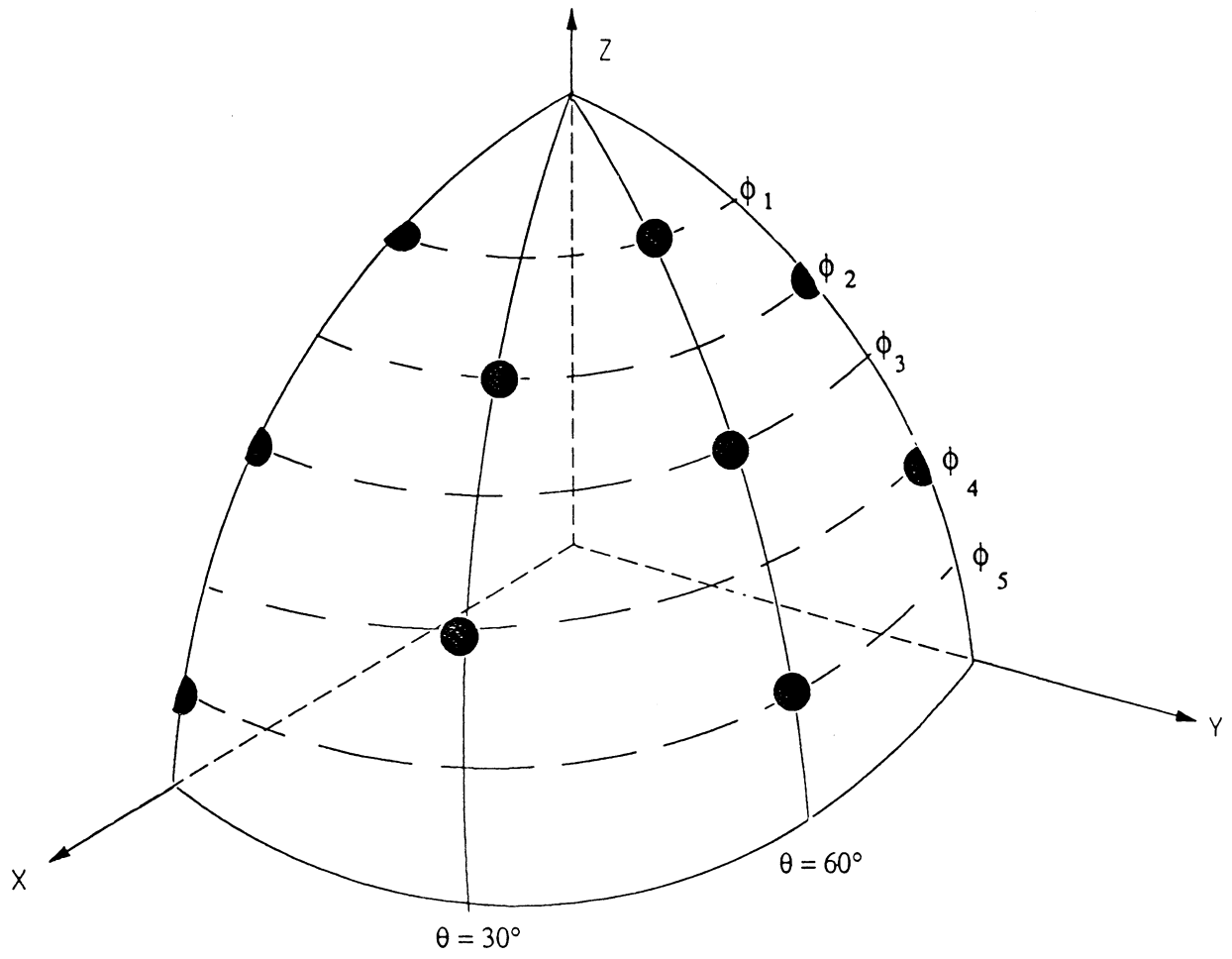

Fig. 3.17. Beam distribution in one octant of chamber.

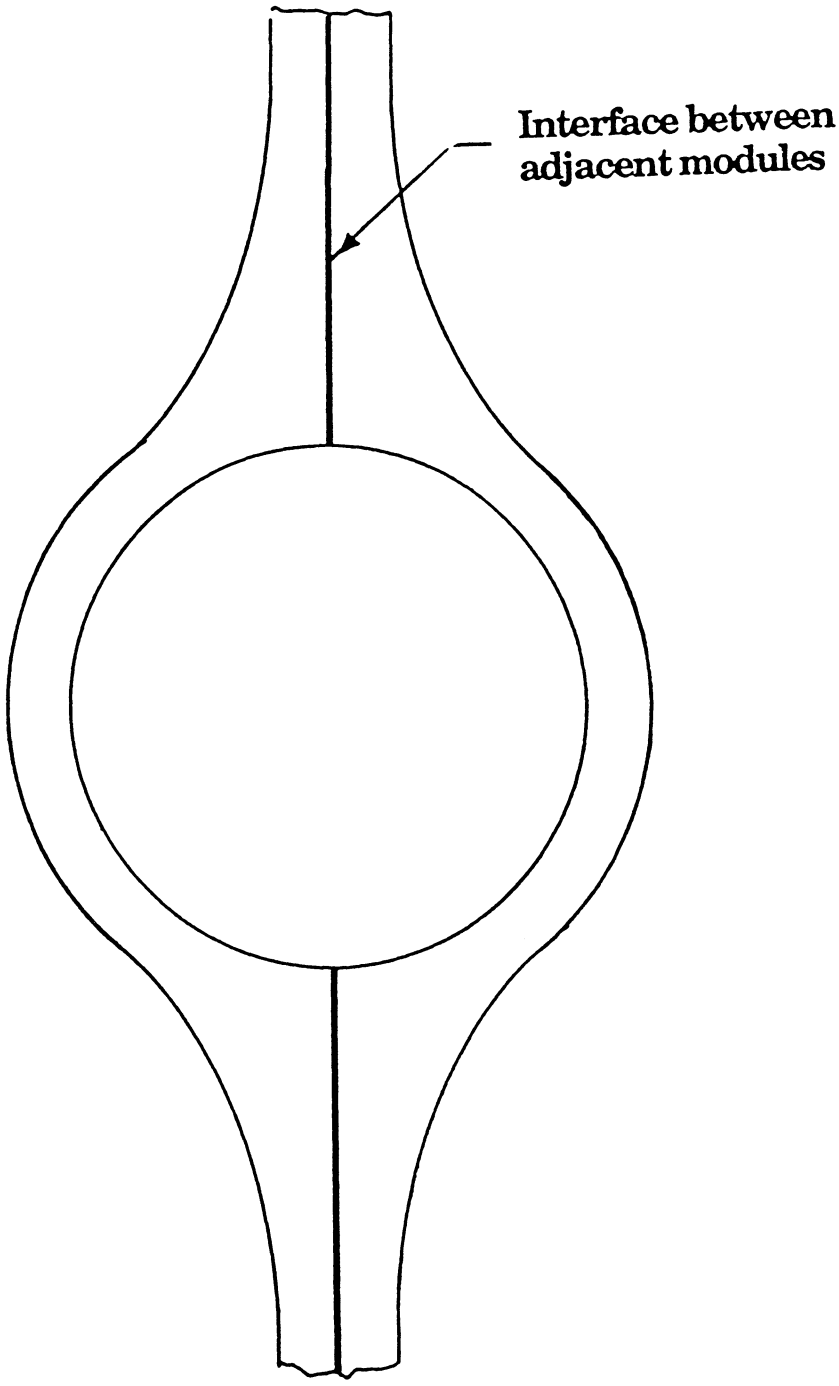

Fig. 3.18. Chamber wall profile around beam port.

respects. Figure 3.19 shows several views of the two types of modules. They are actually exact mirror images of each other. When assembled, the two types of modules are alternated such that the interface between them will form the proper beam port configuration.

Figure 3.20 is a cross section through a module at the midplane and at Z = ±5.8 m where the circumference of the FW is one half that at the midplane. Please note that in each case, the cut is taken normal to the FW, or in the case of the conical region, the cut is at 45° to the horizontal. The figure shows that the blanket/reflector is divided into five flow regions, which have a progressively higher carbon fraction from the FW to the rear. Figure 3.20 shows that the FW is attached to the back structure with radial ribs and from the target side has the appearance of an air mattress. It is curved toward the center of the chamber at a radius of 20 cm in order to minimize the stresses on the FW due to the 0.2 MPa internal pressure.

Figure 3.21 is a figure of the top half of a module with the FW removed to show how the radial ribs are arranged. At the midplane, the ribs are 21.3 cm center to center, but as they enter the conical part of the chamber, the ribs converge while the channel depth increases to make up for the decreased channel width. Finally, as the narrow region of the conical part is approached, alternate ribs are deleted altogether as shown in the figure.

Figure 3.22 shows the radial build of the blanket/reflector at the midplane as optimized by neutronic analysis. The overall thickness is 1.0 m. The FW is 1.0 cm thick and is followed by a 19 cm zone in which the carbon fraction is 3%. The second and third zones are each 40 cm thick and have 20% and 50% fraction of carbon, respectively. Increasing the carbon fraction toward the back of the blanket provides a built in reflector which gets cooled by the breeding material. The cross section at the conical region shows that the blanket/reflector was increased to a thickness of 1.75 m. It is important to note that the cumulative area of the flow channels at the FW is the same. The depth of the channels is increased to make up for the shorter circumferential extent. This is done to insure a constant high breeder material velocity of 115 cm/s at the FW where the surface heating is high. The second coolant channel also has a constant flow area from top to bottom since although this zone does not have any surface heating, it experiences a high nuclear heating. In the remaining three breeding material channels, the flow area at the extremities is reduced to 87%, 85%, and 83% relative to that at midplane, respectively. The velocity in these channels is very low, on the order of a few centimeters per second, thus, the flow area is not critical.

The breeding material chosen is granular Li_2O in the form of a moving bed. An attractive feature of Li_2O is its very high Li atom density, even higher than liquid Li, making it possible to breed without the benefit of neutron multipliers. In this design, the Li_2O particles of 300-500 μm flow through the blanket by gravity. Each module has dedicated supply and return tubes connected to common manifolds at the top and bottom. The velocity in the channel immediately behind the FW is ~115 cm/s while the average velocity in all the succeeding channels is ~12 cm/s, an order of

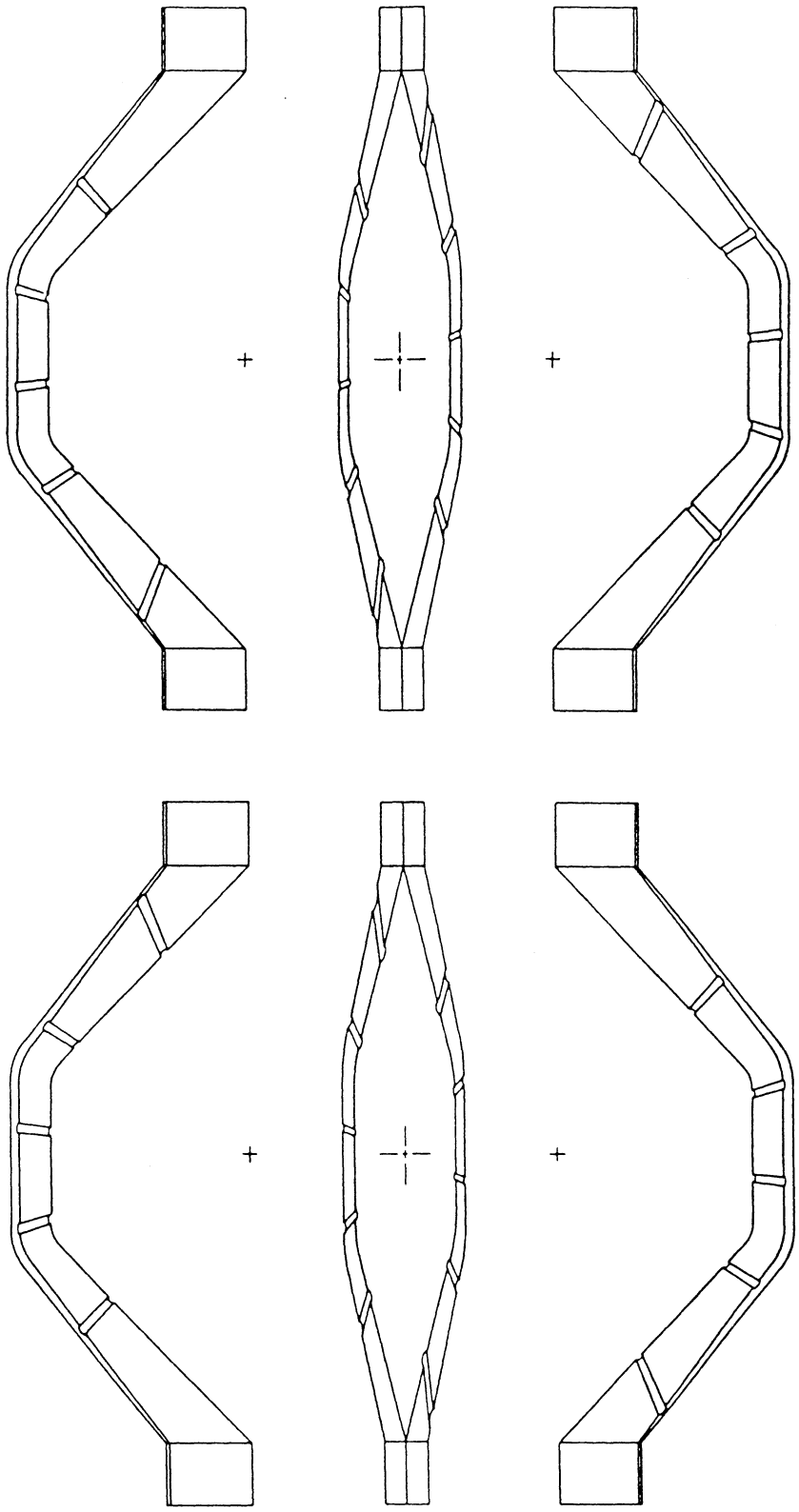

Fig. 3.19. Several views of the two types of modules.

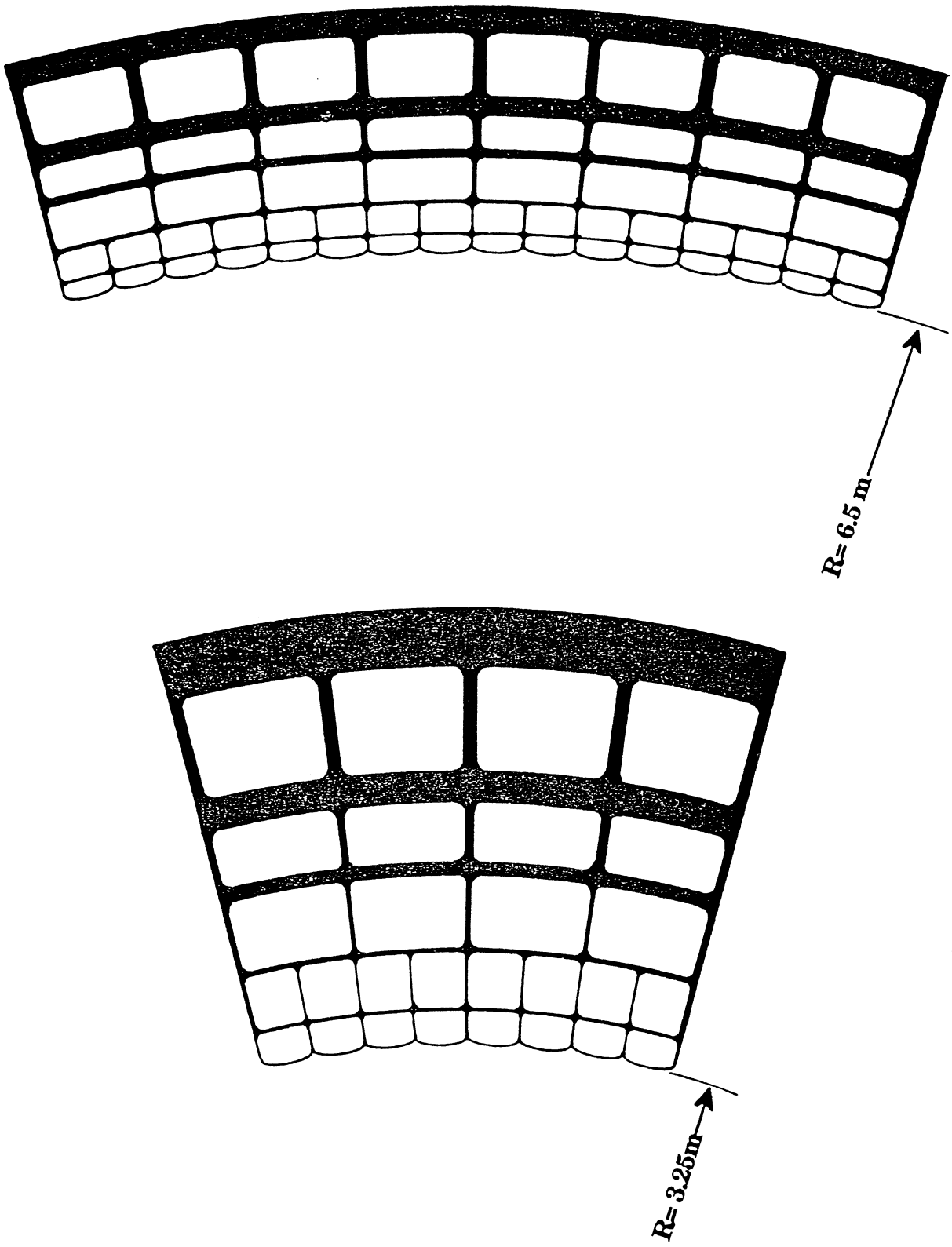

Fig. 3.20. Cross section through a module at midplane and at Z = 5.8 m.

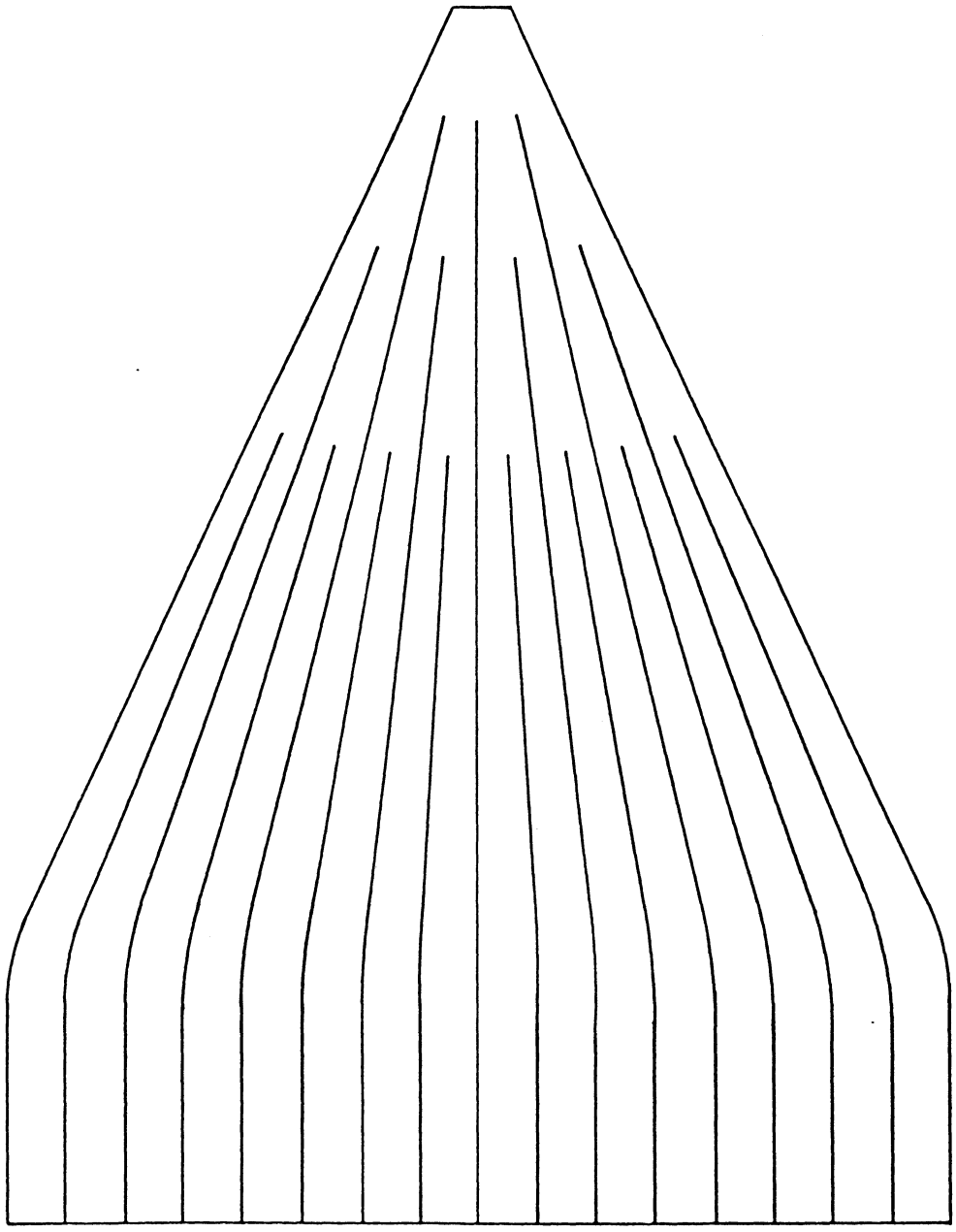

Fig. 3.21. Distribution of FW radial supports - upper half of module.

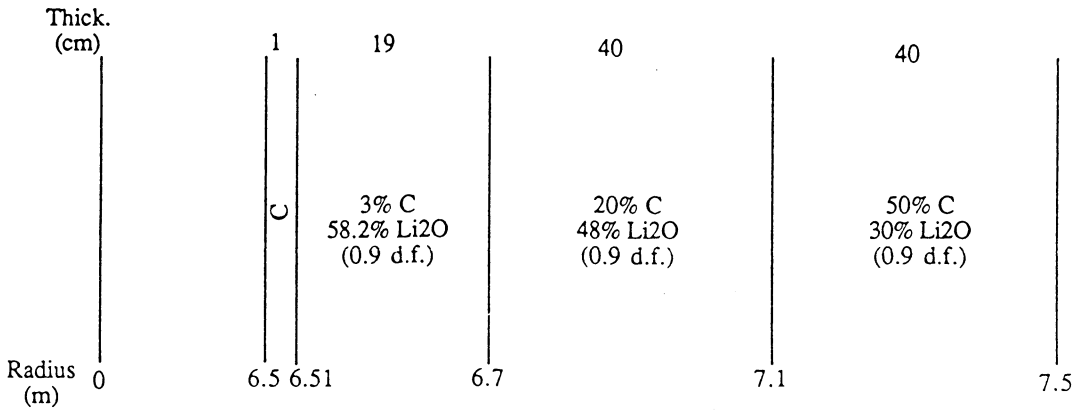

Fig. 3.22. Radial build of blanket at midplane.

magnitude lower. Of the total mass flow rate through the reactor of 5490 kg/s, 57% goes through the FW channel, while the remaining 43% goes through the rest of the channels. The theoretical density of Li_2O is 2.01 g/cm^3, but we assume that the material is 90% density, and the moving bed has a 60% Li_2O fraction, giving the effective density a value of 1.08 g/cm^3. The pressure of the He carrier gas in the blanket is 0.2 MPa and since the chamber is at 0.5 torr, the absolute pressure on the FW is 0.3 MPa. In the next section, finite element stress analysis of the FW is described.

The inlet temperature of the Li_2O into the chamber is 550°C. At the FW, the outlet temperature is 700°C and at the back, 800°C, but the equilibrated outlet temperature from the chamber is 743°C. Table 3.6 gives the physical parameters of the SOMBRERO chamber.

Table 3.6. Physical Parameter of SOMBRERO Chamber

Material of Construction	4D Weave C/C Composite
Chamber Radius at Midplane (m)	6.5
Overall Internal Chamber Height (m)	18
Number of Modules in Chamber	12
Number of Beam Ports in Chamber	60
Structural Mass Per Module (Tonnes)	37.8
First Wall Thickness (cm)	1.0
Radius of Curvature of FW Between Ribs (m)	0.2
Thickness of FW Ribs (cm)	1.0
Number of Ribs per Module at Midplane	17
Maximum Stress in FW (MPa)	42.9

Stress Analysis of the First Wall. The ANSYS finite element code was used for the first wall stress analysis. Material properties used in the analysis are given in Table 3.7[3.11] where the UVW directions are in one plane with the fibers laid 60° apart, and the Z direction is perpendicular to the primary fiber plane.

Table 3.7. Physical Properties of 4D Weave C/C Composites

	Z Direction	U,V,W Direction
Tensile Modulus (GPA)		48.3
Compressive Modulus (GPA)	110.3	41.4
Tensile Strain (%)		0.14
Compressive Strain (%)	1.3	0.12
Poissons Ratio	0.02 - 0.1	
Coefficient of Expansion (cm/cm °C)	5×10^{-7}	

The FW has a radius of curvature of 20 cm and a thickness of 1.0 cm. Figure 3.23 shows how the FW was modelled for ANSYS. Because of symmetry, only one half of a FW channel was modelled, showing one FW radial support and only one half of the FW in the channel attached to it. The location of the point of analysis is at Z = -4.6 m, where the FW surface heat load and temperature peak. This is the worst spot since the thermal stress will be lower everywhere else. Figure 3.23 shows that the radial support is fixed, but the FW is allowed to expand outward under the actions of the internal pressure and thermal stress.

Figures 3.24 and 3.25 show the FW stress distribution due to the internal pressure of 0.3 MPa in the X and Y directions, respectively. The X direction is perpendicular to the FW, and the Y direction is parallel to it. As expected, these stresses are very low, with the highest being 10.6 MPa in the Y direction at the corner between the radial support and the FW. At the FW midway between the supports, the maximum stress is ~6 MPa, or the value which is obtained from a simple $\sigma = pr/t$ for cylindrical geometry, where p is the pressure, r is the radius of curvature, and t the thickness.

Figures 3.26 and 3.27 show the stress distribution, again in the X and Y directions with the secondary thermal stress superimposed. Here the stress in the X direction is low, 8.5 MPa, but in the Y direction it is 42.9 MPa. The maximum stress again occurs at the corner between the radial support and the FW. In the actual case, there would be a rounded transition at this point, and the stress concentration would be reduced.

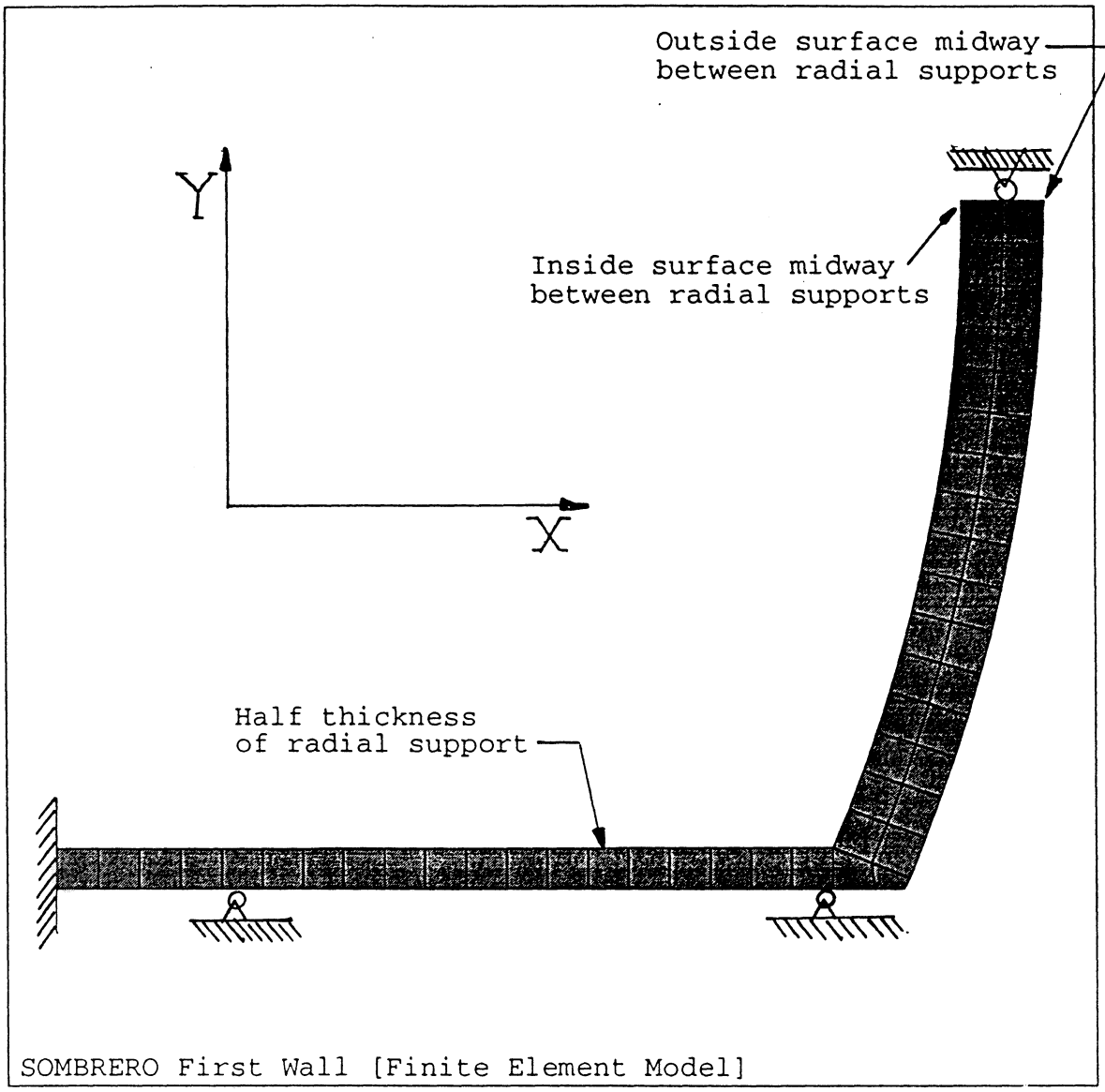

Fig. 3.23. First wall modeling for ANSYS.

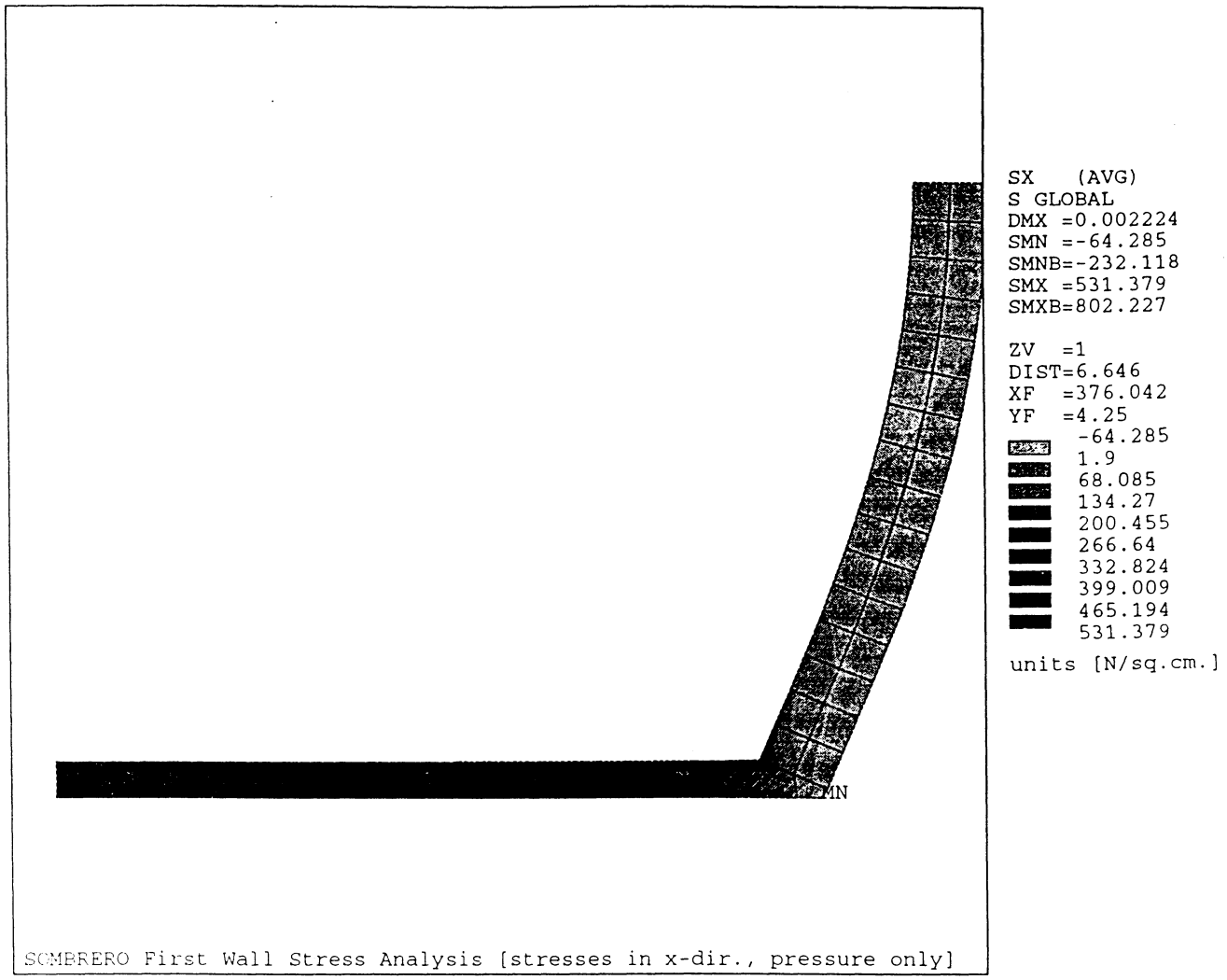

Fig. 3.24. First wall stress distribution in the X direction (perpendicular to FW) due to internal pressure of 0.3 MPa.

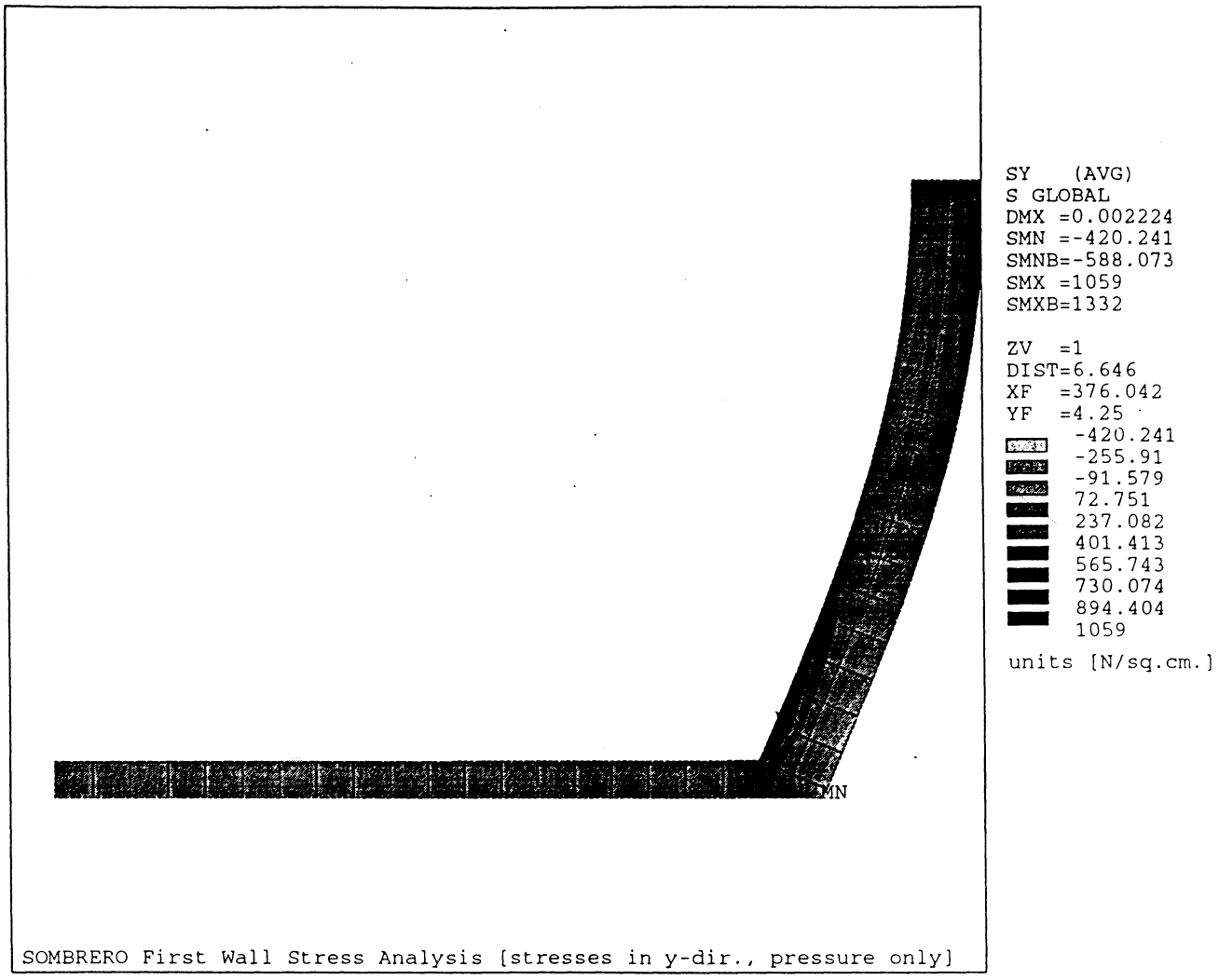

Fig. 3.25. First wall stress distribution in the Y direction (parallel to FW) due to internal pressure of 0.3 MPa.

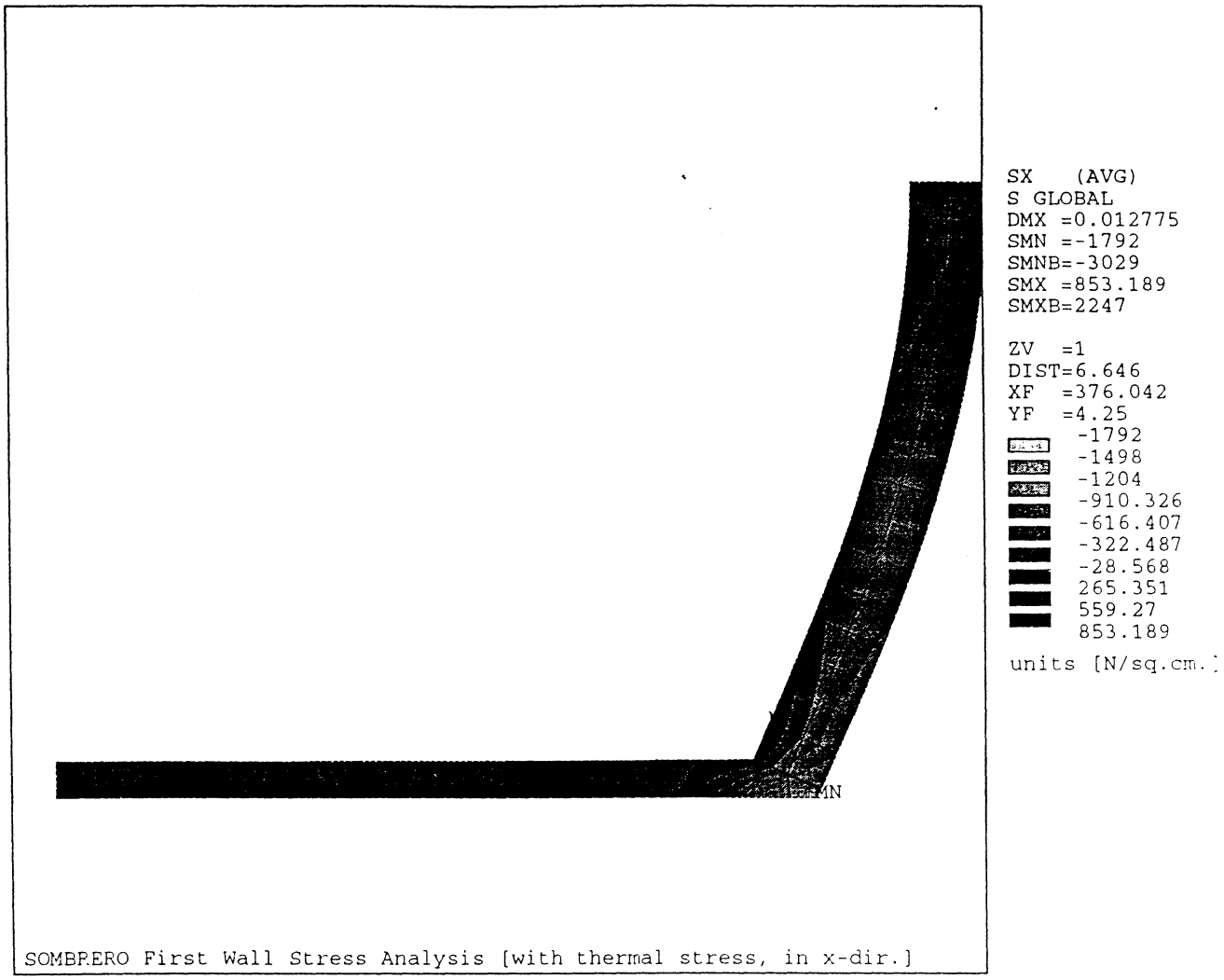

Fig. 3.26. First wall stress distribution in the X direction due to internal pressure and thermal stress.

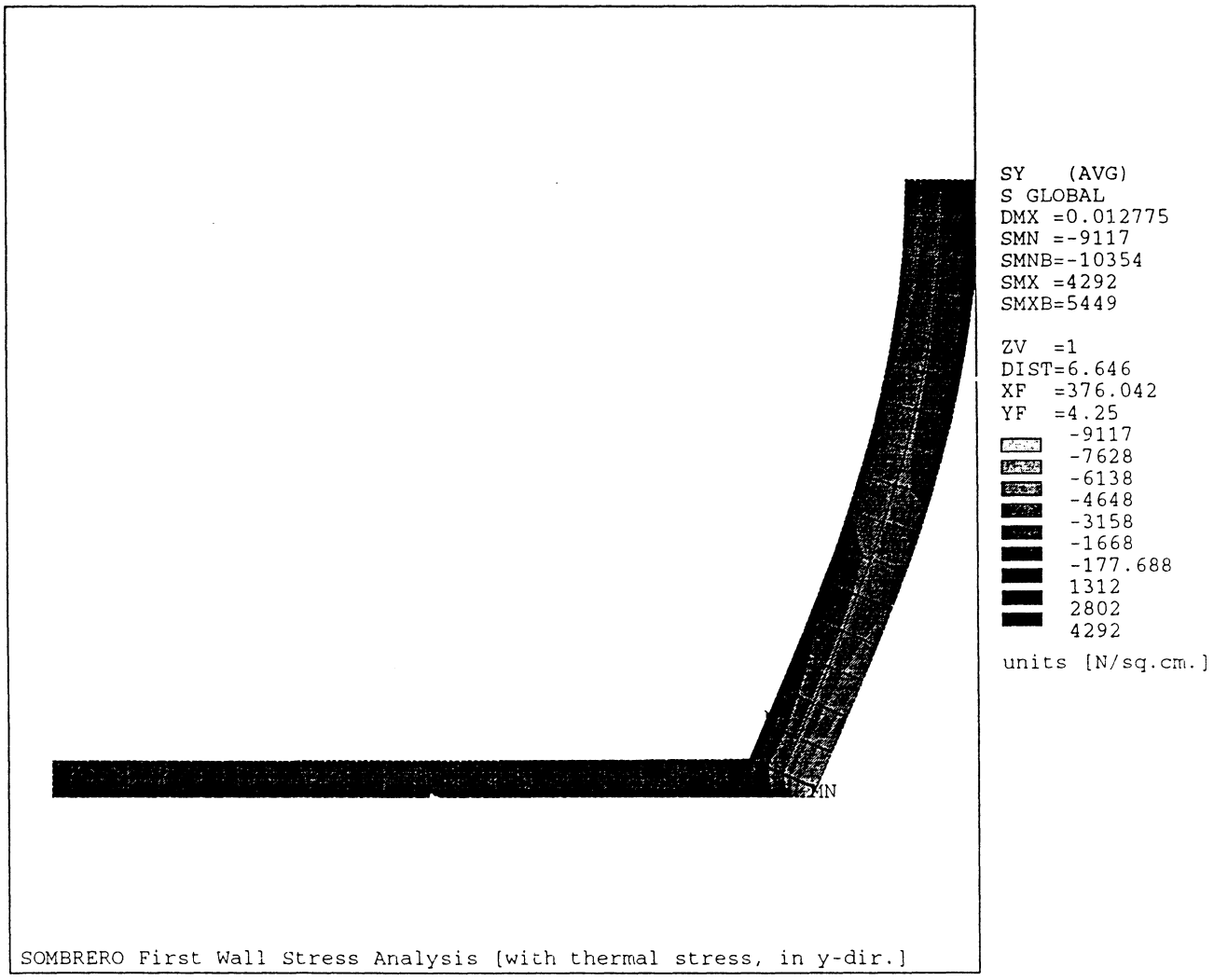

Fig. 3.27. First wall stress distribution in the Y direction due to internal pressure and thermal stress.

Structural characteristics of 3D and 4D weaves of C/C composites vary by quite a lot, depending on the manufacturer. Tensile strength can vary from 50-300 MPa and shear strength from 20-40 MPa[3.11]. The feature that distinguishes these materials from others is that they actually become stronger at higher temperatures. For example, some 3D and 4D C/C composites display a 25% increase in tensile strength at 2000°C as compared to room temperature strength. Thus, it would seem that a material with tensile strength of 100-150 MPa would be sufficient for use in the FW.

Finally, Fig. 3.28 gives the radial deflection of the FW under the combined action of pressure and thermal stress. The maximum displacement if the FW midway between radial supports is only 0.013 cm.

3.2.3.2 Materials and Fabrication

Structural Materials. The first wall in SOMBRERO is protected with a buffer gas of 0.5 torr Xe. This dry wall protection scheme puts stringent requirements on the FW materials. They should have high temperature capability, reasonably high thermal conductivity, and a combination of properties which will give a low thermal stress.

Figure 3.29 is a compilation[3.12] of the thermal stress figure of merit for various materials that have been considered for high heat flux plasma facing components. The thermal stress figure of merit is given by

$$\frac{2(1 - \nu)k\sigma_y}{E\alpha} \quad (W/cm)$$

where

ν = Poisson's ratio,
k = thermal conductivity,
σ_y = yield strength,
E = Young's modules, and
α = thermal expansion coefficient.

The C/C composites lead the way by a healthy margin over other ceramic and metallic materials. Carbon/carbon composites are attractive for high heat flux surfaces because of their high thermal conductivity of ~100 W/mK in a direction perpendicular to the fibers in 3D and 4D C/C composites.[3.13] In a direction parallel to the fibers, conductivity as high as 500 W/mK has been obtained. This compares favorably with copper, which has a conductivity of 400 W/mK at 25°C.

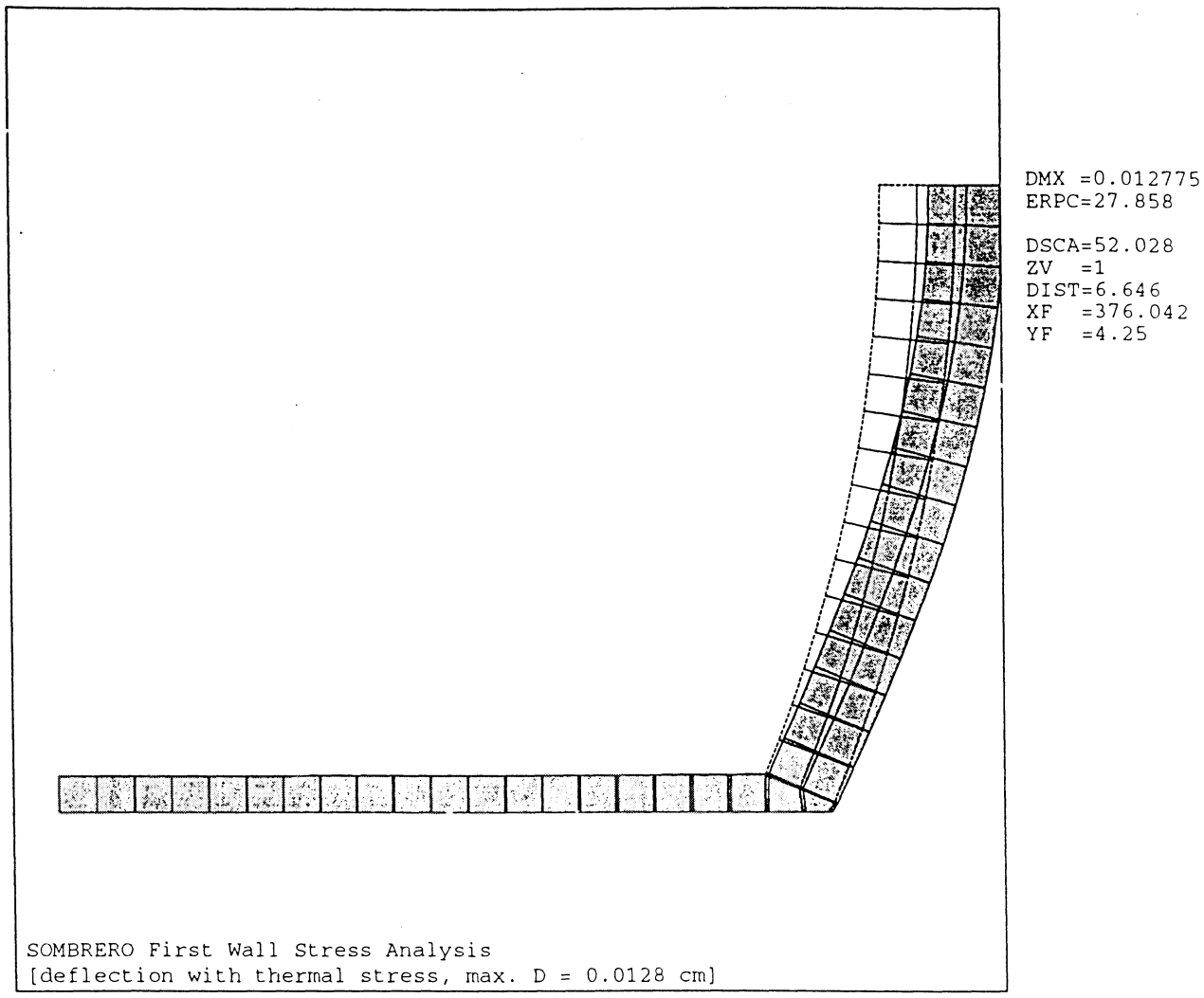

Fig. 3.28. First wall deflection under the combined action of internal pressure and thermal stress.

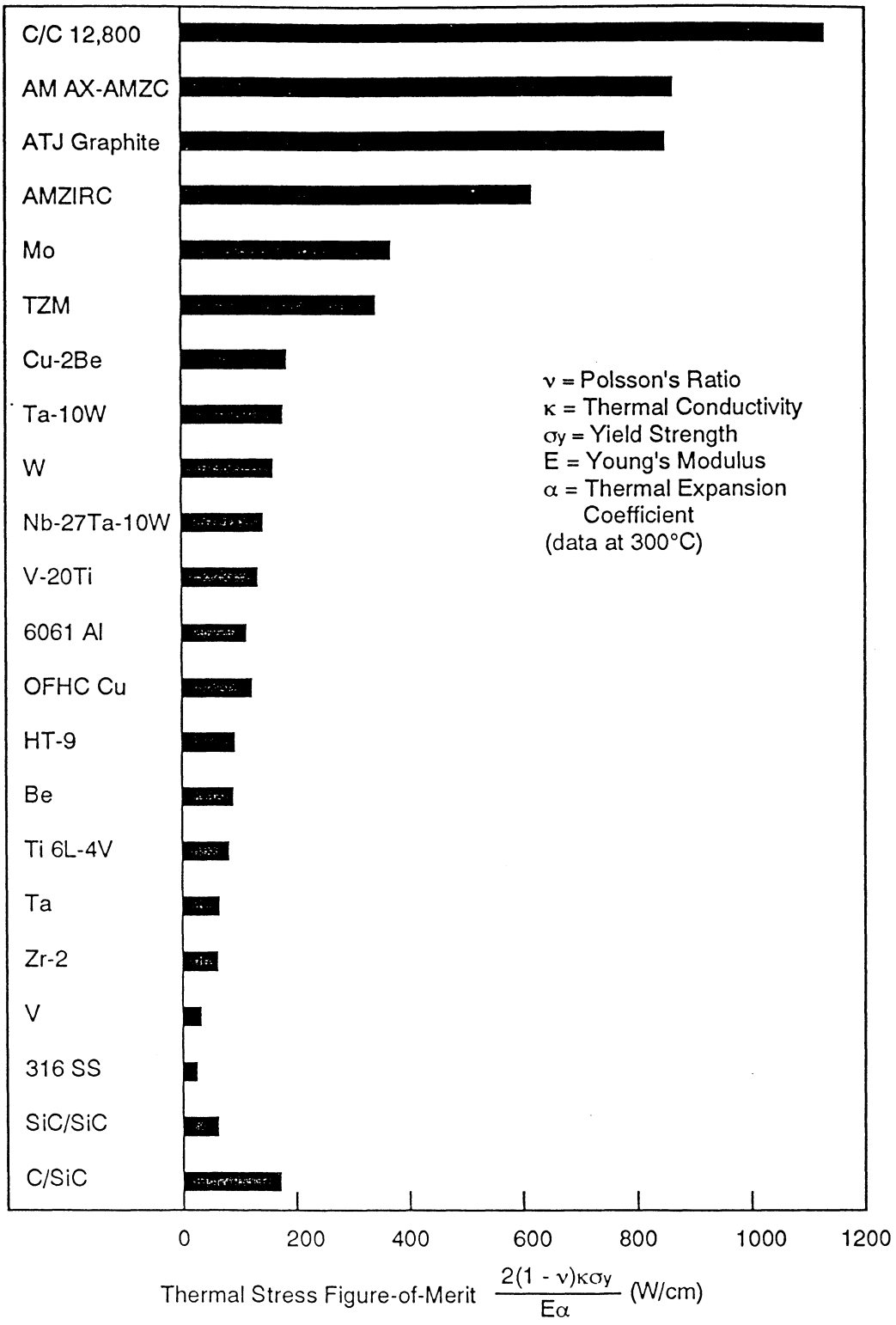

Fig. 3.29. Thermal stress figures of merit for several materials.

There are several other properties of C/C composites which make them attractive for such an application. They are

- High strength, tensile, compressive, and shear[3.11]
- They get stronger at high temperatures[3.11]
- Very low neutron activation

These are among the reasons a C/C composite material has been selected for the SOMBRERO chamber structure.

Although there is some information on radiation damage in pyrolytic graphite, there is none available on 3D and 4D C/C composites. During high temperature irradiation, graphites first experience shrinking or densification and then expand at a rapid rate. Figure 3.30 shows the results for GRAPHNOL N3M for example.[3.13] Useful lifetimes are usually determined when the dimensional change crosses the zero swelling line. The figure shows that for Graphnol N3M this value is 46 dpa at 1325°C. With improved material engineering, these values will go up, and for the present design we have assumed a limiting value of 75 dpa, which gives the FW a lifetime of 5 FPY.

Four dimensional C/C composites are constructed by running fibers in three directions in one plane, 60 degrees apart, commonly called the U,V, and W directions. The fourth direction, called Z, is perpendicular to this plane. When the weave is completed it undergoes a densification. It is first rigidized by chemical vapor deposition (CVD) or low pressure infiltration (LPI) by a hydrocarbon. The last step is called graphitization where the hydrogen is burned out of the hydrocarbon. This results in a composite weave with a density of 1.85-2.0 g/cm^3.

Some extremely complex shapes have been fabricated in these ways for the defense industry, such as very large reentry nose cones for rockets. Although the chamber modules are very large and fairly complex, it is felt that in 30-40 years, when such fusion reactors will be built, the manufacturing methods will have improved to the point where such items can be fabricated routinely.

Breeding Material. The breeding material selected for SOMBRERO is Li_2O in the form of flowing particles 300-500 μm in size. At a recent International Thermonuclear Engineering Reactor (ITER) specialists meeting on blanket materials data base, it was reported that with regard to baseline physical properties of ceramic breeders, the data base for Li_2O and $LiAlO_2$ is reasonably complete.[3.14] Tritium solubility and transport have been studied in significant detail for Li_2O, which is the only breeder material for which single-crystal tritium diffusion measurements have been made. Table 3.8 summarizes the data base assessment for Li_2O, and Table 3.9 is a summary of four recommended ceramic breeders.[3.14] Of these four, only Li_2O has a high enough Li atom density (even higher than Li) for adequate tritium breeding without neutron multiplication.

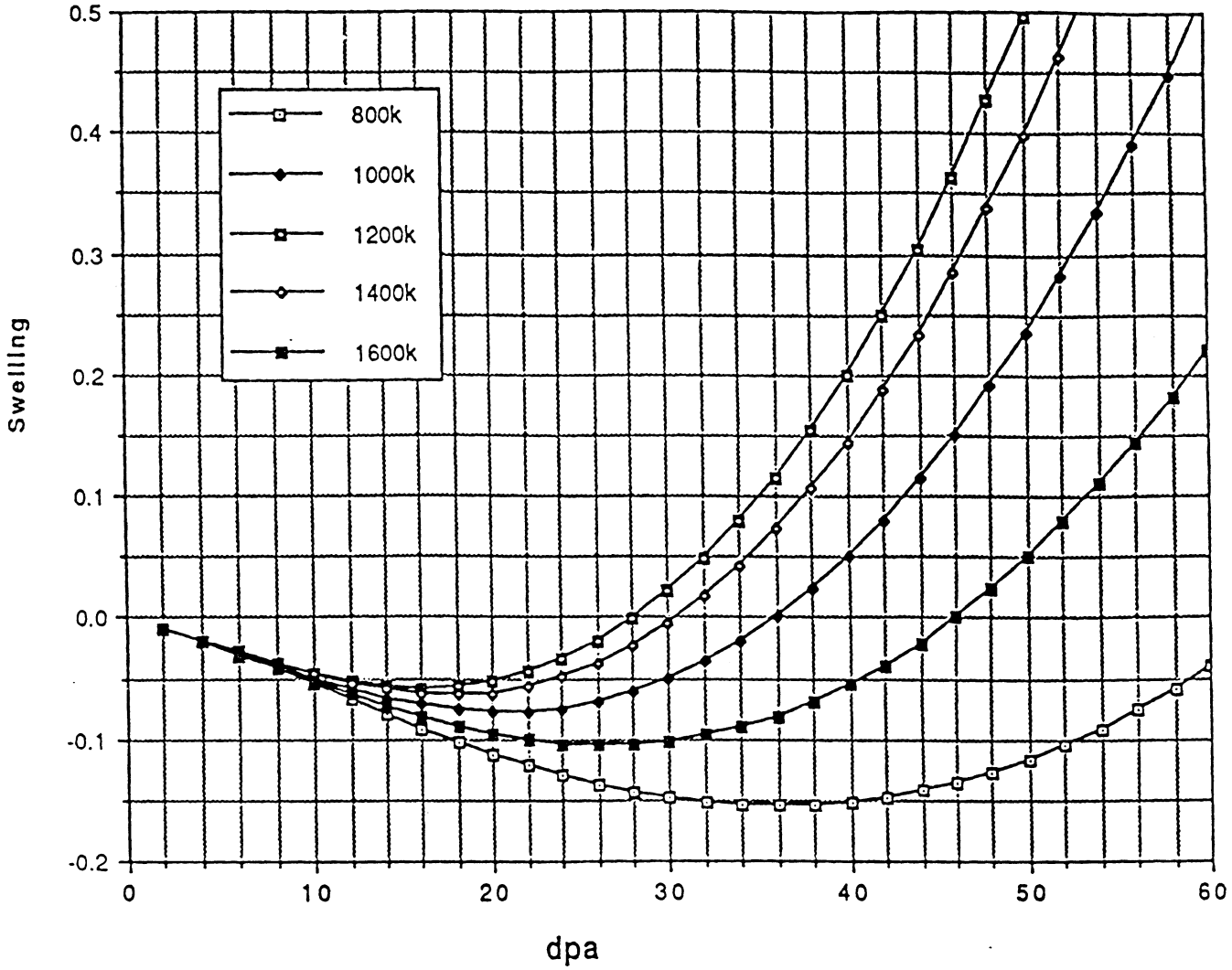

Fig. 3.30. Radiation swelling in Graphnol N3M as a function of temperature and fluence.

Table 3.8. Li_2O Data Base Assessment (Ref. 3.14)

Physical Properties	
Density	Adequate/good agreement
Melting temperature	Adequate/good agreement
Vapor pressure	Limited/general agreement
Thermal expansion	Adequate/good agreement
Thermal conductivity	Limited/general agreement
Specific heat	Adequate/good agreement
Mechanical Properties	
Elastic modulus	Limited/general agreement
Poisson's ratio	Limited/general agreement
Tensile strength	Very limited
Compressive strength	Single set of data
Bending strength	Single set of data
Chemical Stability / Compatibility	
Composition/purity	Adequate/good agreement
Stability	Adequate/good agreement
Vapor pressure/transport	Adequate/good agreement
Compatibility w/water	Limited/general agreement
Tritium Solubility / Transport	
Tritium solubility	Limited/some discrepancies
Tritium diffusivity	Adequate/good agreement
Adsorption/desorption	Limited/some discrepancies
Radiation Effects	
Swelling	Single set of date
Tritium trapping/transport	Limited/some discrepancies
Helium trapping/transport	Single set of data
Fracture properties	Single set of data

Table 3.9. Summary of Recommended Ceramic Breeders (Ref. 3.14)

	Li_2O	Li_4SiO_4	Li_2ZrO_3	$LiAlO_2$
Li Atom Density	G	F	F	F
Large Scale Production Feasibility	F	F	F	F
Activation	G	G	P	F
Thermal Conductivity	G	P	P	F
Melting Point/Phase Change	G	F	G	G
Thermal Expansion	F	F	G	G
Mechanical Strength	F	F	G	G
Creep/Ductility	F	P	P	P
Chemical Stability	F	F	G	G
Water Compatibility	P	F	F	G
Structural Compatibility	F	F	G	G
Li Mass Transfer	KI	G	G	G
Tritium Solubility	F	F	F	F
Tritium Release (Transport)	G	F	G	P
Irradiation Effects on Physical Properties	G	G	G	G
Irradiation Swelling	P	F	G	G
Irradiation Stability	F	P	G	F
Radiation Effects (T-transport, Compatibility)	KI	KI	KI	KI

G - Good, F - Fair, P - Poor, KI - Key Issue

From Table 3.8 it is obvious that for the application intended in this reactor, Li_2O has good credentials. Water compatibility and irradiation swelling were judged poor for Li_2O. For this reason we have opted for a Pb intermediate loop, to prevent water from coming in contact with Li_2O. As far as irradiation swelling, this is much less significant in a moving bed than in a static bed. The key issues listed are Li mass transfer and radiation effects on T_2 transport and compatibility. Here again, these issues have more relevance to static beds. A moving bed can have a continuous reprocessing side loop which can maintain the desired properties.

The melting temperature of Li_2O as listed in the *Handbook of Chemistry and Physics* is >1700°C. However, this somewhat depends on the purity of the material. A more typical value is 1432 ± 6°C for commercially produced material.[3.15]

The following correlations were used to evaluate the properties needed for thermal hydraulics calculations:

Specific Heat (kJ/kg K) for temprerature range of $306 \leq T \leq 1073$ K (Ref. 3.16)

$$C_p = 2.5179 + 3.328 \times 10^{-4} T - 8.382 \times 20^4 / T^4$$

Thermal Conductivity (W/mK) for temperature range of $473 \leq T \leq 1172$ K (Ref. 3.17)

$$k = (1 - P)^{1.96} [39.79 (1 + 7.067 \times 10^{-3} T)^{-1}]$$

where P is the porocity ($0.066 \leq P \leq 0.292$)

3.2.3.3 Thermal Hydraulics

Heat transfer in moving beds is dominated by the effective thermal conductivity of the solid and the interstitial gas instead of by the conductivity of the gas alone, as is the case in fluidized beds. For this reason, heat transfer coefficients in moving beds are higher than those for fluidized beds using the same material.[3.18]

The most critical cooling part in SOMBRERO is the FW. Figure 3.31 gives the nuclear heating distribution through the blanket at midplane. As can be seen, the nuclear heat generation in the front part is significantly higher than in the rear zones. In addition, the FW receives heat radiated to it by the Xe fill gas after the ions and soft x rays have been stopped. The front channel at the FW must, therefore, remove the nuclear heat generated in the graphite FW and the Li_2O in the channel, as well as all the surface heat incident on it from the fill gas. This amounts to 44% of the total thermal power in the reactor. Moreover, since the ΔT in the FW channel is only 150°C, and in the rear channels it is 250°C, the mass flow rate in the FW channel is 57% of the total mass flow rate. Figure 3.32 gives the mass flow rate in each blanket channel, and Fig. 3.33 gives the velocity in each channel at midplane (channel 1 is at the FW). These velocities are based on a void fraction of 40% and an equivalent Li_2O density of 1.08 g/cm^3. The Li_2O specific heat at the FW at an average temperature of 625°C was taken as 2713 J/kgK and in the rear zones at 675°C as 2740 J/kgK.

For determining the heat transfer coefficient at the FW, it was decided to treat the Li_2O moving bed as a continuum. This decision was taken after an extensive investigation into moving bed heat transfer research going back to 1955. It was found that most of the research gave formulations for heat transfer coefficients which depended on times or distances particles spent on the heated surface, parameters which are impossible to predict for SOMBRERO. Mickley and Fairbanks[3.19] derived a correlation for the local heat transfer coefficient based on particle residence time on the heated surface. Baskakov[3.20,3.21,3.22] introduced a contact resistance at the heated wall to allow for heat transfer impedance due to increased voidage at the wall. But their

correlations also depended on the mean residence time a particle spent on a heated surface. Gelperin[3.23,3.24] developed this approach further and derived expression for the overall heat transfer coefficient. Sullivan and Sabersky[3.25] made a series of experiments using flowing beds of glass beads, mustard seed and fine grained sand. They obtained Nusselt numbers based on a modified Peclet number which depended on L, the distance a particle stayed in contact with a heated surface:

$$N_{Pe} = N_{Re}\, N_{Pr}$$

$$N^{*}_{PeL} = \left(\frac{k}{k_g}\right)^2 \left(\frac{d}{L}\right)^2 N_{Pe}$$

where

N^{*}_{PeL} = modified Peclet number
k = effective bed thermal conductivity
k_g = gas thermal conductivity
d = particle diameter
L = distance a particle stays in contact with the heated surface.

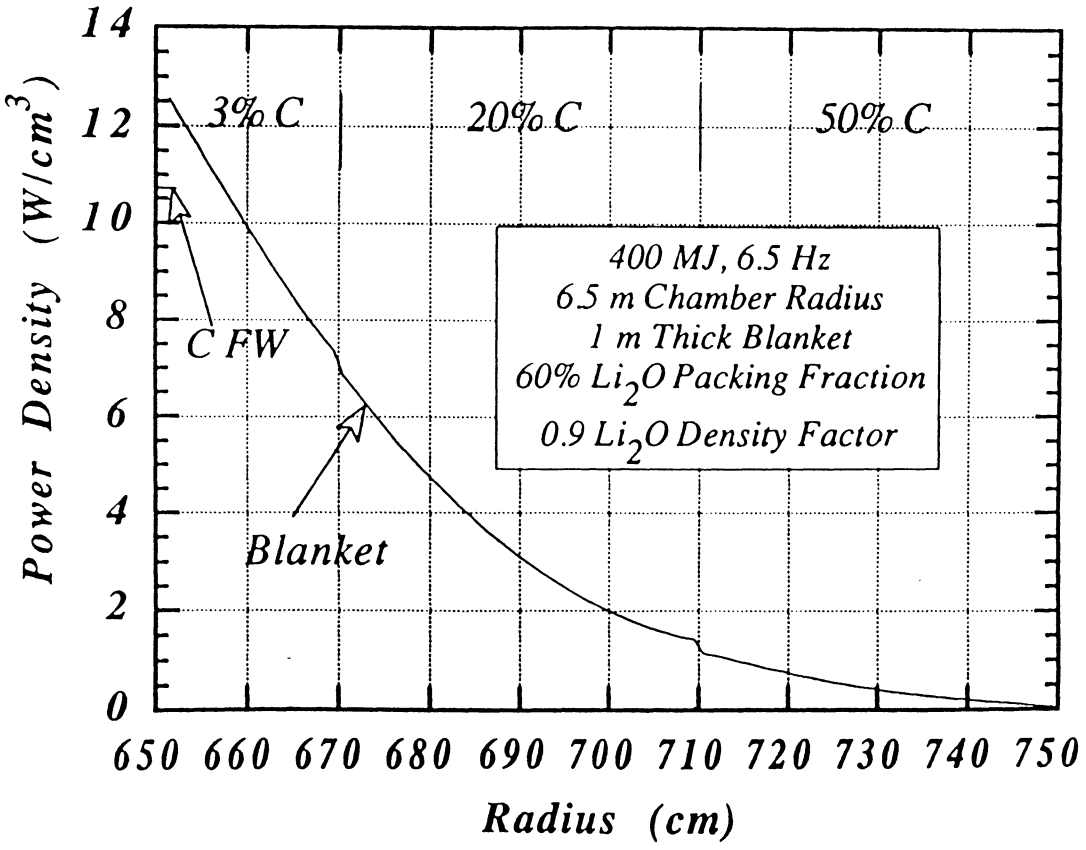

Fig. 3.31. Nuclear heating distribution at midplane.

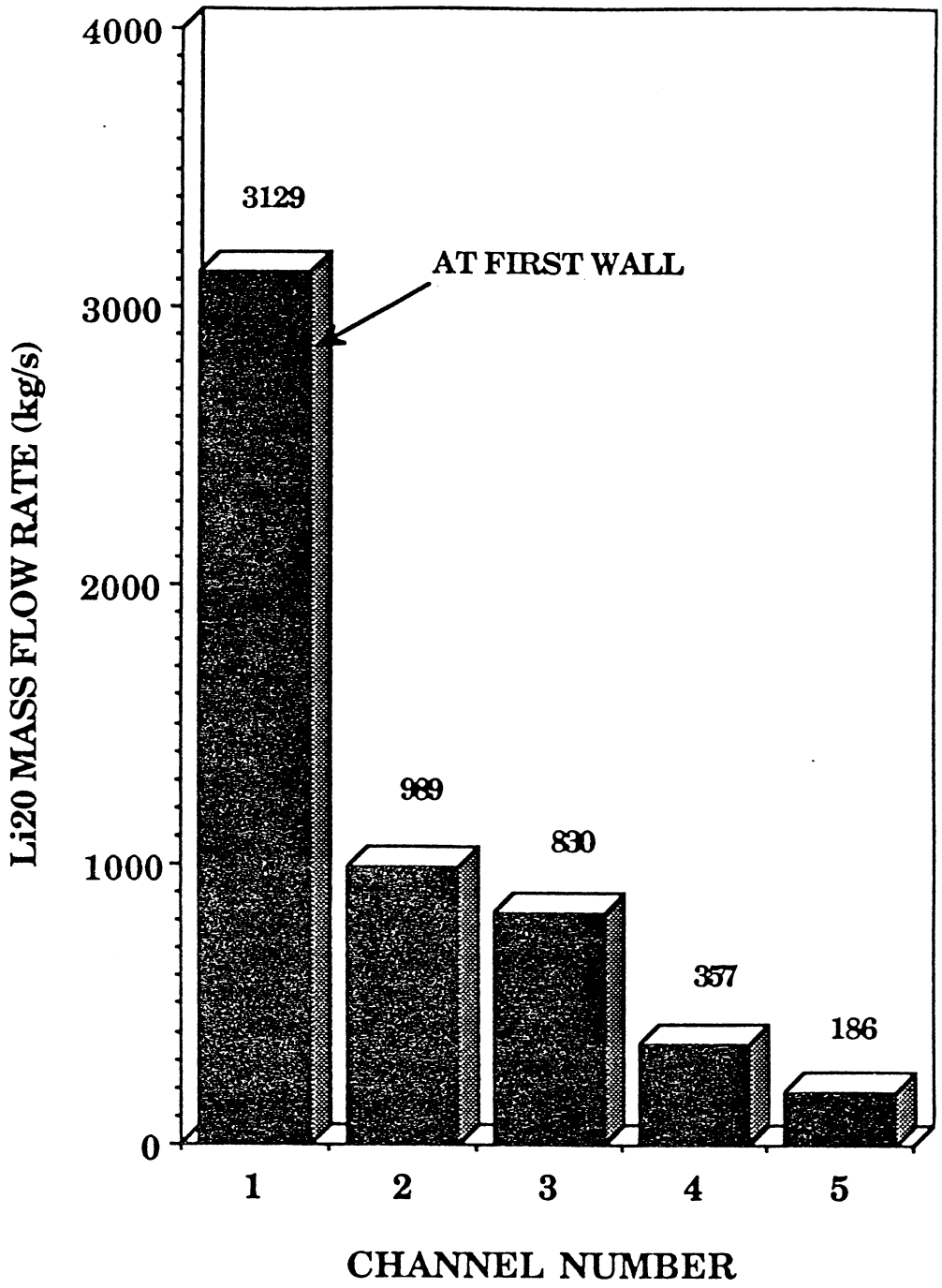

Fig. 3.32. Mass flow rate in the blanket channels.

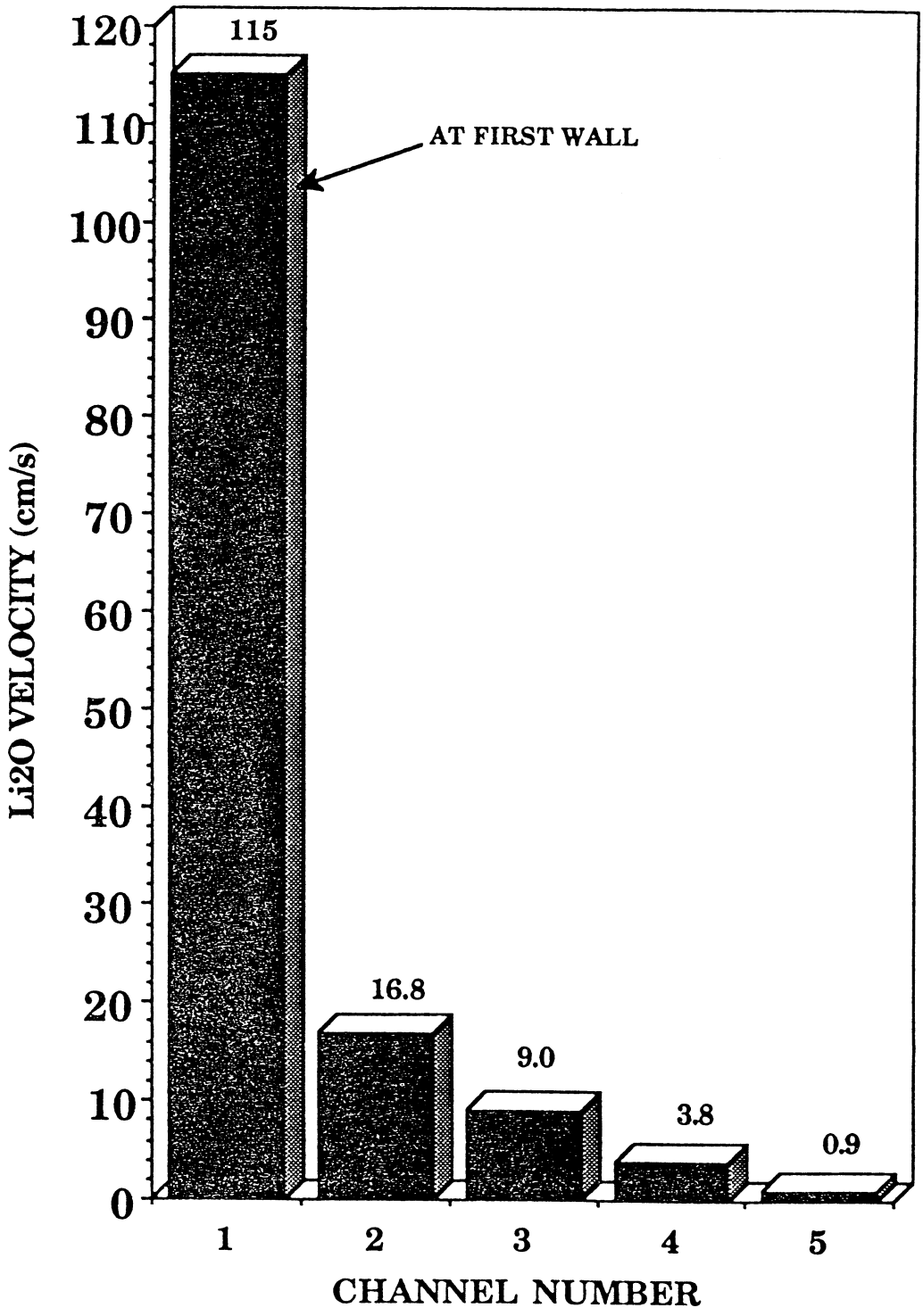

Fig. 3.33. Li_2O velocity at midplane in the blanket channels.

The Nusselt number is then:

$$N_{Nu} = \frac{h \cdot d}{k_g} = \frac{1}{\chi - \frac{\sqrt{\pi}}{2} \cdot \sqrt{\frac{1}{N^*_{PeL}}}}$$

where h is the heat transfer coefficient, and χ is a constant taken as 0.085 for the materials tested.

Figure 3.34 is a plot of local heat transfer coefficients as a function of moving bed velocity for sand particles of 500 μm and 1000 μm size at 400°C and 800°C using the Sullivan and Sabersky formulation for L = 1.0 cm. It can be seen that values of h approaching 2600 W/m^2K can be had for a velocity of 110 cm/s for particles of 500 μm size at 800°C. Since there is a lot of mixing going on at velocities greater than ~40 cm/s, an $L \leq 1$ cm is not unreasonable.

In order to be able to use the Li_2O stream as a continuum, the effective viscosity of the particles as a function of velocity has to be obtained. To obtain the effective viscosity, experiments performed by R. Nietert[3.26] at the University of Wisconsin in 1981 were used. The experiments involved flowing soda lime glass beads in electrically heated tubes. Nusselt numbers were obtained experimentally from three different particle size ranges in three different size tubes for a velocity range from 0.5-20 cm/s. The following parameters were known:

- Particle size
- Tube ID
- Inlet temperature
- Outlet temperature
- Velocity
- Density
- Void fraction
- Gas conductivity
- Solid conductivity
- Solid specific heat
- Heat flux

The Nusselt numbers were used to derive the effective viscosities for moving beds using the Dittus Boelter formulation. These effective viscosities for the same particle sizes and void fractions were plotted against velocity for the same heat flux and an analytic expression was obtained. There was a definite trend at the higher velocity values, thus, the curve was extrapolated to the velocity of interest. Since Li_2O is harder than soda lime glass, it is expected that the effective viscosities might be lower yet, making these values conservative. Figure 3.35 is a plot of the obtained effective viscosities for 500 μm size soda lime glass particles.

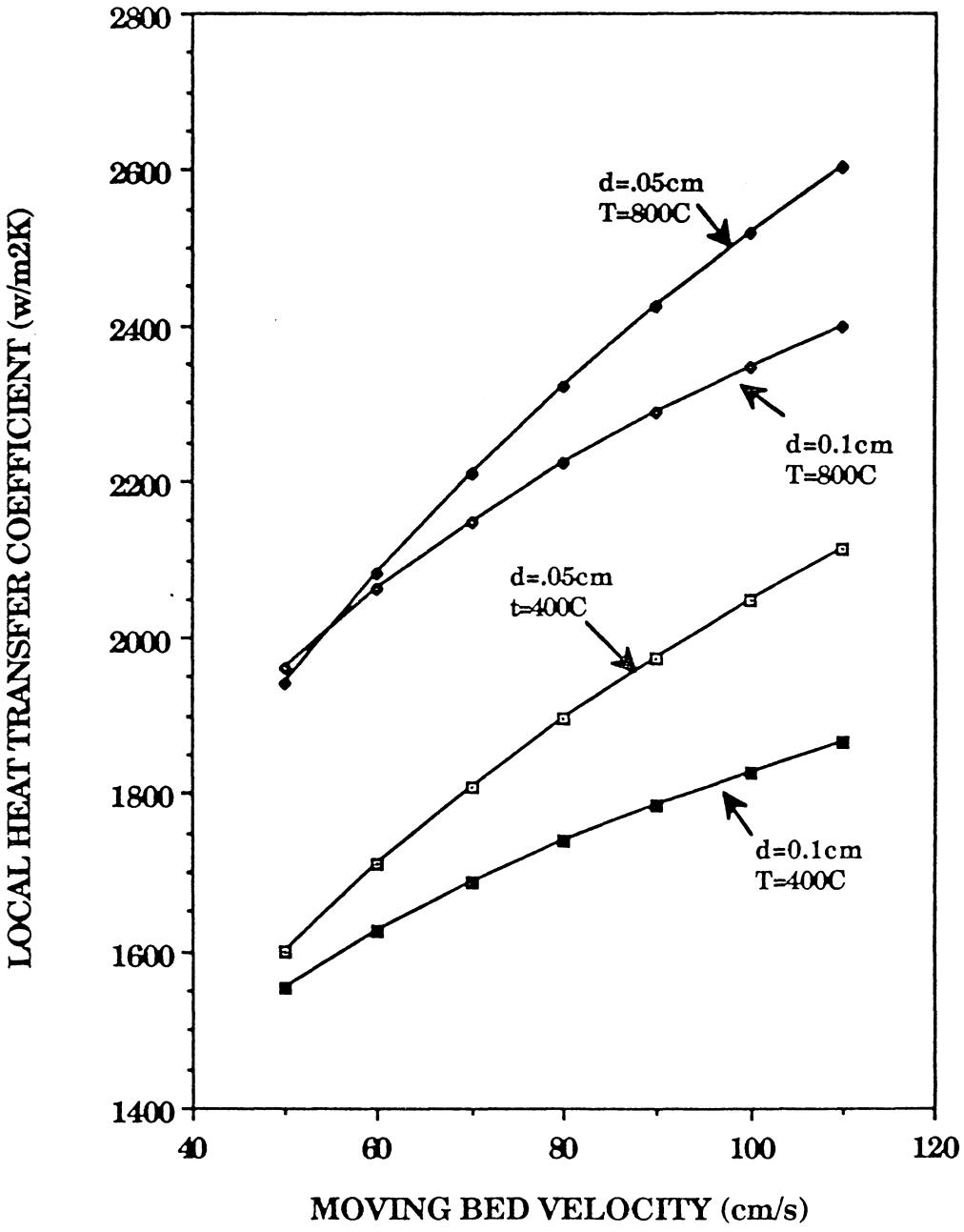

*L is the max. distance a particle stays in contact with the heated surface

Fig. 3.34. Local heat transfer coefficients as a function of velocity for sand particles using the Sullivan and Sabersky formulation for L=1 cm.

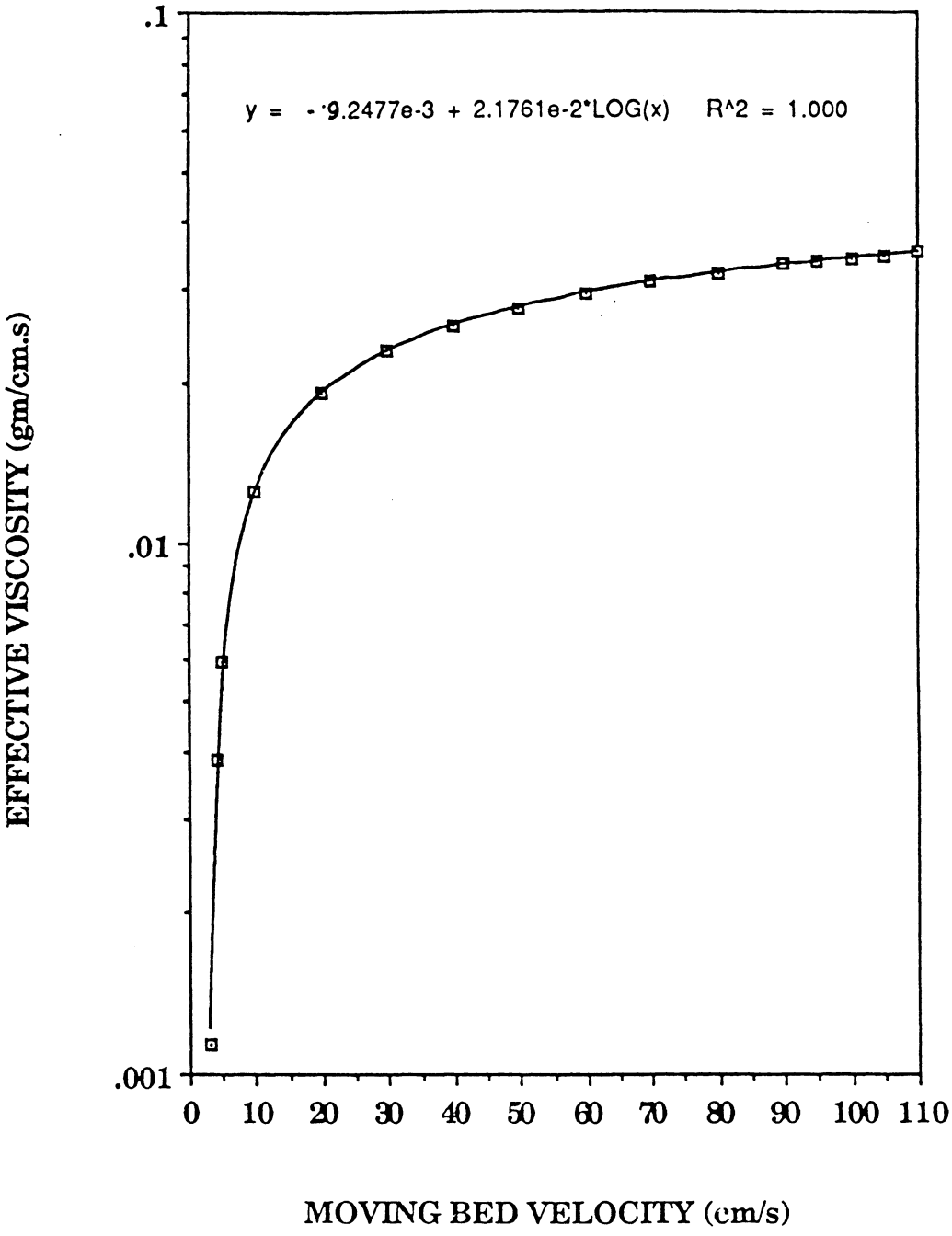

Fig. 3.35. Effective viscosity as a function of velocity for 500 μm soda lime glass particles.

To obtain the effective thermal conductivity of the moving bed, we made use of the method of Deissler and Boegli.[3.27] Figure 3.36 gives the static effective thermal conductivity for two phase systems as derived by Deissler and Boegli for materials separated by planes parallel to heat flow and perpendicular to heat flow. The thermal conductivity of Li_2O (90% density factor) was obtained using the expression given in Section 3.2.3.2. Thermal conductivity of He gas at 0.2 MPa is also well known.[3.28] The effective thermal conductivity for a bed with 40% He gas at 0.2 MPa is plotted in Fig. 3.37 as a function of temperature.

Figure 3.38 gives the specific heat for Li_2O as a function of temperature as obtained from the expression given in Section 3.2.3.2.

The Dittus-Boelter correlation is then used to determine the effective Nusselt number and hence the heat transfer coefficient in the different blanket zones. At the FW at midplane, this coefficient is 2758 W/m^2K, a value which is within 4% of that shown in Fig. 3.34 from the Sullivan and Sabersky formulation for L = 1.0 cm. In calculating FW temperatures a thermal conductivity for the 4D weave C/C composite of 70 W/mK has been used. There is still a lot unknown on how the thermal conductivity of C/C composites degrades as a result of radiation damage. In general for most graphites, the conductivity decreases to about 25% of its unirradiated value at high dose for an irradiation temperature of 500°C, and to 50% at 1200°C.[3.29] It was mentioned in Section 3.2.3.2 that C/C composites have been fabricated with conductivities up to 100 W/mK in a direction perpendicular to the fibers in 3D weaves. Parallel to the fibers it is as high as 500 W/mK. Since 4D weaves have a lot of fibers oriented parallel to the heat flow, we have assumed an initial conductivity of 140 W/mK, which degrades to 70 W/mK after irradiation. This is justified since the FW at midplane will have an average temperature of ~1300°C.

Table 3.10 gives the thermal hydraulics parameters for the SOMBRERO chamber. The temperature at the FW peaks at Z = -4.6 m where the surface heat load is equal to that at midplane and the Li_2O temperature is higher than at midplane. At Z = -4.6 m the FW internal surface temperature is 1242°C and the outside surface temperature is 1438°C.

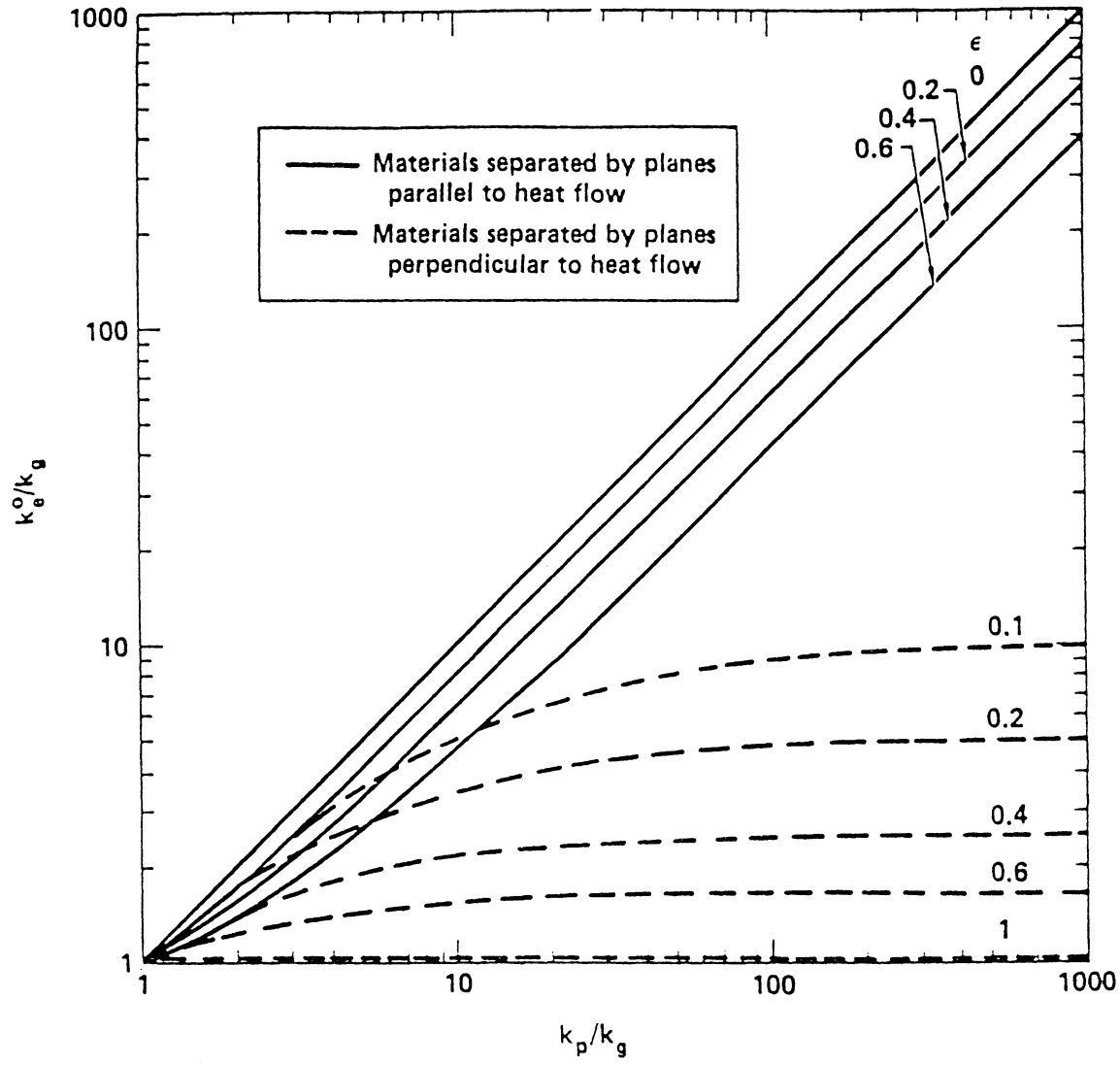

Fig. 3.36. Effective thermal conductivity for two phase system according to Deissler and Boegli.

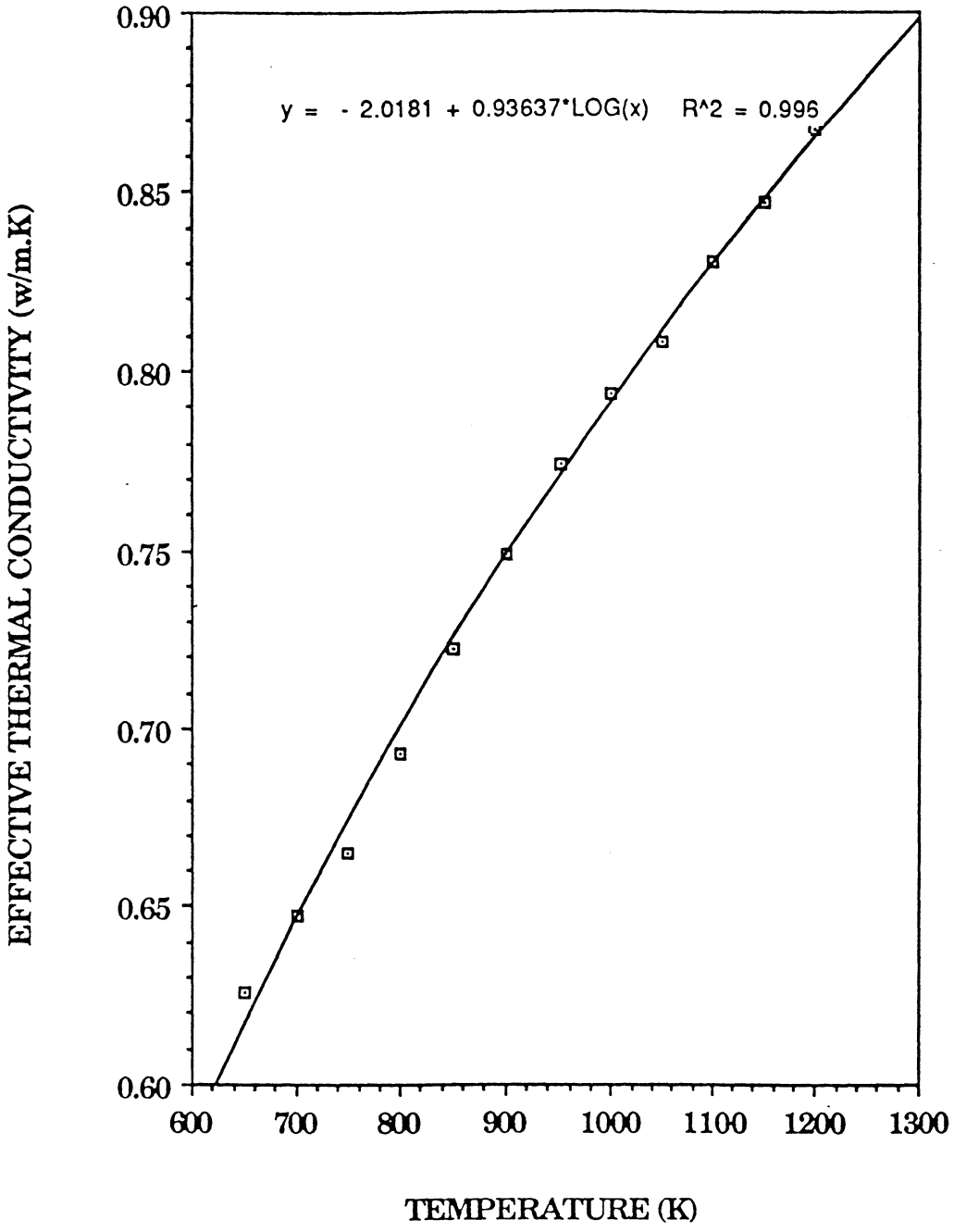

Fig. 3.37. Effective thermal conductivity of Li_2O (90% density) and 40% He gas at 0.2 MPa as a function of temperature.

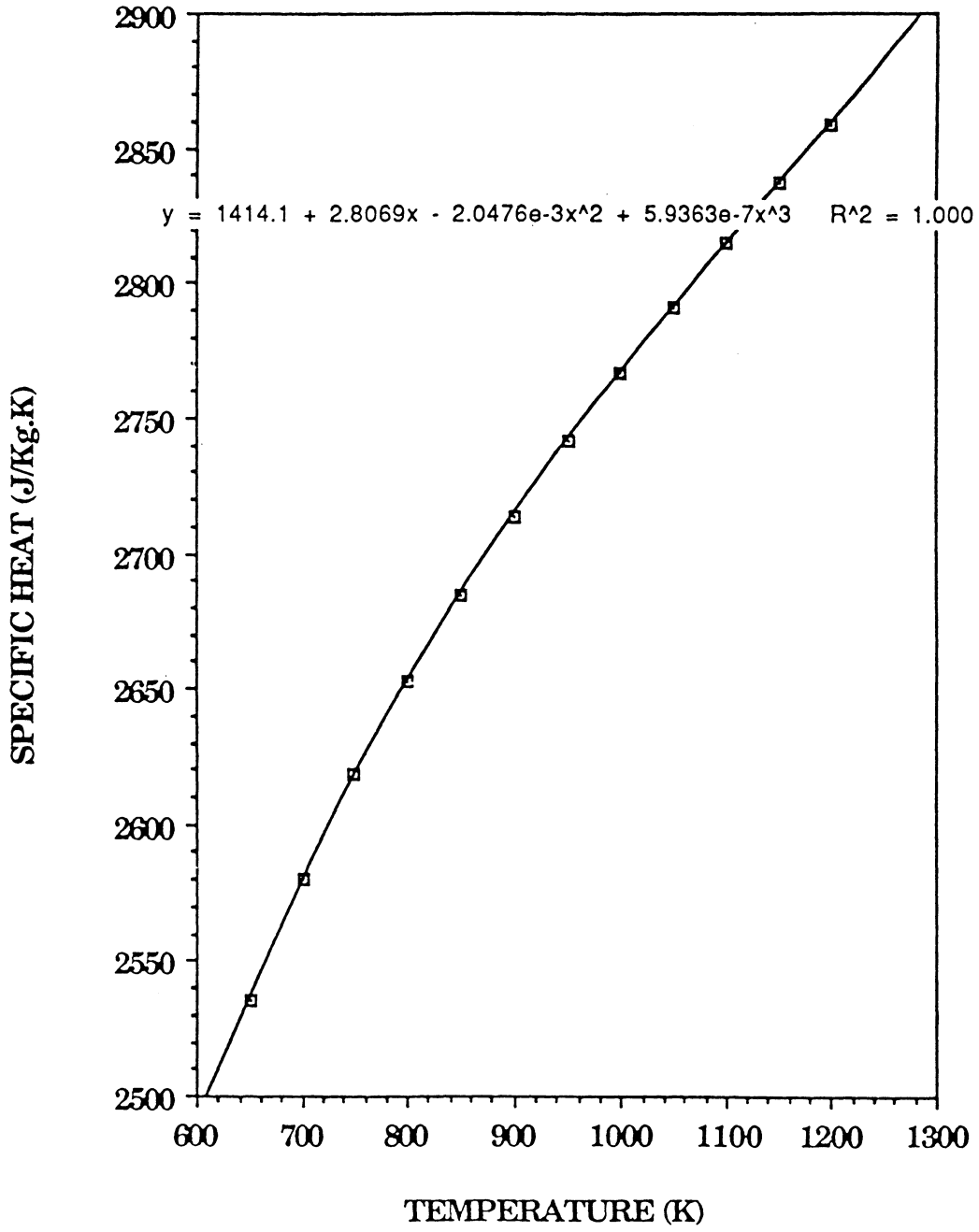

Fig. 3.38. Specific heat of Li_2O as a function of temperature.

Table 3.10. Thermal Hydraulics Parameters

Fusion Power (MW)	2677
Thermal Power (MW)	2891
Surface Power (MW)	801
Maximum Surface Heat Load (W/cm^2)	150.4
Maximum Nuclear Heat in FW (W/cm^3)	10.5
Inlet Li_2O Temperature (°C)	550
Outlet Temperature at FW (°C)	700
Outlet Temperature in Rear (°C)	800
Equilibrated Outlet Temperature (°C)	743
Li_2O Mass Flow Rate in 1st Channel (kg/s)	3129
Total Mass Flow Rate in Reactor (kg/s)	5491
Heat Transfer Coefficient at Midplane (W/m^2k)	2758
Inside FW Surface Temperature at Midplane (°C)	1149
Outside FW Surface Temperature at Midplane (°C)	1334
Heat Transfer Coefficient at Z = -4.6 (W/m^2k)	2573
Peak Inside FW Surface Temperature at Z = -4.6 m (°C)	1225
Peak Outside FW Surface Temperature at Z = -4.6 m (°C)	1438

The radial FW supports which are spaced every 21.3 cm act as fins and will reduce the FW temperature at the point where they are attached to it. Thermal conduction parallel to the fibers has been measured as high as 500 W/m^2K. If 50% of the conductivity is lost to radiation damage, then the remaining conductivity will still be very high at 250 W/mK. Figure 3.39 shows the model used and Fig. 3.40 the effect of the radial support on the peak FW temperature at Z = -4.6 m as modeled with a finite element code. Finally, Fig. 3.41 shows the temperature profiles at the FW on the inside and outside surfaces midway between radial supports as a function of the distance along the Z axis.

One of the concerns for the FW is in the event of a target misfire (i.e., the target does not get to the center of the chamber but the lasers fire because of a failure in the detection system). In this case the laser beams continue to the other side of the chamber and are incident on the FW. The worst case is close to the midplane where the beam diameter at the FW is ~18 cm. The laser energy per beam is 56.7 kJ, thus, the surface energy density is 222 J/cm^2. The latent heat of vaporization for graphite is 716 kJ/mole or 59.7 kJ/g. If we assume that all the energy goes into vaporizing the graphite, the amount vaporized is 3.7×10^{-3} g/cm^2. At a density of 1.8 g/cm^3, this amounts to ~20 μm. In the actual case there will be considerable vapor shielding, and the total deposited energy will be much less. For this reason, it is felt that a missed target does not present a serious problem for the FW.

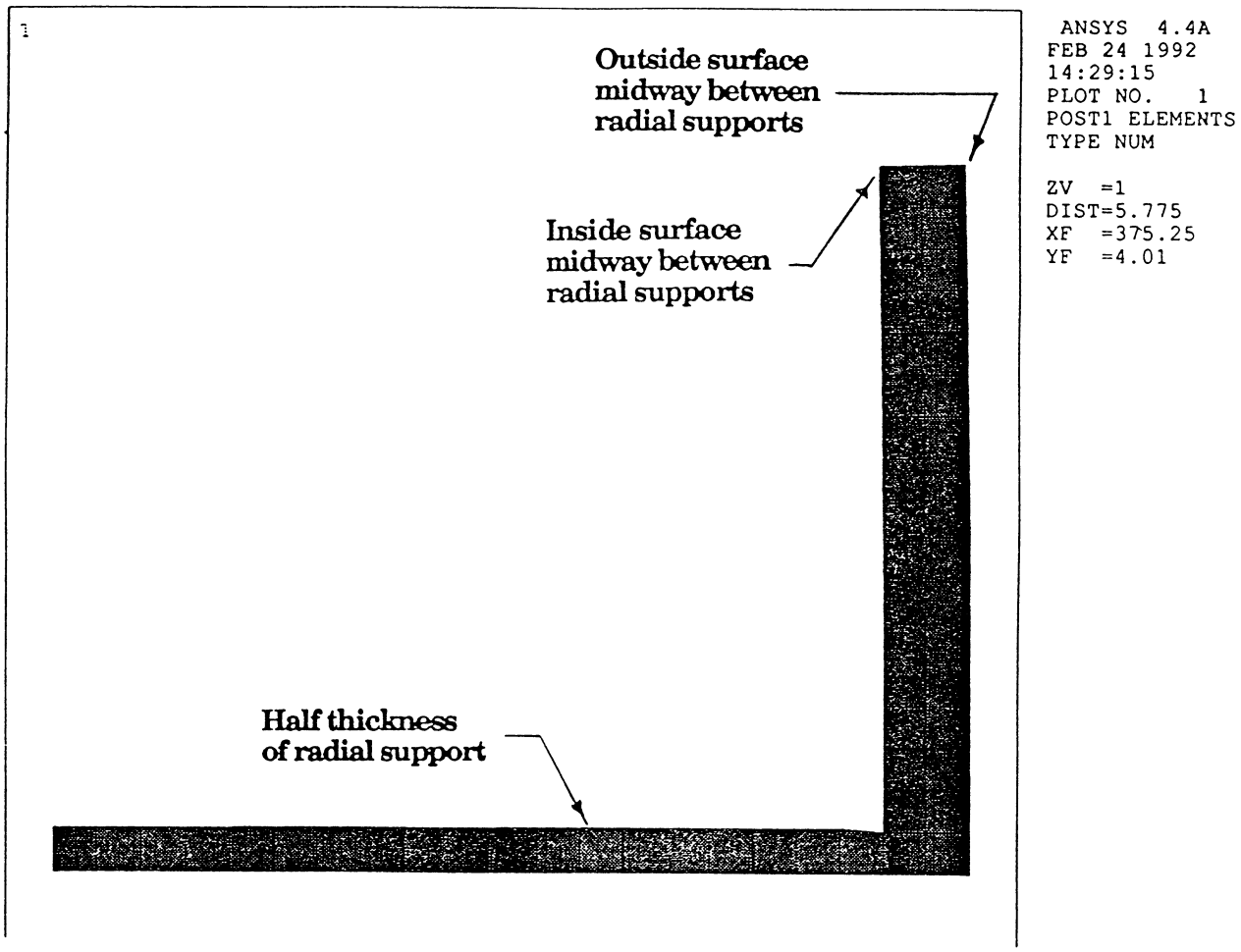

Fig. 3.39. Finite element model for determining the effect of the radial support on the FW temperature.

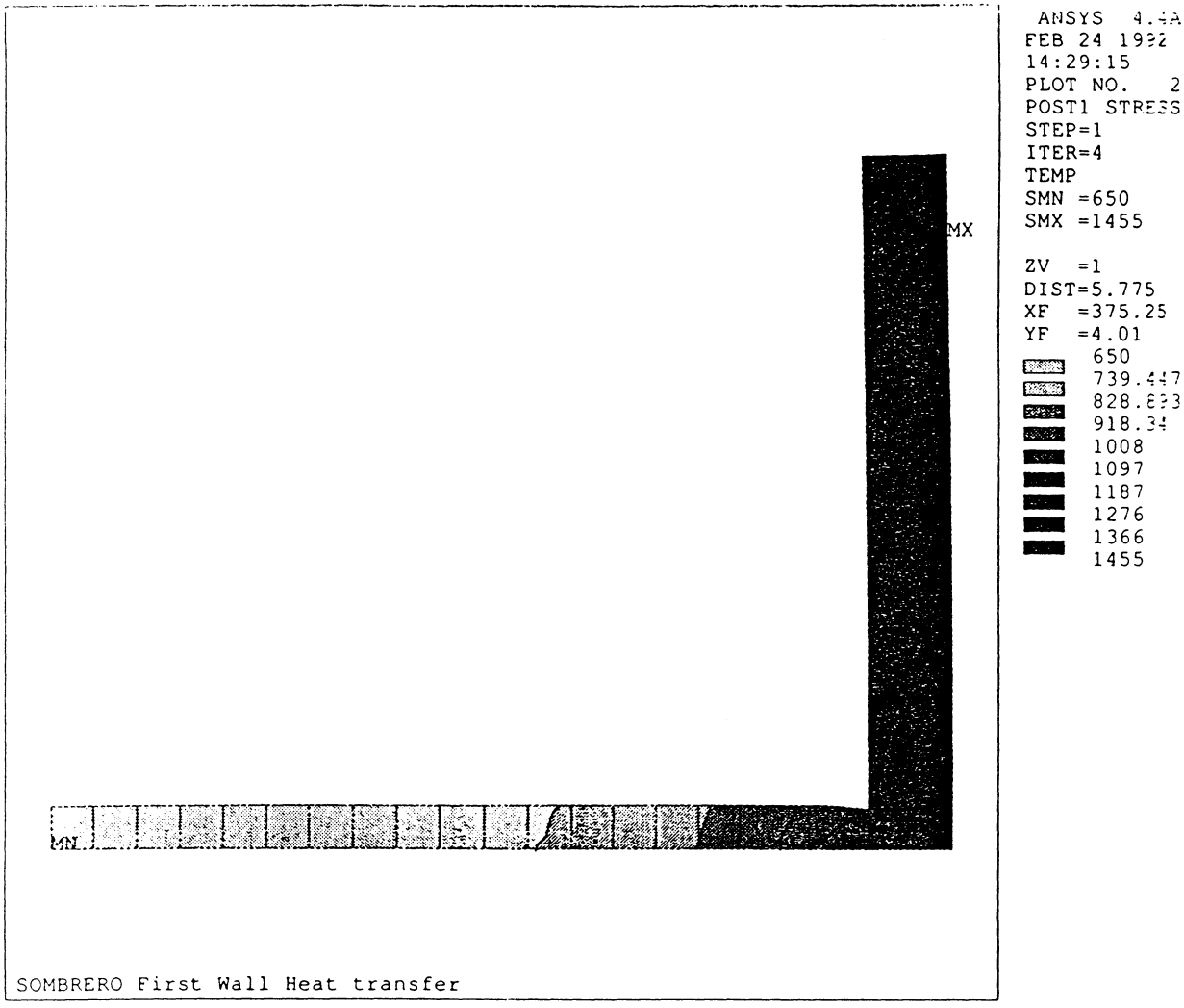

Fig. 3.40. Temperature variation at Z = -4.6 m as a result of the radial support.

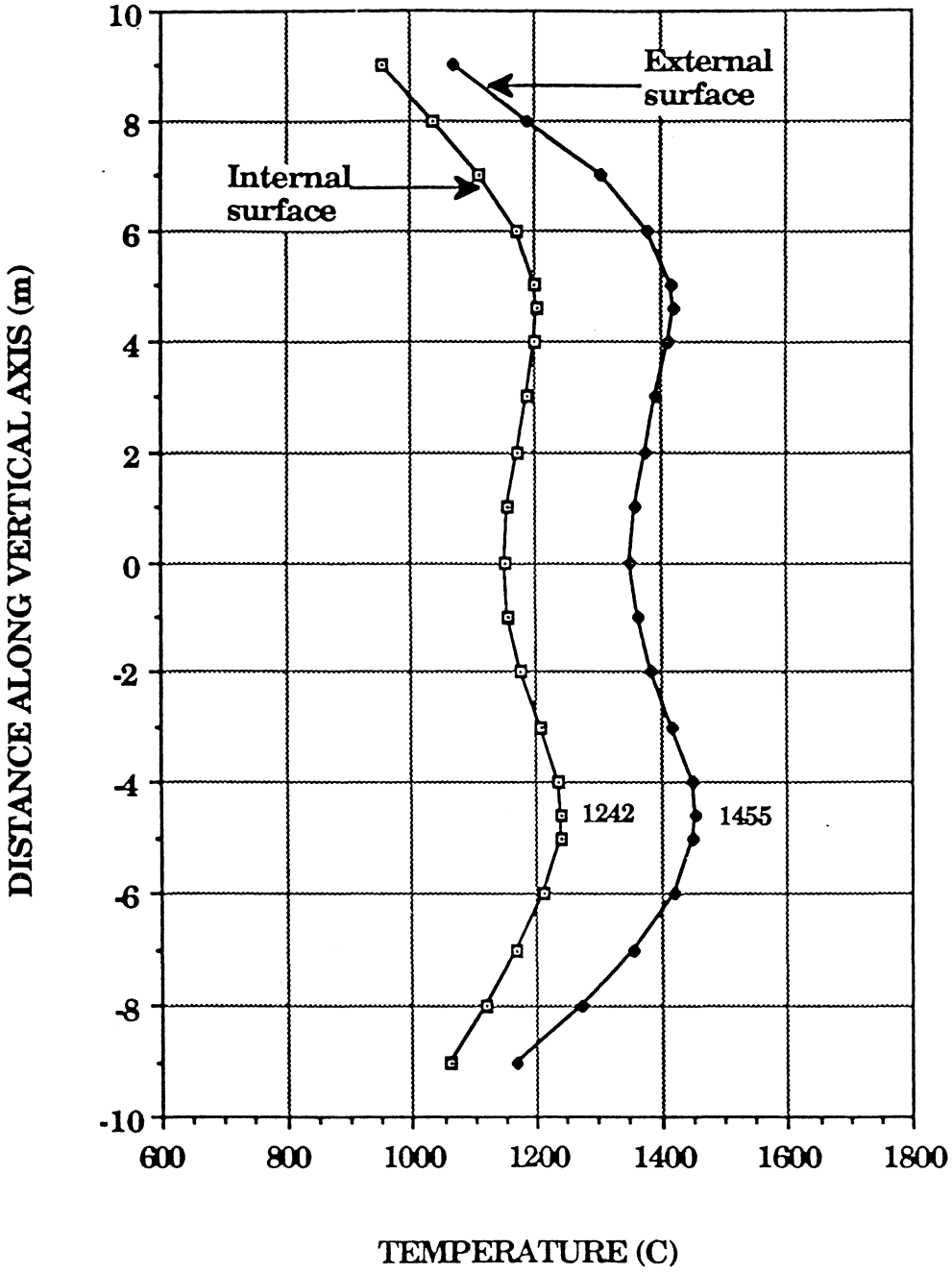

Fig. 3.41. Temperature profile on the inside and outside surfaces of the FW as a function of distance along the Z axis.

3.2.3.4 Chamber Support and Module Changeout

Figure 3.42 shows the chamber supported on the inner shield wall. There are 12 modules in the chamber and each module will have one support cantilevered from the shield wall. These modules have dedicated breeder material supply and return tubes. The supports are pivoted at the wall such that they can be retracted during module changeout.

This somewhat unique support and feed scheme was motivated by the desire to be able to remove a single module of the chamber due to a premature failure. Should any one module develop a problem, such as an excessive He leak, it would be possible to replace it with a new module without dismantling the whole chamber.

Figure 3.43 shows a schematic view of a chamber support. The side view indicates the arc the support executes during retraction. The top view shows that each support has a sector of a ring (1/12 of a circumference) attached to it. When all 12 supports are lowered into position, the sectors form a ring on which the chamber is supported. This scheme eliminates the bending moment on the cantilevered supports and puts the ring and the supports into compression. It also eliminates any concentrated loads on the chamber structure. The mass of the chamber is evenly distributed on the ring sectors.

Section 6.5 discusses the maintenance of the SOMBRERO chamber in detail. Briefly, to remove a module from the chamber, the following operations are needed:

- Li_2O breeder material drained from the reactor and supply/return manifolds.
- Supply and return tubes disconnected and removed.
- Tensioning bands at the upper and lower chamber extremities are released and removed.
- The polar crane attaches to the module in question and lifts it up ~0.5 m.
- The support retracts.
- A cage is lowered to the level of the module and the module is inserted into it and secured.
- The cage and module are lowered down into the pit below the chamber and laid down onto a polar carriage.
- The polar carriage then takes the module into a hot cell.

The procedure is reversed when a new module is replaced and inserted into the chamber.

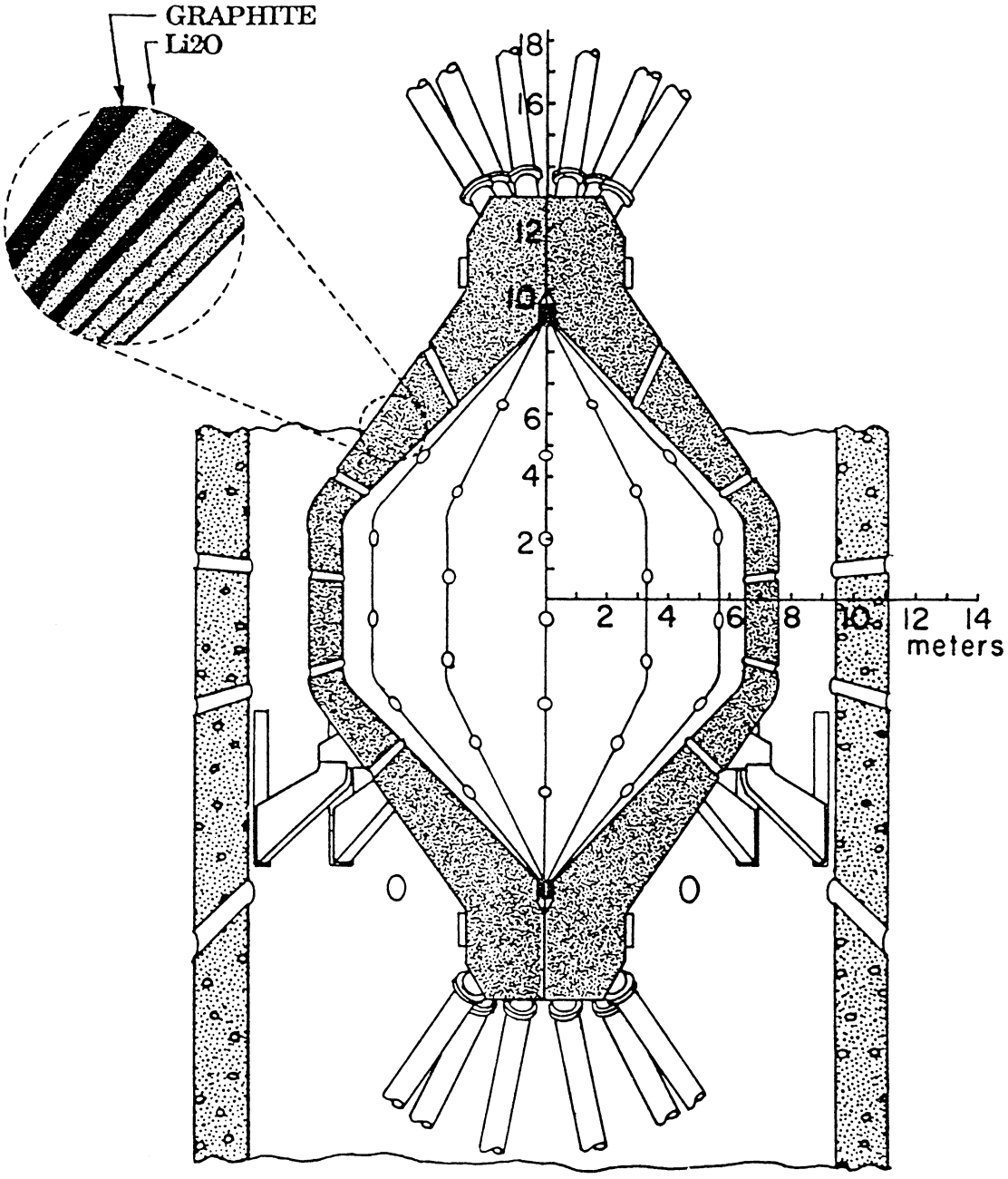

Fig. 3.42. Side view of the SOMBRERO chamber.

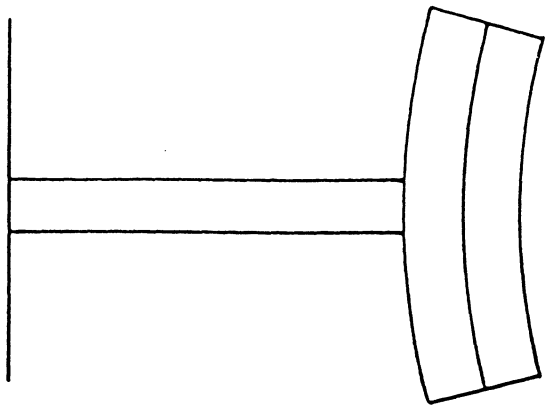

TOP VIEW

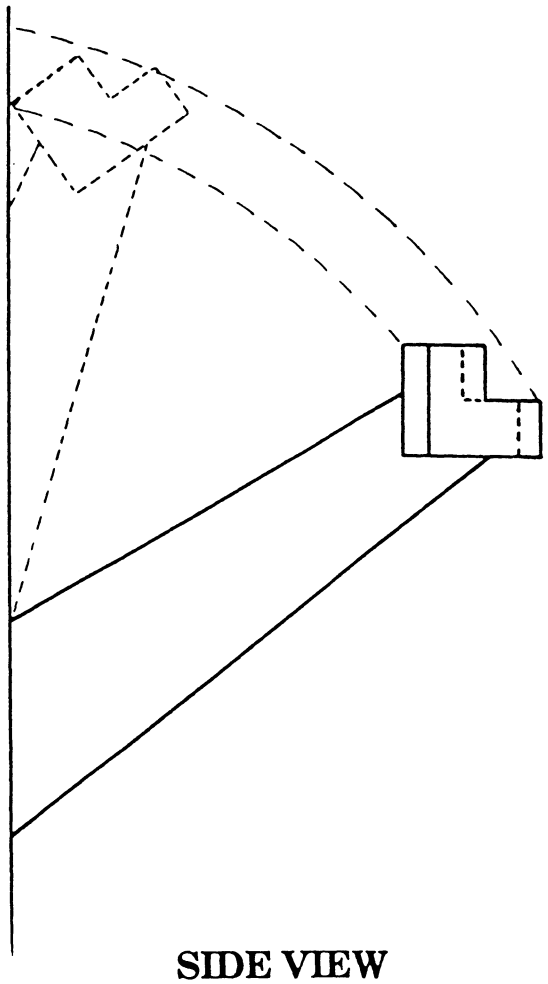

SIDE VIEW

Fig. 3.43. Schematic view of a chamber support.

3.2.4 Chamber Vacuum System

3.2.4.1 Vacuum Requirements

The atmosphere in the chamber is 0.5 torr of Xe gas. Since the beam ports in the chamber are open onto the reactor building, the atmosphere in the reactor building must be the same. The vacuum system must perform the following functions:

- Initial evacuation from atmospheric pressure to 0.1 torr.
- After Xe is injected up to a pressure of 0.5 torr, the vacuum system must recirculate it at some predetermined rate.
- Steady state evacuation of fusion products (unburned D, T and generated He).
- Steady state evacuation of leaks from the chamber and into the building.

The internal volume of the reaction chamber is 1.37×10^6 l. For the present it is felt that one gas changeover per second is appropriate which means a pumping speed of 1.4×10^6 torr l/s.

The volume of the building is 900,000 m^3. The time needed to evacuate this volume with a constant pumping speed of 1.4×10^6 l/s is:

$$t = \frac{V}{S} \ln\left(\frac{P_1}{P_2}\right)$$

where

V = volume (liters),
S = pumping speed (liters/s),
P_1 = initial pressure (760 torr), and
P_2 = final pressure (0.1 torr).

This gives t = 5744 s or 1.6 hours, which is a very reasonable time considering the evacuated volume. The pumping speed of 1.4×10^6 l/s will not be degraded by pipe conductances, etc., since the pumps will be located in close proximity to the building.

3.2.4.2 Leak Tolerance

Qualitatively, the breakdown threshold for He is an order of magnitude higher than for Xe, and thus it would seem that if the He gas pressure in the chamber was equivalent to that of Xe (0.5 torr), this implies a He leak rate of 7×10^5 torr l/s. At an average pressure of one atmosphere (average between 2 atm and 0.5 torr) this amounts to 921 l/s.

Leakage in the viscous flow regime where pd > 0.55 torr-cm the conductance of a hole is given by:

$$C = \frac{1333\,\pi\,r^4\,p}{8000\,\eta\,l} \quad \text{liters/s}$$

where

r = hole radius,
p = average pressure,
d = hole diameter,
η = gas viscosity, and
l = length of hole.

For this equation to be valid d must be:

$$d > (0.55 \text{ torr-cm}) / (760 \text{ torr})$$

$$d > 7.2 \times 10^{-4} \text{ cm}$$

We can now calculate the size of the hole needed to produce a leak of 921 l/s:

$$r = \left[\frac{8000\,C\,\eta\,l}{1333\,\pi\,p}\right]^{1/4}$$

The viscosity of He gas at 760 torr and 1500 K is 615×10^{-6} g/cm·s and l, the FW thickness, is 1.0 cm. This gives an r = 0.19 cm or a hole of 0.38 cm diameter.

A more realistic way of looking at this problem is to see how many holes of smaller diameter can be tolerated. It is likely that there will be many small leaks rather than several large ones. Figure 3.44 shows the number of pin holes in the FW as a function of hole diameter. It can be seen that there can be 1.4×10^9 holes of 20 μm diameter to obtain this leak rate. On the other end, the number of 500 μm diameter holes is 3670.

There is very little information on the leak tightness of 3D and 4D weaves of C/C composites. We have assumed that the inside surface (Li_2O side) of the chamber channels will be coated with a thin coating of SiC for which there is some leak tightness information. It is postulated that the most likely leaks will be very small tortuous ones longer than the FW thickness. From the above analysis, it seems that this system is amenable to many such leaks.

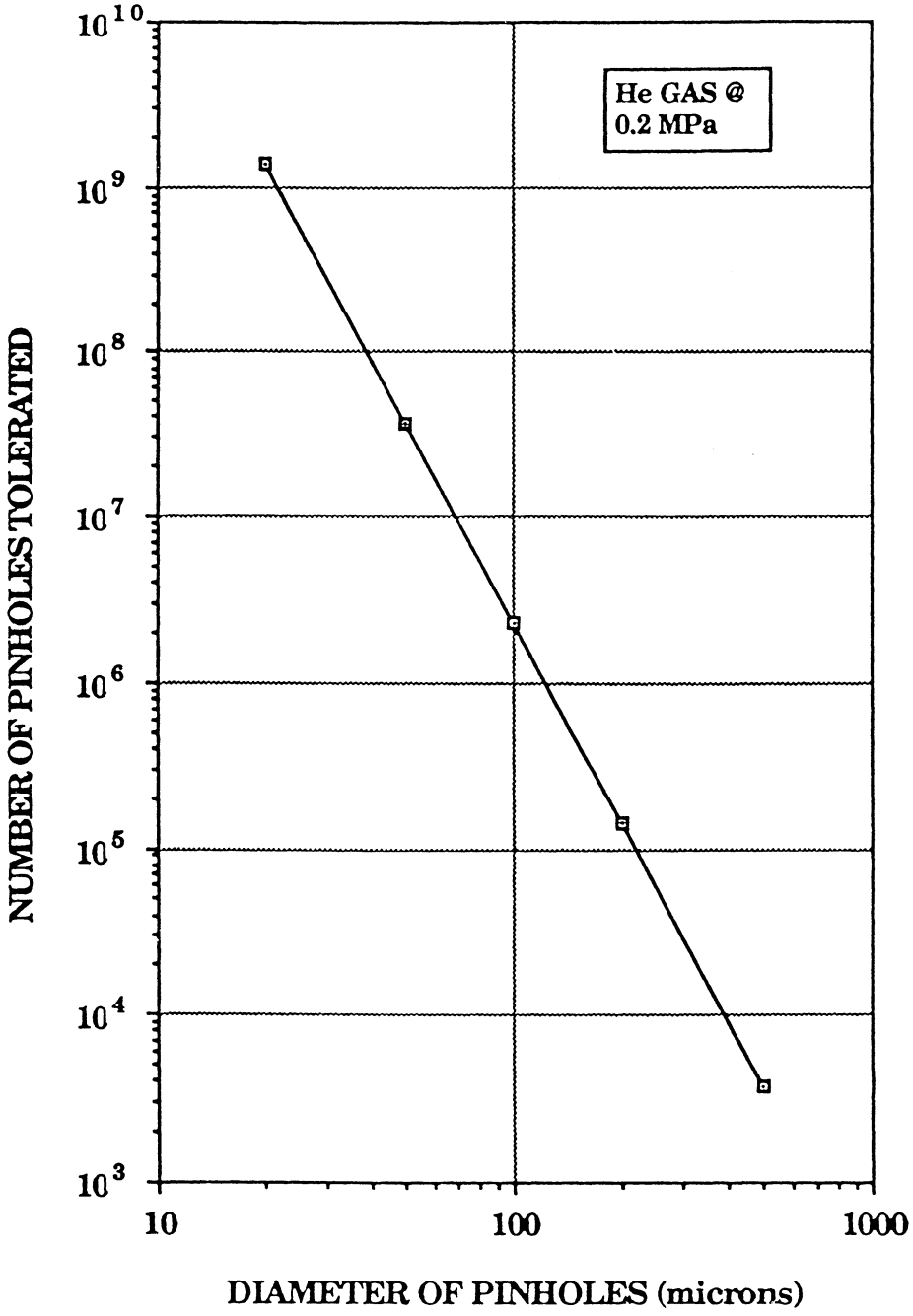

Fig. 3.44. Leak tolerance of SOMBRERO chamber - Number of pinholes tolerated as a function of pinhole diameter.

3.2.4.3 Vacuum System Design

The most appropriate pumps to operate in the 0.5 torr regime are Roots blowers. They comes in large capacity, are very rugged, dependable, and do not use oil for sealing. Instead they depend on well balanced rotors and definite clearances between the moving parts, such that operation at high rotational speeds are possible. Among the attributes of Roots blowers are:

- High Volumetric Efficiency
- High Pumping Speed Over Large Pressure Range
- Sturdy Construction, Small Size, Quiet Running
- Contact Free Rotation Of Interlocked Impellers
- Lubrication Free Pump Chamber
- Reliable Operation with Little Maintenance
- Easy oo Dismantle And Clean
- Low Operating Cost
- Unaffected by Contaminating Gases, Vapors, and Dust.

The recommended pressure rise for Roots blowers is 40 torr. Thus the primary Roots blowers' pressure will raise the effluent pressure from 0.5 torr to 40 torr and the secondary blowers to 80 torr. Dry sealed mechanical pumps will then deliver the effluents to Xe purification and hydrogen isotope recovery and separation system at near atmospheric pressure. Roots blowers with capacities of 10^4 l/s are currently available. It is not out of the question that pumps with capacities of 2 or 3×10^4 l/s will be available in which case, the number of primary blowers will be 46. These will be backed up by 10 secondary blowers. The estimated power consumption is 15 MW. Table 3.11 summarizes the vacuum system parameters.

Table 3.11. Vacuum System Parameters

Chamber Volume (l)	1.37×10^6
Reactor Building Volume (l)	9×10^8
Pressure of Xe in Chamber (Torr)	0.5
Estimated Pumping Speed (l/s)	1.4×10^6
Estimated Time to Evacuate Building (h)	1.6
Capacity of Roots Pumps (l/s)	3×10^4
Number of Primary Pumps	46
Number of Secondary Pumps	10
Power Consumption (MW)	15

3.2.5 Neutronics Analysis

3.2.5.1 Neutronics Model and Assumptions

The main objective of the neutronics analysis is to optimize the blanket design to insure tritium self-sufficiency while maximizing the overall reactor energy multiplication. The solid angle fraction subtended by the 60 beam ports in the SOMBRERO chamber is only 0.25% resulting in negligible loss of breeding. Hence, overall tritium self-sufficiency can be achieved with a modest local (1-D) tritium breeding ratio (TBR). This attractive feature of inertial confinement reactors allows for a simple blanket design in which no special neutron multipliers are needed. The local TBR for SOMBRERO is required to be at least 1.15 to achieve overall tritium self-sufficiency taking into account radioactive decay, loss between production and use, and maintaining the equilibrium tritium inventory in the different reactor components. In order to enhance the safety and environmental features of the design, low activation materials are used. Carbon/carbon composite structure and Li_2O breeder are used in the SOMBRERO blanket. The 1-cm-thick bare chamber structural wall has a minimum distance of 6.5 m from the target and is protected from the target x rays and debris by a 0.5 torr of Xe gas. In this section, the neutron-induced damage in the blanket structure is calculated to determine the achievable lifetime. The lifetime of the final optics is also determined. In addition, an objective of this neutronics analysis is to provide adequate biological shielding to maintain an acceptable operational biological dose rate <2.5 mrem/hr everywhere outside the reactor building.

Neutronics calculations for SOMBRERO have been performed using one-dimensional spherical geometry. The discrete ordinates code ONEDANT[3.30] was utilized along with 30 neutron - 12 gamma group cross section data based on the ENDF/B-V evaluation. A point isotropic source is used at the center of the chamber emitting neutrons and gamma photons. The target spectrum takes into account neutron multiplication, spectrum softening, and gamma generation resulting from the interaction of the fusion neutrons with the dense target material. One-dimensional spherical geometry neutronics calculations have been performed for a generic single shell target configuration at ignition.[3.31] The DT core is compressed to 485 times its solid density to a ρR-value of 2 g/cm^2 resulting in significant neutron target interactions. A uniform 14.1 MeV neutron source was used in the compressed DT fuel zone. For each DT fusion reaction, 1.025 neutrons are emitted from the target with an average energy of 11.64 MeV. In addition, 0.013 gamma photons are emitted with 3.85 MeV average energy. The energy spectra of neutrons and gamma photons emitted from the target are shown in Fig. 3.45. 2.1% of the fusion energy is lost in endoergic reactions in the target, and 69.5% of the target yield is carried by neutrons and gamma photons, which interact with the blanket material resulting in tritium breeding, nuclear heating, and radiation damage. The rest of the target yield is carried by x rays and debris which deposit their

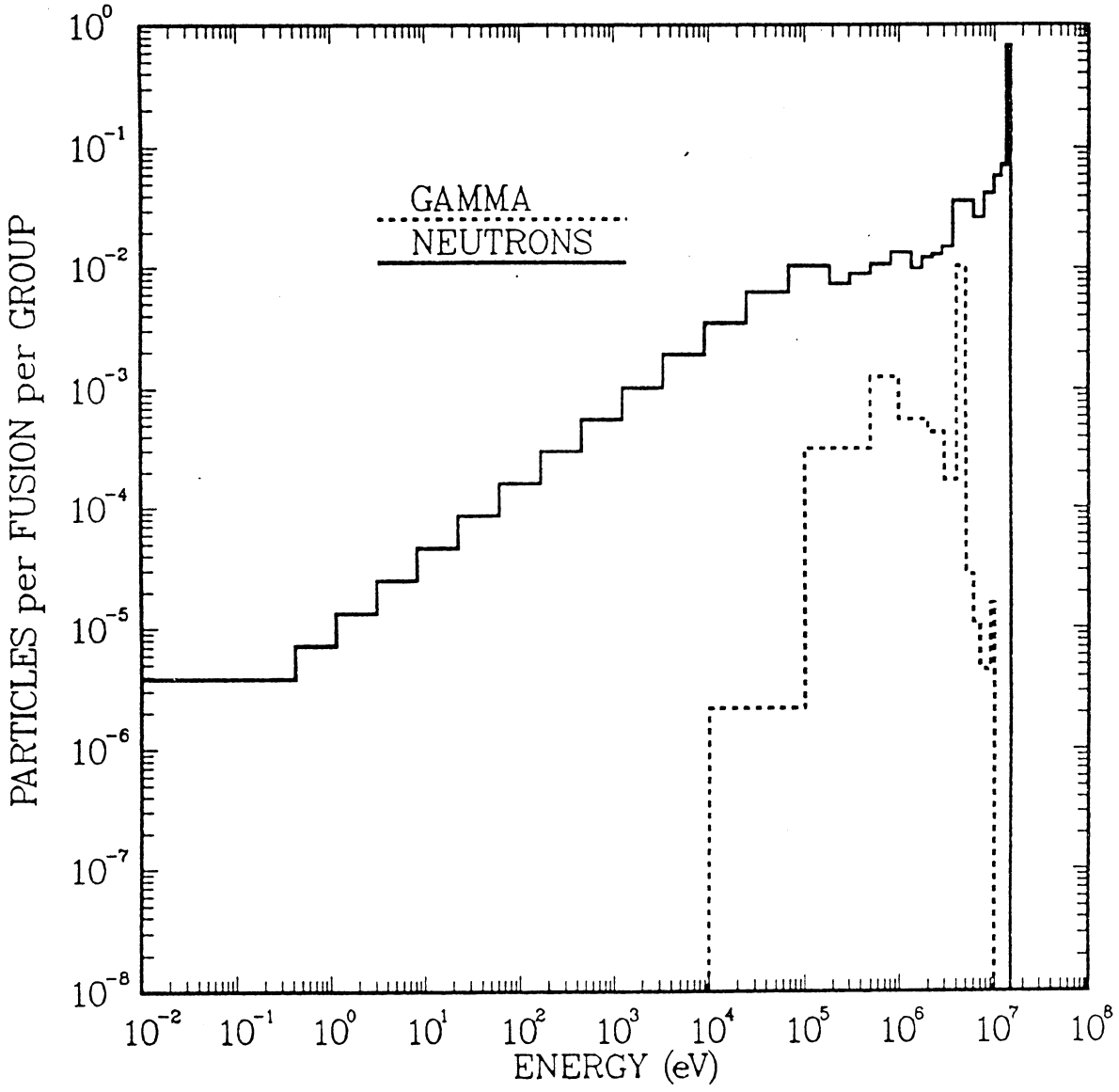

Fig. 3.45. Energy spectra of neutrons and gamma photons emitted from the target.

energy at the front surface of the blanket. The blanket nuclear energy multiplication (M_n) is defined as the ratio of the total blanket nuclear heating resulting from neutron and gamma interactions to the energy carried by the direct neutrons and gamma photons incident on the first wall. This quantity is a measure of the energy multiplication capability of the blanket and is to be compared with the energy multiplication factor commonly used in magnetic confinement designs. To take into account the surface energy deposited by x rays and ion debris and the energy lost in target endoergic reactions, an overall energy multiplication factor (M_o) can be defined for IFE reactors. M_o, which depends on the target design, is the ratio of total thermal power deposited in the target and blanket to the DT fusion power. For the target design used here, M_o is related to M_n via

$$M_o = 0.979\ [0.695\ M_n + 0.305]\ .$$

The results presented here are normalized to a target DT fuel yield of ~400 MJ and a repetition rate of 6.7 Hz.

3.2.5.2 Blanket Parametric Analysis

Several neutronics calculations have been performed to investigate the impact of the different design parameters on the nuclear performance of the blanket. In these calculations, the lithium enrichment, blanket thickness, and structure content have been varied. In addition, the impact of using a metallic reflector was assessed. The nuclear performance parameters considered in this analysis are the tritium breeding ratio (TBR) and the overall energy multiplication (M_o). In the calculations, a 1-cm-thick carbon/carbon first wall is located at 6.5 m from the target. Li_2O solid breeder moving bed is used in the blanket at a packing fraction of 0.6. The density of the Li_2O used to be 90% of the theoretical density. In the preliminary analysis, the carbon/carbon (C/C) composite structural material is considered to occupy 5% of the blanket volume. The option of using a 0.5 m thick metallic reflector consisting of 90% low activation ferritic steel and 10% He coolant was investigated. A concrete biological shield was used behind the reflector in the neutronics model.

The effect of lithium enrichment on TBR and M_o is shown in Fig. 3.46 for a 0.5 m thick blanket without a metallic reflector. The TBR increases slightly as lithium is enriched from 7.4 (natural) to 10% ^6Li. Increasing the enrichment beyond 10% reduces the TBR significantly. The peak TBR value is only 0.4% larger than the value achieved with natural lithium. In addition, enriching the lithium results in a small (<3%) enhancement in M_o. Based on these results, natural lithium is used in the Li_2O breeder. The effects of blanket thickness on TBR and M_o are shown in Figs. 3.47 and 3.48 for both cases with and without a metallic reflector. Using a metallic reflector increases the TBR by only 1.3% and M_o by 3.5% for a 0.7 m thick blanket. Since the

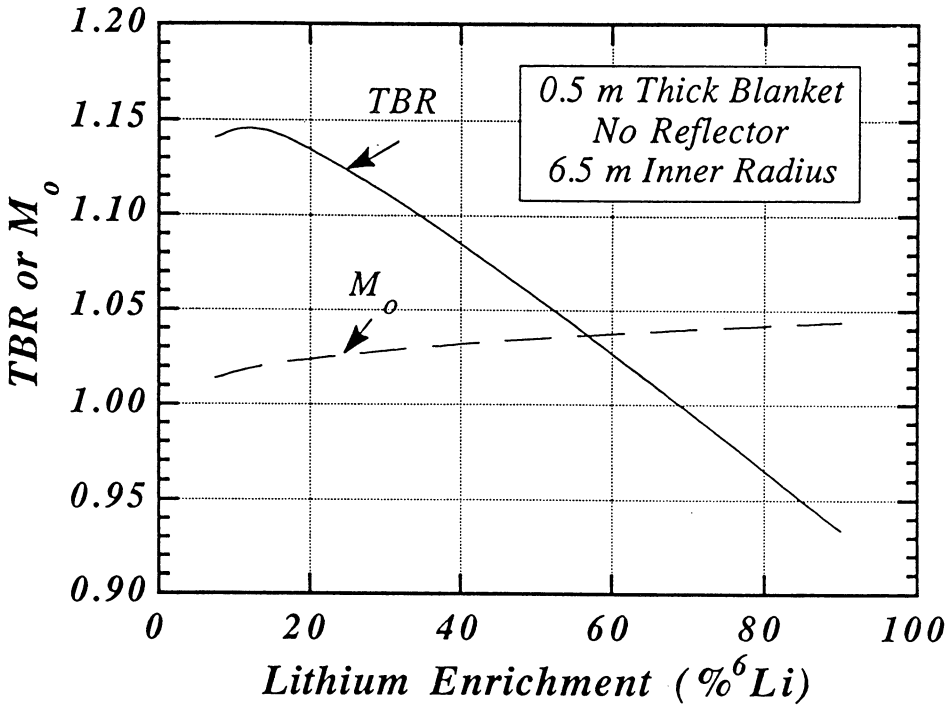

Fig. 3.46. Effect of lithium enrichment on TBR and M_o.

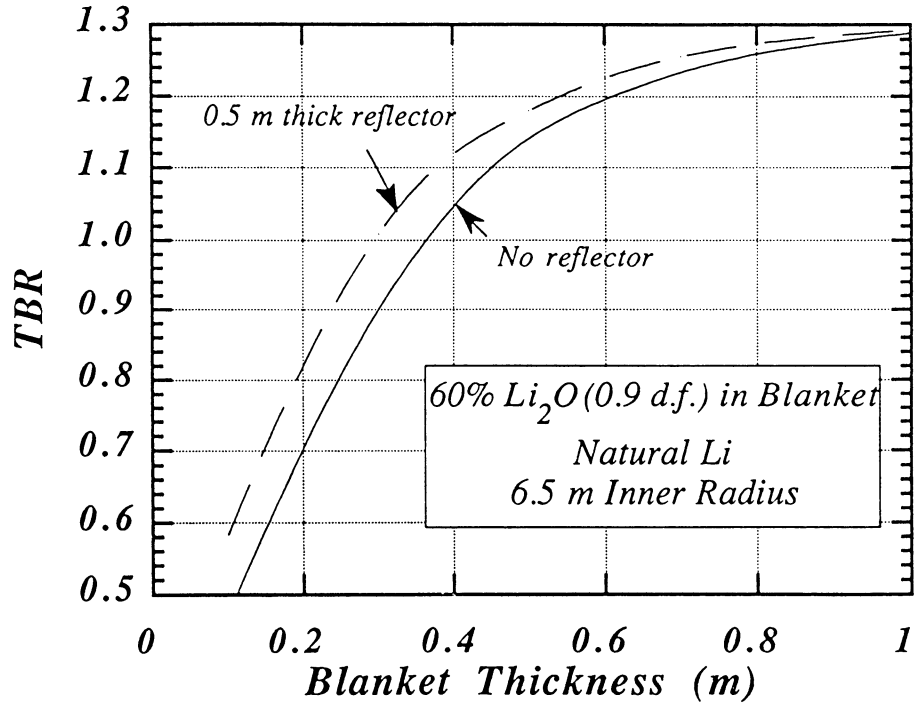

Fig. 3.47. Effect of blanket thickness on TBR.

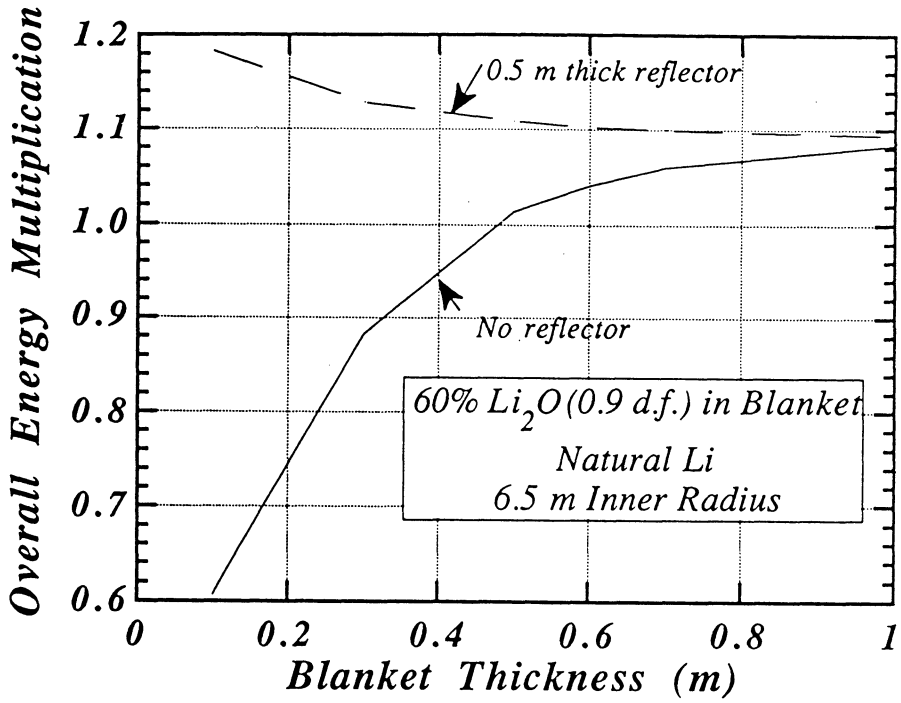

Fig. 3.48. Effect of blanket thickness on M_o.

enhancement of TBR and M_o is not significant, it was decided not to use a metallic reflector to avoid design complexity and steel activation. The TBR and M_o values achieved for a 0.7 m thick blanket without a reflector are 1.24 and 1.062, respectively. It should be noted that the preliminary parametric analysis given above overestimates the TBR and M_o values since the concrete shield is placed right behind the blanket. In the reference building layout, the concrete shield has an inner radius of 10 m. Hence neutron leakage at the back of the blanket will be excessive reducing neutron utilization in the blanket. The number of neutrons leaking from the back of the 0.7 m thick blanket is 0.124 per DT fusion in the target. This results in decreasing the TBR and M_o values to 1.174 and 1.039, respectively.

In order to increase neutron utilization in the blanket, the use of a carbon reflector is considered. Table 3.12 lists the nuclear performance parameters for different design options utilizing a carbon reflector. In option 1, no reflector is used and the carbon structure content is 5% in the blanket. In option 2, a 0.5 m thick carbon reflector with 10% He coolant is used behind the 0.7 m thick blanket. The TBR and M_o values increased to 1.275 and 1.069, respectively. Notice that nuclear heating in the reflector amounts to only 2% of the total nuclear heating and is not included in the calculated energy multiplication. In option 3, 4, and 5, instead of using a separate carbon reflector, a relatively thicker blanket is used with the volumetric content of the carbon structure varying increasing towards the back. The blanket is divided into three zones with

different structure contents. In these options, the total blanket and reflector thickness is reduced compared to the case with a separate shield. The values for neutron leakage at the back of the blanket are 0.017, 0.016, and 0.009 neutrons per fusion in options 3, 4, and 5, respectively, compared to 0.124 without a reflector. Comparing the results for options 3, 4 and 5, it is clear that TBR and M_0 are not sensitive to the thickness and structure content of the back layer of blanket. Therefore, design option 3 is chosen for the reference SOMBRERO blanket design.

Table 3.12. Nuclear Performance for the Different Design Options.

Option	Blanket * Thickness (m)	Zone Thickness (cm)	%C in Blanket	Reflector Thickness (m)	TBR	M_o
1	0.7	69	5	0	1.174	1.039
2	0.7	69	5	0.5	1.275	1.069
3	1.0	19/40/40	3/20/50	0	1.251	1.080
4	1.0	19/40/40	3/20/60	0	1.251	1.080
5	1.1	19/40/50	3/20/50	0	1.259	1.083

* Includes 1-cm-thick C/C first wall

3.2.5.3 Neutronics Parameters for the Reference Design

The radial build of the reference SOMBRERO blanket design is given in Fig. 3.49. A 1-m-thick blanket is used with increasing carbon content towards the back. The 1-D local TBR for the reference blanket is 1.25. The overall TBR value is expected to be close to the 1-D value since the solid angle fraction subtended by the 60 beam penetrations is less than 0.3%. The overall reactor energy multiplication is 1.08. For a DT fusion power of 2677 MW, the total thermal power is 2891 MW with ~800 MW deposited at the surface of the first wall by x rays and debris and 2100 MW deposited volumetrically in the blanket by neutrons and gamma photons. Figure 3.50 shows the radial variation of power density in the blanket. The peak first wall power density is 10.9 W/cm^3. The power density in the blanket varies from 12.6 W/cm^3 at the front to 0.1 W/cm^3 at the back.

Figure 3.51 gives the radial variation of damage rate in the carbon/carbon composite structural material used in the blanket. The peak dpa rate is 15.3 dpa/FPY, which occurs in the first wall at the reactor midplane. The dpa rate drops to 0.05 dpa/FPY at the back of the blanket. The peak helium production rate in the structure is 3770 He appm/FPY at the first wall. The main problem for the c/c composite is the dimensional stability after operating at high temperature in a neutron environment for long periods of time. During high temperature irradiation, the graphite

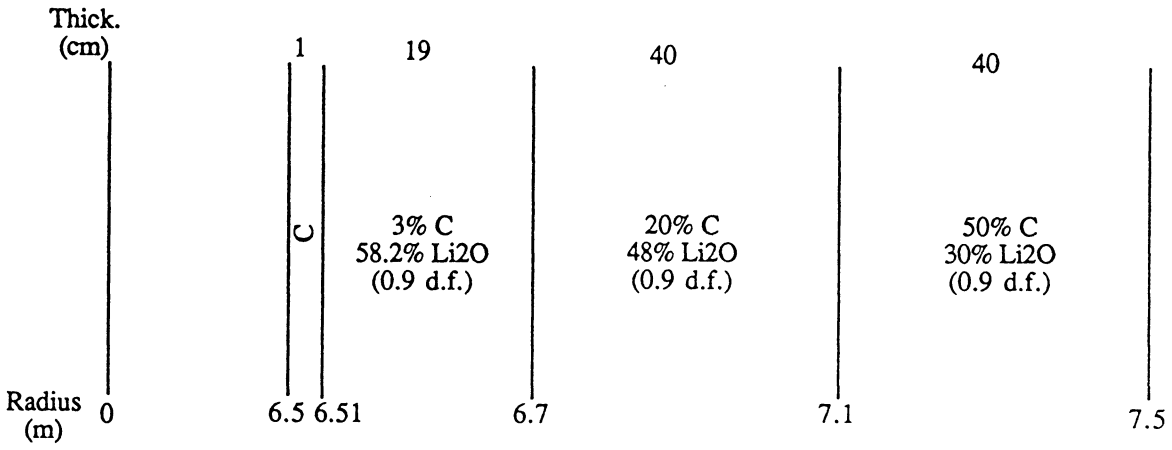

Fig. 3.49. Radial build of reference SOMBRERO blanket design.

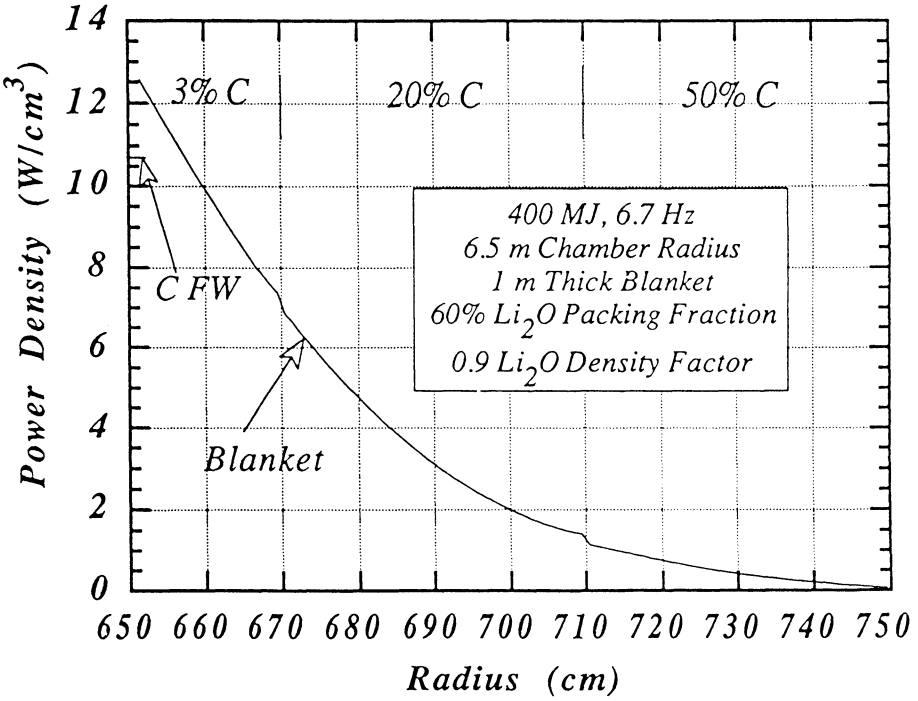

Fig. 3.50. Radial variation of power density in blanket.

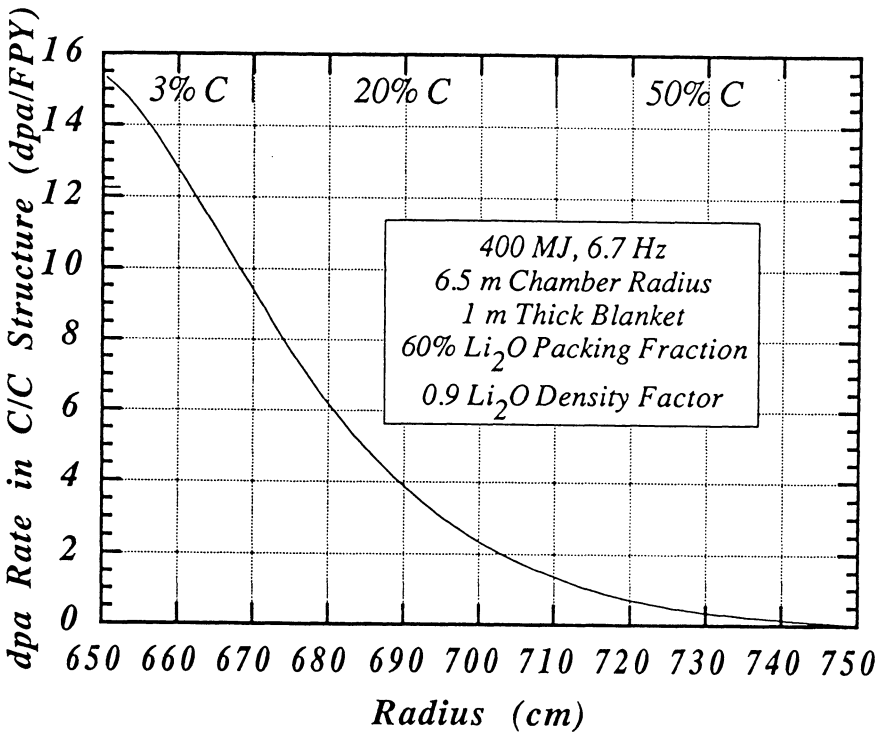

Fig. 3.51. Radial variation of structure damage rate in blanket.

first shrinks and then expands at a very rapid rate. A useful lifetime is usually determined when the dimensional change reverses and crosses the zero swelling line. Birch and Brocklehurst[3.32] reported data on three forms of graphite showing that AXZ-5Q1 graphite will reach the zero swelling point at a fluence of 35 dpa at 1300°C. The graphites tested thus far have not been optimized for the fusion environment. We assume that the dpa limit can be increased to 75 dpa by optimizing the graphite for a fusion neutron environment in a materials development program. With a dpa limit of 75 dpa, the C/C composite first wall is expected to have ~5 FPY lifetime.

3.2.5.4 Biological Shielding

The concrete biological shield thickness required to achieve an operational dose rate of 2.5 mrem/hr depends on the location of shield and material between target and shield. Several 1-D calculations have been performed to determine the required shield thickness. The shield is composed of 70% concrete, 20% steel, and 10% He coolant. It was found that 25 cm of the steel reinforced concrete shield will reduce the dose rate by an order of magnitude.

Figure 3.52 shows the effect of shield thickness on the biological dose rate during operation at the back of the shield. The inner surface of the shield is at a distance of 50 m from the target with no material used in the region between the target and the shield. This is representative of the areas of the reactor building exposed to the direct source neutrons streaming through the

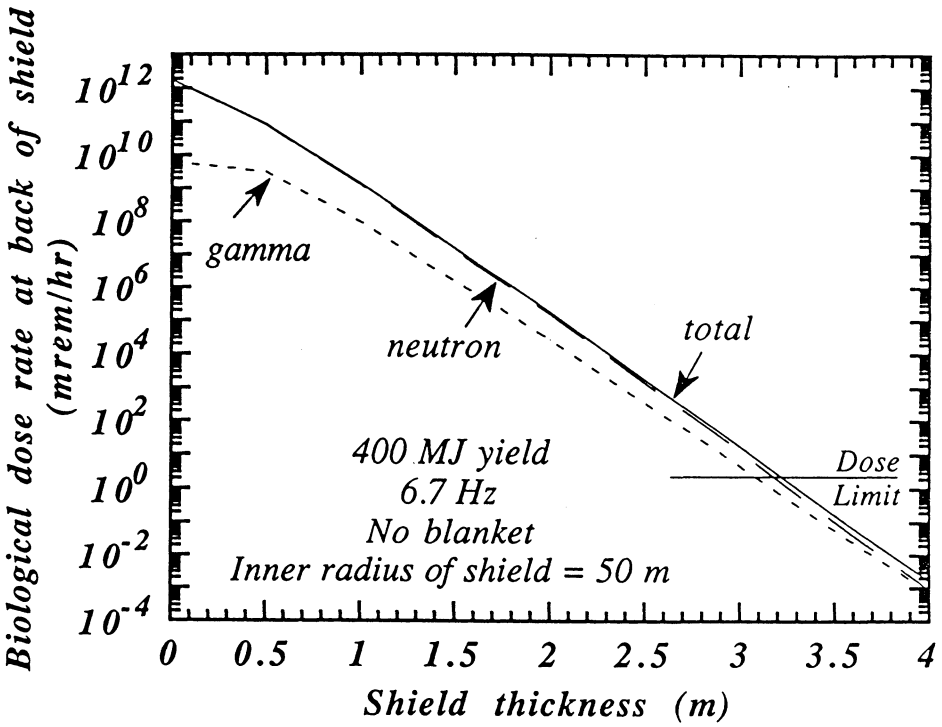

Fig. 3.52. Operational biological dose rate as a function of shield thickness without blanket.

beam ports. The results indicate that a wall thickness of 3.2 m is required in these zones located inside the direct neutron traps attached to the containment building. Figure 3.53 gives the effect of shield thickness on the operational dose rate for a concrete shield located at 10 m from the target with the 1-m-thick blanket included in the model. It is clear from the results that a total shield thickness of 2.7 m is required behind the blanket.

The chamber is surrounded by a cylindrical concrete shield with an inner radius of 10 cm. The IHX and steam generators are located in the space between this inner shield and the outer containment building. The thickness of the inner shield is determined such that hands-on-maintenance can be performed on these components following shutdown. The dose rate resulting from the decay gamma emitted from the activated material should not exceed 2.5 mrem/hr one day after shutdown. Activation analysis for previous reactor designs indicate that activation of the shield and outlying components result in a dose rate of 2.5 mrem/hr one day after shutdown if the neutron flux at the back of the shield is kept at a level of ~10^6 n/cm^{2}s during operation. The results in Fig. 3.54 imply that a 1.7 m thick shield wall surrounding the reactor at a radius of 10 m makes it possible to perform hands-on-maintenance in the space between it and the outer containment building. This is confirmed by the activation analysis discussed in Section 6. The outer building wall, therefore, needs only to be 1 m thick.

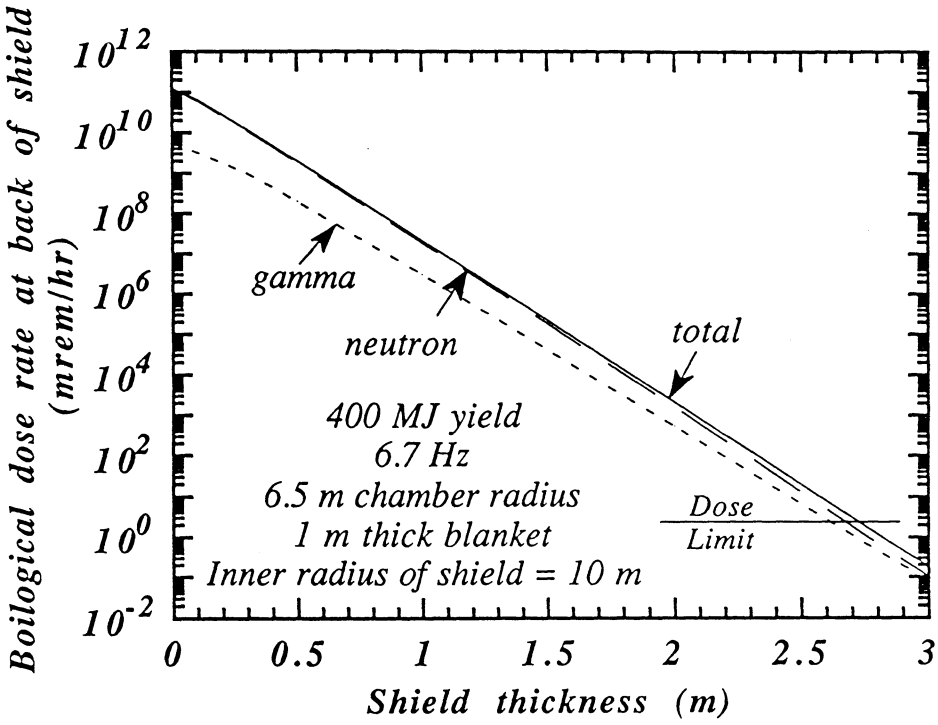

Fig. 3.53. Operational biological dose rate behind the blanket as a function of shield thickness.

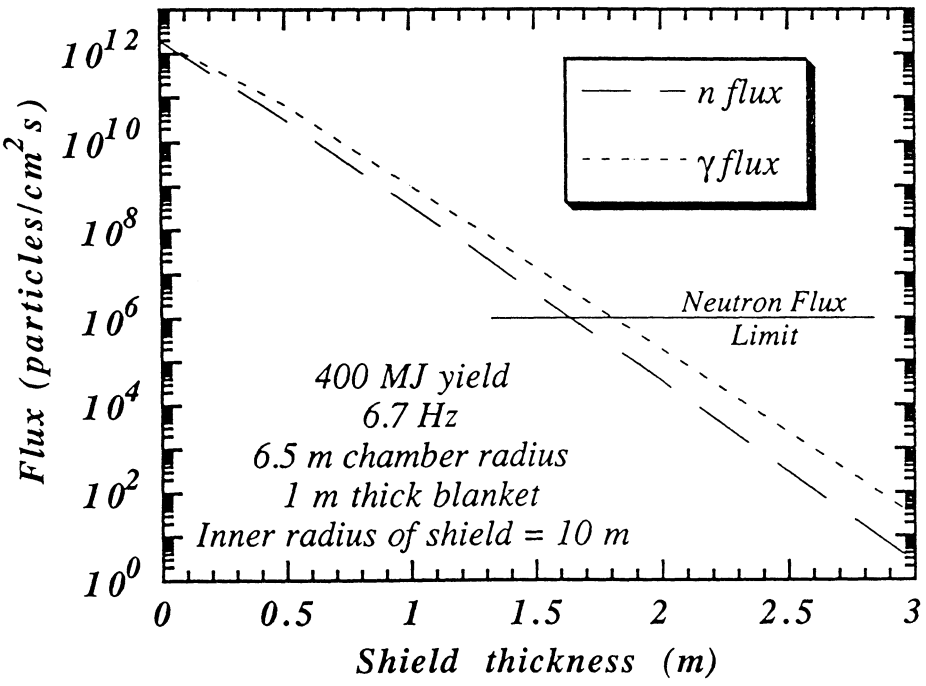

Fig. 3.54. Neutron and gamma flux at the back of the inner biological shield.

3.2.5.5 Lifetime of Final Optics

The lifetime of the final focusing (FF) mirrors depends on the neutron fluence limit for the dielectric coated or metal mirror, the solid angle fraction subtended by the beam ports ($\Delta\Omega/4\pi$), damage recovery with annealing and the location of the mirror relative to the target. The solid angle fraction subtended by the 60 beam ports in SOMBRERO is only 0.25%. The fast neutron flux ($E_n > 0.1$ MeV) level at the grazing incidence metal mirror (GIMM) located in the direct line-of-sight of the source neutrons at 30 m from the target has been determined to be 8.2×10^{12} n/cm^{2}s and is due mostly to the direct source neutrons. Figure 3.55 gives the lifetime for these mirrors as a function of the fast neutron fluence limit and the recovery fraction with annealing. The lifetime without annealing is determined by dividing the fast neutron fluence limit by the fast neutron flux at the mirror. If partial recovery is possible with annealing, the lifetime can be extended until time between anneals becomes very small. A minimum time of one month between anneals is assumed. It can be seen that a GIMM at 30 m from the target, assuming an 80% annealing recovery, can have a lifetime of 17 FPY if the limit is 10^{21} n/cm^2. If the limit is 10^{22} n/cm^2, it can have a lifetime of 40 FPY with no annealing. It is clear that the lifetime of the GIMM is very sensitive to the neutron fluence limit and damage recovery by annealing. Experimental data on radiation damage to metallic mirrors are essential to allow for a more accurate prediction of the GIMM lifetime.

Although the dielectric coated mirrors are placed out of the direct line-of-sight of the source neutrons, secondary neutrons resulting from the interaction of the streaming source neutrons with the GIMM and outer reactor building can cause significant radiation damage to the coating. To reduce the secondary neutron flux, the source neutrons are directed into high aspect ratio traps as shown in Fig. 3.1. Neutronic evaluations show that holes with aspect ratios ~2 will effectively trap most of the neutrons, allowing a negligible amount (<5%) of low energy neutrons to backscatter. As a result, the fast neutron flux ($E > 0.1$ MeV) at the dialectic coated mirrors located at 50 m from the target was determined to be 8.6×10^8 n/cm^{2}s. Figure 3.56 gives the lifetime of the FF mirrors as a function of fluence limit and distance from the target. At a 10^{18} n/cm^2 fast neutron fluence limit, the SOMBRERO FF mirrors will be lifetime components with a lifetime of 37 FPY if they are located at 50 m from the target. Again, experimental data on the impact of radiation damage on the reflectivity of the dielectric coating of the FF mirrors are required.

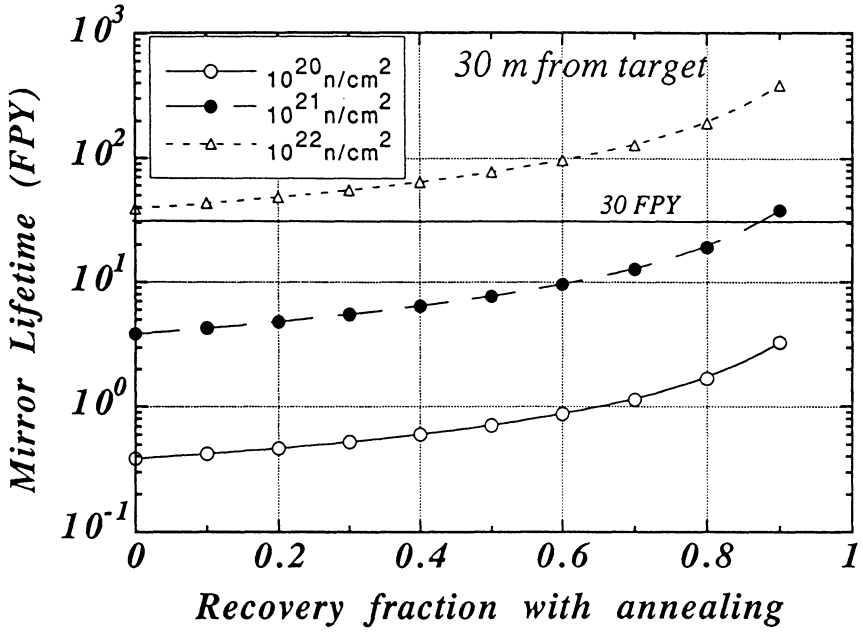

Fig. 3.55. Lifetime of metallic grazing incidence mirrors.

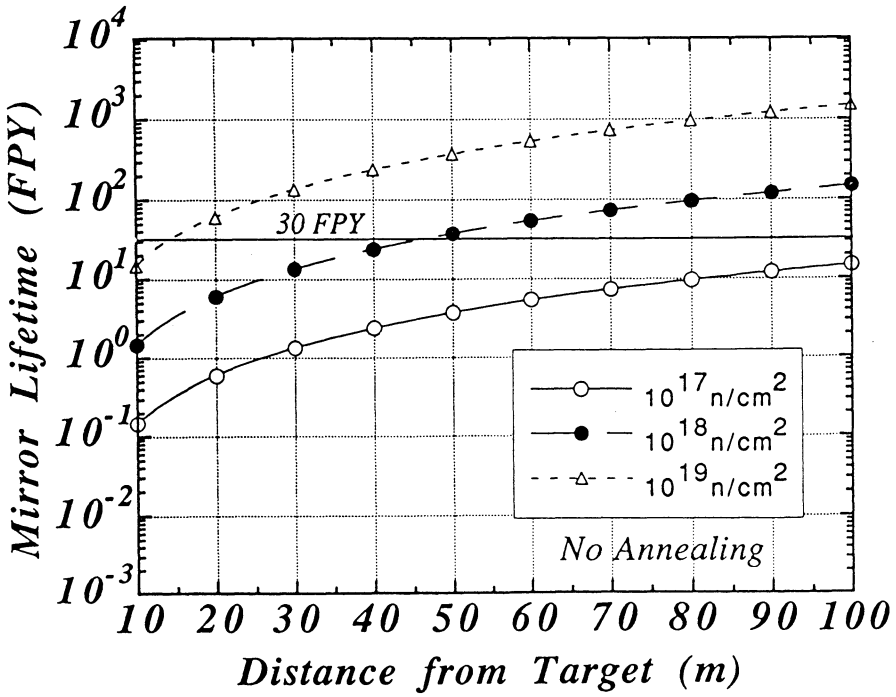

Fig. 3.56. Lifetime of dielectric coated FF mirrors.

3.2.6 Tritium Considerations

3.2.6.1 Chemical State of the Tritium

To produce ~2700 MW of fusion power in the SOMBRERO chamber, tritium is burned at a rate of 410 g(T)/d. Tritium is produced in the Li_2O breeder at the burn rate times the tritium breeding ratio (1.25) to yield 513 g(T)/d. This tritium is soluble in the oxide and is especially difficult to desorb from the surface of the oxide particles. For this reason, most experimentalists utilize a hydrogen overpressure in a circulatory He gas stream to aid in the desorption of T_2 from the in-situ breeder in the blanket.[3.33] Although the breeder particles in SOMBRERO circulate in a closed loop to the heat exchanger, the simplest T recovery scheme still appears to be based upon the evolution of T from the breeder to the gas phase with subsequent recovery of the T from the gas.

The use of H_2 overpressure does not appear practical in the SOMBRERO design because of the formation of HT, which would be carried by the He to the IHX and result in a high permeation rate of T into the lead intermediate heat transfer fluid and eventually into the steam. Because lead has a low solubility for T_2, the only technique to reduce the T_2 concentration in the intermediate loop would be by vacuum pumping, which is very expensive at the low pressures required.[3.34] Another reason to avoid the use of excess H_2 is that the oxygen activity can be decreased to 10^{-25} atm at which point decomposition of Li_2O begins[3.35] forming gaseous species Li and LiH(T), both of which would react with the carbon structure. For these reasons, the oxygen activity was kept $>10^{-10}$ atm so that the T exists as the species HTO, which would permit only very limited T permeation at the IHX. These objectives were accomplished by the addition of H_2O vapor to the He in an amount calculated by the relationship,

$$H_2 + \frac{1}{2} O_2 = H_2O \qquad K_{eq} = 3.2 \times 10^{11}\ \text{atm}^{-1/2} \ @\ 900\ \text{K}.$$

In order to obtain an O_2 activity of 10^{-10} atm, approximately 64 Pa of H_2O were added so that the ratio H_2O/H_2 was 3×10^6. The vapor pressure of the H_2O is much less than the vapor pressure of 3150 Pa required to form a second-phase[3.33] of LiOH(T) in the Li_2O. Such a second-phase would be detrimental because it melts at 417°C and would subsequently agglomerate the oxide particles.

In order to determine the solubility of T in the Li_2O, it is necessary to estimate the HTO partial pressure in the He and the rate of the HTO desorption from the surface of the particles. The determination of the steady-state concentration of HTO in the He is difficult in this design because the He is used at several different velocities for entrainment of the particles; consequently, four sets of He entrances and exits are provided, and the T content in the He of each set may be different.

Initially, we consider the He/HTO concentration which exists within the chamber. The inventory of Li_2O within the chamber is ~668 Mg, and the Li_2O flow rate is 5.55 Mg/s, which gives an average residence time of 120s. The volumetric flow rate is ~5 m^3/s. The He flows counter-current to the breeder at a slow velocity, ~2.5 m^3/s, and a pressure of 2 atm. At steady-state the T desorbs as HTO from the particles at the breeding rate; consequently, the partial pressure of HTO is 5.93 Pa.

Based upon the HTO partial pressure, the solubility of (OH) in the Li_2O can be calculated by use of the relationship,[3.33]

$$S_{OH}\ \text{appm} = 10^{-A}\,(9.864 \times 10^{-6}\,P_{H_2O})^{B} + 173\,(\exp - 2950/T)\,P_{H_2})^{1/2} \qquad (1)$$

where A and B are functions of temperature. The second term, P_{H_2} is very small compared to the first term because of the addition of H_2O. The first term was calculated, therefore, and corrected for the ratio of P_{HTO}/P_{H_2O} and the fact that HTO has only 1 T per molecule. The result indicated that the solubility of T in the Li_2O is 0.10 wppm, in good agreement with an initial estimate of ~0.08 wppm; therefore, for the total 2000 Mg of Li_2O, the T inventory is 160-200 g.

Alternatively, the tritium inventory was estimated based upon the desorption rate of HTO from the surface of the particles, based upon the relationship of the mean residence time,[3.36]

$$\tau = \frac{a^2}{15\,D} + \frac{a}{3}\left[\frac{a \cdot A_s \cdot \rho_{th} \cdot k}{3}\right]^{-1}$$

where

a	=	radius of the grains (~10 μm),
A_s	=	specific surface area (~5×10^{-2} m^2/g),
ρ_{th}	=	theoretical density of Li_2O (~2 g/cm^3),
k	=	desorption coefficient, and,
D	=	diffusion coefficient.

The first term in the above equation represents the diffusive holdup within the particles and is very small because of the small grain size. The measured desorption coefficient, k, has been observed[3.37] to be similar to that for H_2 desorption (i.e., ~1.1×10^{-5} cm/s); hence, the τ value calculated is 94 s. If the breeder were stationary in the chamber, it would have an inventory of ~57 g of (T) before it released T at the breeding rate. This result indicates that the tritium release does not reach steady-state until the breeder material has traveled 75% of the path through the chamber; consequently, some additional HTO will be released to the gas phase as the breeder particles circulate external to the chamber. Additionally, this result suggests that because the entire breeder circuit contains three times as much Li_2O as in the chamber, the total inventory is ~170 g of

T, in good agreement with the solubility data. Other factors to consider in the use of H_2O to control the oxidation state of the oxide breeder are (1) the sublimation of LiOH, (2) the vapor pressure of Li, and (3) potential corrosion of the carbon structure, as noted in the following discussion.

1) The vapor pressure of LiOH will be ~1.6×10^{-2} Pa (1.6×10^{-7} atm)[3.35] at 900 K. The sublimation of this material through the four He exit ports was calculated by use of the relationship,

$$\text{Sublimation Rate} = \frac{\text{velocity of vapor}}{4} \times \frac{\text{moles (LiOH)}}{m^3}$$

This calculation indicated that the sublimation rate would be

$$\frac{5 \times 10^{-4} \text{ moles (LiOH)}}{m^2 \cdot s}$$

Consequently, for 4 He exit ports of ~2.5 m^2/each, the total sublimation would be ~100 kg/day or only ~5% of the total Li_2O in the system.

2) The vapor pressure of metallic Li at 900 K is < 10^{-12} atm (Ref. 3.35) and would cause very minor corrosion of the carbon.

3) The corrosion of neutron irradiation pyrotitic graphite by H_2O vapor has been determined by Hirooka and Imai[3.38] at a series of temperature. For instance, at 880°C the corrosion rate is:

$$R = \frac{4.5 \times 10^{-10} \text{ g}}{cm^2 \cdot s \cdot atm^{1/2}}$$

Consequently, at the H_2O vapor pressure of 64 Pa, the graphite corrosion rate would be only 1.5 μm/yr.

In summary, the addition of a small excess vapor pressure of H_2O is advantageous for the following reasons:

1) It retains the T as the species HTO, which lowers the permeation rate at the IHX.
2) The corrosion rate of the graphite structure is not adversely affected.
3) The vaporization of LiOH(T) is not excessive.

3.2.6.2 Tritium Recovery

Tritium must be continuously recovered from two streams which exit from the chamber, namely (a) the breeder particle stream, and (b) the unburned target fuel which exits through the laser beam holes. Each stream must be processed separately, as described in the following scheme.

The Breeder Stream. Previously, in Section 3.2.6.1, it was noted that the steady-state rate of tritium desorption as HTO from the breeder particles would be the same as the tritium breeding rate, $\sim 6 \times 10^{-3}$ g(T)/s or $\sim 2 \times 10^{-3}$ moles (HTO)/s. Much of this HTO will exit with the He flowing at a rate of 2.5 m^3/s through the chamber; however, additional HTO will be released as the particles transit the entire system. During this transit four entrance/exist streams of He will be used to entrain the particles. If these streams have the same volumetric He flow rates, then, the HTO will be diluted by 10 m^3/s of He at a 2 atm pressure to yield a concentration of 2×10^{-4} moles (HTO)/m^3 with a partial pressure of HTO at 1.5 Pa. In order to recover the tritium at the breeding rate, 10 m^3/s of He must be processed to remove this HTO, and the H_2O at a pressure of 64 Pa. This removal step will utilize adsorption on a molecular sieve drying-bed with a dew-point comparable to -60°C or 1 Pa of H_2O vapor pressure. The HTO vapor pressure at the exit from the dryer will be therefore only 2.3×10^{-2} Pa.

In order to recover the tritium in the water desorbed from the desiccant, a water distillation column could be used to concentrate the HTO, followed by a catalyzed vapor-phase treatment with excess H_2 to yield HT, H_2 and H_2O. The H_2O would be removed by condensation and the gaseous species HT and H_2 would be sent to a cryogenic distillation system which is part of the Fuel Reprocessing System to prepare pure T_2. Alternatively, a newly developed high-temperature processing system[3.39] could be employed to catalytically treat the tritiated water with excess H_2 without using the water distillation system. Such a system avoids the undesirable feature of preparing concentrated tritiated water but increases the volume of gases for the cryogenic distillation system. In either case, pure T_2 would be prepared and sent to the target factory.

Processing the Unburned Target Fuel. Following each target burn event, the unburned fuel, approximately 70% of the injected fuel, together with the waste from the target shell are vaporized and propelled toward the chamber walls, where most of these vapors together with the Xe fill-gas are expelled through the beam ports. After these gases cool, Xe external to the chamber would rush into the partial evacuated chamber. The vaporized condensable gases would begin to condense and perhaps interfere with the subsequent laser beams. For this reason, clean Xe gas is injected into the chamber at a rate sufficient to refill the chamber once per second to a pressure of 0.5 torr. This sweep gas will contain 20.5×10^{-3} g(T)/m^3(Xe)STP plus deuterium and some target shell material, such as a CH-polymer.

The exhaust gases from the chamber will fill the open-spaces in the containment building to a pressure of 0.5 torr. The containment building has a volume of ~1.1×10^6 m^3, but several spaces are excluded for equipment; hence, the space open for the chamber exhaust might be ~30% of the total, e.g., 3.4×10^5 m^3. When filled with Xe, the Xe inventory would be 223 m^3(Xe)STP (1.3 tonnes). Using the previously determined T concentration per m^3(Xe) and the Xe inventory, we note that the total T inventory would be only 4.6 g(T) for the atmosphere in the containment building.

The atmosphere in the containment building would be processed continuously to remove the T, Xe, and other gases exhausted from the chamber. This process would require the removal of 0.54 m^3/s of Xe(STP), comparable to 4×10^5 torr-liters/s. At a pressure of 0.5 torr the required pumping speed is 8×10^5 l/s which could be readily accomplished with several Roots Blowers. This side-stream is purified using the following steps:

1) Filter the gases to remove large particles and cold-trap at 0°C to remove H_2O and oil vapors.
2) Catalytically oxidize to form CO_2, H_2O, DTO, etc.
3) Adsorb water species on a desiccant and CO_2 on an absorbant.
4) After removal from the desiccant, the H_2O species are catalytically treated with excess H_2 to yield the hydrogen species HT, DT, HD, etc. which are sent to the cryogenic distillation columns for the preparation of pure T_2 and returned to the target factory.
5) The Xe would be further purified, if needed, by distillation at -107°C which could also separate any He which might be leaked from the chamber blanket.

3.2.6.3 Permeation of Tritium Into the Power Cycle

A routine release of tritium from the breeder to the environment does occur via permeation of T_2 from the He carrier gas through the tubes of the intermediate heat exchanger (IHX) into the Pb intermediate heat transfer fluid. Lead was selected for the IHX because it would not react exothermally via chemical reactions with either the Li_2O particles or the steam, during accidents, while large exothermal reactions occur when Li_2O reacts with H_2O. Unfortunately, Pb has a very low solubility for T_2; hence, any T_2 which permeates into the lead is retained as gas bubbles, which eventually attain the same T_2 vapor pressure as the primary loop. Therefore, T_2 will permeate into the steam generator at the same rate as through the IHX. Gaseous T_2 could be recovered from the IHX loop by the use of ultra-low pressure vacuum pumps, but would be very costly. For this reason, this system has been designed to limit the permeation of T_2 at the IHX by the addition of H_2O to the primary loop to form HTO which will not permeate.

For ferritic steel tubes in the IHX, the permeation rate of T_2 is,

$$\phi_{T_2} = \frac{2 \times 10^5 \text{ Ci·mm}}{B \text{ m}^2\text{·d·(Pa)}^{1/2}} \left[\exp\left(\frac{11{,}100 \text{ cal/mole}}{RT}\right)\right] \frac{A (P_{T_2})^{1/2}}{t_w}$$

where

A = tube area (5.54×10^3 m^2),

t_w = tube wall thickness (1 mm),

R = 1.98 cal/mole·K,

T = temperature (918 K), and

B = oxide barrier factor

The barrier factor is due to the oxide on the steam side of the steam generator, which reduces the tritium penetration of ferritic steel[3.40] by a factor of ~100. The helium has a P_{T_2} of 2.1×10^{-6} Pa as it exists the top of the chamber. If this gas were transported to the IHX, the tritium would diffuse; however, this stream is subjected to 3 new streams of He with very low T_2 concentration so that the P_{T_2} could easily be diluted by 90% to 2.1×10^{-7} Pa when the He reaches the IHX. Based upon these assumptions, the tritium loss to the steam cycle would be only 12 Ci/d.

3.2.6.4 Pathways of Tritium Release

Some tritium does reach the off-site environment during normal and off-normal operations. In order to assess the potential for these releases, the inventories and rates of processing of tritium in each of the processing systems were determined and the vulnerability of equipment to failure with release of tritium was assessed. The routine releases from the several processing systems were based upon the quantity of tritium processed per day and followed recent experience at TSTA.[3.41] TSTA indicated that only 1.5 Ci of T were released through the stack during the processing of 100 g of T in 38 hr, which is ~1 Ci/d/100 g(T) or a decontamination factor of 10^6. The accidental releases were estimated from the T inventory in the apparatus and the passive safety system in-place which would mitigate the T release. The major systems considered for this study were 1) The Target Factory and Delivery System, 2) the Reactor System, 3) the Fuel Reprocessing System, and 4) the Reactor Building, as summarized in Table 3.13

The Target Factory. This facility must process ~1400 g of tritium per day. For well-enclosed glove boxes and other secondary enclosures, the predicted routine release of T would be 14 Ci/d though through the stack. As described in Section 4.0, only a small inventory of tritium-loaded targets will be continuously prepared; therefore, the quantity of tritium in use along the production line is only 300 g. However, 200 g(T) is enclosed in two liquid cryogenic containers which are usually surrounded by evacuated chambers which have sufficient volumes to contain the total T_2 inventory at a low pressure; consequently, these are fail-safe systems unlikely to release tritium.

Table 3.13. SOMBRERO Tritium Locations, Inventories, Flow Rates, and Potential Release Rates

Location	Inventory g(T)	Flow Rate g(T)/d	Tritium Releases Routine Ci/d	Accident g(T)
Reactor Building				
Atmosphere	4.6	900	23	4.6
Surfaces	<0.1	-		-
Fuel Injection	1.0	1400		1
Reactor System				
Breeder	162	~500	11	80(50%)
Graphite	10	-		-
Helium	5	~500		5
Steam Generator			15	
Fuel Reprocessing				
Desiccant Beds	61	1500		-
Distillation System	13	1500	30	-
Other System	1			-
Target Factory	300	1400	14	100

The Reactor System. The reactor systems consists of the chamber with the breeder blanket, the breeder circuit, and the heat transfer system. The Li_2O breeder particles produce ~500 g(T)/day; however, at steady-state all of this tritium is released to the circulating He. The tritium inventory in the breeder is ~0.081 wppm; consequently, for the total breeder, ~2000 tonnes, the inventory is 162 g(T).

The graphite chamber structure will also absorb some tritium. Only a small quantity HTO should be absorbed by the heat temperature graphite containing the breeder circuit, as shown by the calculated small amount of corrosion by the H_2O vapors. The first wall of graphite facing the target ,however, is subjected to bombardment by D^+ and T^+ ions following each target explosion. Because of the Xe gas protection, these energetic ions do not impinge directly upon the first wall; however, they have been observed to dissolve in graphite particularly along grain boundaries and saturate[3.42] at a concentration of ~5 ppm atom H/atom C. Based upon the mass of the first wall, 165 tonnes of C, the total inventory would be 10 g(T).

The He circuit contains HTO at a partial pressure of 6 Pa and a average temperature of 918°C, giving a total inventory of 5 g(T). This circuit will also process a flow of ~500 g(T)/day. Under routine operation, breeder particles and the accompanying He circuit would process a total of ~1100 g(T)/d and expect to release ~11 Ci/d. At the same time the tritium permeation through the steam generator would be 15 Ci/d. Under accidental conditions, all the helium would be released, containing 5 g(T), and perhaps half of the breeder particles, containing 80 g(T).

Fuel Reprocessing. The fuel reprocessing system generally has high tritium inventories in two pieces of equipment; namely, 1) the dryer beds used to adsorb HTO from both the He and Xe circuits, and 2) the cryogenic distillation system for the separation of the hydrogenic isotopes. For one-hour operation of the desiccant beds, their inventory would be 61 g(T). During continuous operation of the distillation system, it would have an inventory of 13 g(T) based upon an advanced distillation system design.[3.43] Each system processes ~1500 g(T)/d so that the total routine release from these systems could be ~30 Ci/d. Under accidental conditions, all the tritium in the distillation system would be vented to an evacuated tank so that no tritium release would occur. During reheat of a desiccant bed, some tritium could escape; however, the enclosure containing this equipment would also be vented to an evacuated tank so that no tritium release would occur.

Reactor Building. The containment building atmosphere of Xe has a continuous inventory of ~4.6 g(T), but has a daily flow rate of ~900 g(T)/d. The inventory of tritium-loaded targets in the target injector located in the containment building is kept small, ~1 g(T); however, the system handles ~1400 g(T)/d. These two systems would be expected to release routinely ~23 Ci/d of tritium and ~5.6 g(T) during an accidental breach of the containment system.

The wall surface, nearly 1.3×10^5 m^2, of the containment building which contains the Xe and tritium represents many potential sites for tritium adsorption. For this reason these walls should be covered with thin sheets of stainless steel which has a low adsorption for molecular T_2 or DT. This adsorption has been measured experimentally to follow the relationship,[3.44]

$$y = 2.54\ [x]^{1.03}$$

where

x = tritium concentration in the atmosphere (mCi/m^3), and
y = dis/min ($\times 10^{-3}$)/100 cm^2 (of surface).

Based upon the tritium concentration of 135 mCi/m^3 (Xe) @ 0.5 torr, the total adsorption on all of the steel surfaces is very small, 2.5×10^{-4} g(T); however, this adsorption could exceed 1 kg if 10% of the tritium existed as HTO.